University of Rhode Island
DigitalCommons@URI

Open Access Dissertations

2011

GEOACOUSTIC INVERSION USING THE VECTOR FIELD

Steven E. Crocker
University of Rhode Island, steven.e.crocker@gmail.com

Follow this and additional works at: https://digitalcommons.uri.edu/oa_diss

Terms of Use

All rights reserved under copyright.

Recommended Citation

Crocker, Steven E., "GEOACOUSTIC INVERSION USING THE VECTOR FIELD" (2011). *Open Access Dissertations.* Paper 82.
https://digitalcommons.uri.edu/oa_diss/82

This Dissertation is brought to you by the University of Rhode Island. It has been accepted for inclusion in Open Access Dissertations by an authorized administrator of DigitalCommons@URI. For more information, please contact digitalcommons-group@uri.edu. For permission to reuse copyrighted content, contact the author directly.

GEOACOUSTIC INVERSION USING THE VECTOR FIELD

BY

STEVEN E. CROCKER

A DISSERTATION SUBMITTED IN PARTIAL FULFILLMENT OF THE
REQUIREMENTS FOR THE DEGREE OF
DOCTOR OF PHILOSOPHY
IN
OCEAN ENGINEERING

UNIVERSITY OF RHODE ISLAND
2011

DOCTOR OF PHILOSOPHY DISSERTATION

OF

STEVEN E. CROCKER

APPROVED:

Dissertation Committee:

Major Professor James H. Miller

Gopu R. Potty

Malcolm L. Spaulding

D. Randolph Watts

Nasser H. Zawia
DEAN OF THE GRADUATE SCHOOL

UNIVERSITY OF RHODE ISLAND

2011

ABSTRACT

The main goal of this project was to study the use of the acoustic vector field, separately or in combination with the scalar field, to estimate the depth dependent geoacoustic properties of the seafloor via non-linear inversion. The study was performed in the context of the Sediment Acoustics Experiment 2004 (SAX04) conducted in the Northern Gulf of Mexico (GOM) where a small number of acoustic vector sensors were deployed in close proximity to the seafloor. A variety of acoustic waveforms were transmitted into the seafloor at normal incidence. The acoustic vector sensors were located both above and beneath the seafloor interface where they measured the acoustic pressure and the acoustic particle acceleration. Motion data provided by the buried vector sensors were affected by a suspension response that was sensitive to the mass properties of the sensor, the sediment density and sediment elasticity (e.g., shear wave speed). The suspension response for the buried vector sensors included a resonance within the analysis band of 0.4 to 2.0 kHz. The suspension resonance represented an unknown complex transfer function between the acoustic vector field in the seabed and data representing that field. Therefore, inverse methods developed for this study were required to 1) estimate dynamic properties of the sensor suspension resonance and 2) account for the associated corruption of vector field data. A method to account for the vector sensor suspense response function was integrated directly into the inversion methods such that vector channel data corruption was reduced and an estimate of the shear wave speed in the sediment was returned. Inversions of real and synthetic data sets indicated that information about sediment shear wave speed was carried by the suspension response of the buried sensors, as opposed to being contained inherently within the acoustic vector field.

ACKNOWLEDGMENTS

I'd like to thank my major professor, James H. Miller, for his confidence and support during this, our second foray into the world of graduate education. It seems not possible that he supported my educational goals more than 20 years ago, while at the Naval Postgraduate School. It was there that Jim introduced me to acoustics as a powerful tool to understand the undersea environment. I owe him a debt of gratitude for agreeing to take me on once more as I embarked on this most recent educational endeavor. It is with all sincerity that I call Jim Miller my professor, my mentor and my friend.

I am especially grateful to John Osler and Paul Hines of Defence Research and Development Canada (DRDC) Atlantic for providing the data set that served as the foundation of this research. Their generosity and willingness to help a student whom they had never met will not be forgotten.

I would be remiss were I not to acknowledge my Navy colleagues for their support and encouragement during what seemed like a labor without end. Kevin Smith provided encouragement and facilitated the critical financial support needed to begin this effort. Ellen Livingston, Anthony Ruffa and the committee for the In-House Laboratory Independent Research (ILIR) program at the Naval Undersea Warfare Center have at various times provided the financial support required to pursue this work to conclusion. My success is their success.

DEDICATION

This dissertation is dedicated to my parents, who convinced a young man with a penchant for mischief that the key to a happy life was to be found in education.

TABLE OF CONTENTS

CHAPTER

LIST OF TABLES

LIST OF FIGURES

Figure **Page**

Figure **Page**

Figure **Page**

CHAPTER 1

Introduction

1.1 Background

Estimation of seabed sediment properties by inversion of acoustic field data has been the subject of considerable attention. A substantial body of literature [1], [2], [3] exists on inversion of scalar acoustic field data (pressure) for various properties of the seabed. Most of this work has been centered on the inversion of one or more acoustic quantities derived from scalar field measurements. Inversion of the acoustic vector field data has received much less attention. The vector field, defined here as the acoustic particle displacement (and its temporal derivatives), has the potential to convey information about the medium through which the wave field propagates that may not available using the scalar field alone.

Instruments that sense both the acoustic scalar and vector fields continue to evolve as two distinct classes. The class of pressure gradient vector sensors employ a spatial array of scalar measurements. The scalar field is estimated as the mean of the individual measurements. The gradient of the scalar field is estimated using finite differences computed from pairs of scalar measurements arranged to resolve the gradient in one or more spatial directions. Finally, the acoustic vector field is computed from the estimated gradient using the momentum equation

$$\frac{\partial u}{\partial t} = \frac{-\nabla p}{\rho_\circ} \tag{1}$$

where u and p represent the acoustic vector (particle velocity) and scalar (acoustic pressure) fields. The density of the medium is $\rho_\circ$.

The class of inertial vector sensors combines a hydrophone with one or more motion sensors. Motion sensing is typically provided by piezoelectric accelerometers or moving coil geophones [4] arranged to measure three orthogonal components of the acoustic vector field. Acoustic vector sensors employing accelerometers have benefited from recent advances in single crystal piezoelectric materials. These materials have facilitated the design and manufacture of accelerometers with high sensitivity, thus significantly reducing the quantity of material required to achieve a given sensitivity. As a result, the size of the contemporary (accelerometer based) acoustic vector sensor has been dramatically reduced [5] relative to previous designs based on piezoelectric ceramic materials. Much of the work to develop and employ acoustic vector sensors [6], [7], [8] has been directed toward naval applications.

Relatively few investigations on use of the acoustic vector field in geoacoustic inversions have been published. In one study [9], a small vertical array of acoustic vector sensors was used to record a series of broad band (e.g., explosive) signals at a variety of ranges in a shallow water wave guide. The inversion was based on a matched field process where the bottom was parameterized as a homogeneous fluid half space with unknown sound speed and attenuation. Sediment density was provided by a nearby core sample. An objective function was defined that compared the transmission loss for acoustic pressure and the vertical component of the acoustic particle velocity. In addition to providing an estimate of the sediment attenuation, information in the vector field was successfully used to reduce the variance in the estimates for water depth and sediment sound speed relative to inversions based on the scalar field alone.

A similar experiment [10] was conducted near Hawaii where instead of inverting the observed transmission loss, an objective function was defined to operate on complex representations of the acoustic scalar and vector field data. A sensitivity study using synthetic data showed that the method should provide good sensitivity to sediment compression wave speed and density. Experimental results appear to have been consistent with the sensitivity study, however a comparison with results obtained by inversion of scalar field data alone was not provided. As before, the seabed was parameterized as a homogeneous fluid half space.

A distinctly different approach was employed [11] for an experiment conducted in shallow water near Monterey Bay in 2006. In this experiment, a horizontal line array composed of acoustic vector sensors was deployed on the seabed in 85 meters of water. An inversion method operating on data provided by a conventional plane wave beamformer was used to track a moving source. The bottom was parameterized as three fluid layers overlying a homogeneous fluid half space. Geoacoustic parameters reported included layer thickness, compression wave speed and gradient, attenuation and density. Results obtained by inversion of the scalar channels (e.g. hydrophone data) and one component of the vector field (e.g. acoustic particle acceleration parallel to the longitudinal axis of the array) were reported to have been consistent with one another. Results obtained by inversion of vector field data provided no performance advantage relative to results obtained by inversion of scalar acoustic field data alone.

1.2 Objectives

The primary objective of this work was to test the postulate that the acoustic vector field contains information that could be used to invert for the geoacoustic properties of the seafloor, and that this same (or equivalent) information was not available in the scalar field alone.

It is a simple matter to show that this postulate is correct for the simplest case of measurements relating to a plane propagating wave. Consider an experiment in which two hydrophones, separated by a known distance, observe the passage of a plane propagating wave. Countless students of acoustics have *inverted* the equation for propagation $x = ct$ where x, c and t represent the distance traversed, phase speed and elapsed time to yield an estimate of the phase speed based on the known separation and measurement of the time taken to traverse that separation. If the experimental apparatus were also to include a measurement of the acoustic vector field, our student could then estimate the density of the medium using the characteristic impedance $p = \rho_\circ c u$ where p, u, $\rho_\circ$ are the (scalar) acoustic pressure, the (vector) acoustic particle velocity and density, respectively.

This example highlights an important distinction with respect to the parameter estimates. The method for estimation of the phase speed resembles many traditional approaches to geoacoustic inversion in that the estimate represents an average over some spatial domain, such as between two hydrophones. However, the density estimate was derived from knowledge of the scalar and vector fields at a point. The density estimate does not represent a spatial average, nor would it be influenced by properties of the medium at locations removed from the measurement (neglecting for the moment contributions from reflection and backscatter). Thus, the acoustic vector field provided information that was not available in the scalar field. This information allowed our student to estimate a geoacoustic parameter that could not be estimated using the scalar field alone. However, it is important to note that this result represents a point estimate and not an average over the experimental domain.

There is also the potential for vector field data provided by an instrument to contain information exceeding that carried by the vector field in the absence of the instrument. Specifically, the distorted measurement of a real instrument may contain information about the environment that is not available to the undistorted measurement of a hypothetical ideal instrument. It will be shown that the motion of an instrument, in this case an *inertial acoustic vector sensor*, may not equal that of the material in which the instrument is in direct physical communication. The instrument motion may be influenced by a transfer function between itself and the propagating medium. In other words, a suspension response may exist between the instrument and the material with which it is in direct contact. Since the vector field data reflect the motion of the instrument case, not necessarily that of the propagating medium, the suspension response may carry useful information about the environment.

In light of these considerations, the primary objective was expanded to better characterize the value that knowledge of the vector acoustic field may have for a particular geoacoustic inverse problem.

- Does the vector acoustic field carry exploitable information about the environment that is not available in the scalar field?
- Is information carried by the acoustic vector field useful only at the point of measurement, or can it also be used to formulate parameter estimates at locations removed from the point of measurement?
- Can the suspension response of an acoustic vector sensor be used to improve geoacoustic parameter estimates? Does the improvement apply to only certain parameters and not others?

1.3 Analysis Approach

Data to support this work were collected during the Sediment Acoustic Experiment 2004 (SAX04) conducted in the Northern Gulf of Mexico as shown in Fig. 1. The overall objective of the experiment was to better understand acoustic detection at low grazing angles for objects buried in sandy marine sediments. As one component of the experiment, data were collected to study sound penetration into, propagation within, and scattering from the seafloor.

The data used for this work were collected as part of the study to measure sound speed dispersion in sandy sediments using several independent methods.

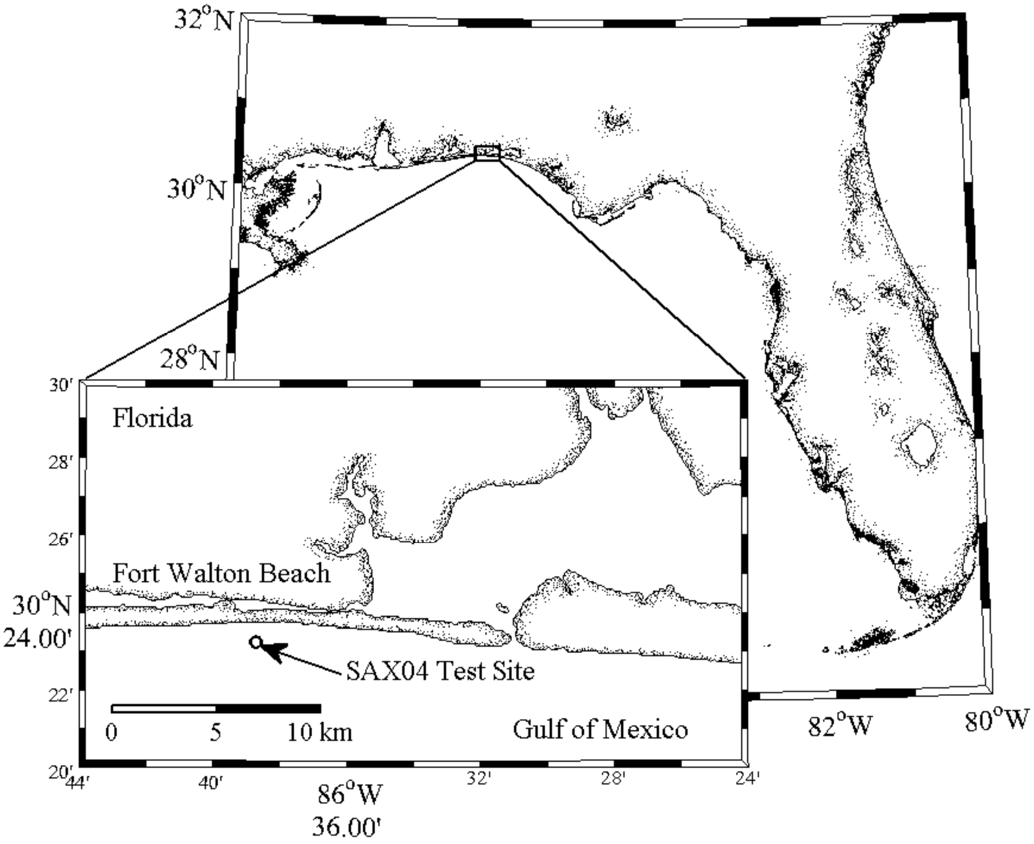

Figure 1. Sediment Acoustics Experiment 2004. Coastline data were extracted from the Global Self-consistent, Hierarchical, High-resolution Shoreline Database (GSHHS) [12].

These experiments were designed for a relatively benign environment where the bottom was parameterized as a homogeneous, sandy sediment half space. The experiments were not specifically designed to collect data to be used for the estimation of sediment properties via geoacoustic inversion. Plans to investigate the potential for inversion of the acoustic vector field were formulated subsequent to the experiment, and the SAX04 data set represented a convenient opportunity to test these ideas. Thus, a method was developed to invert data collected during this experiment to investigate the potential for use of acoustic vector field data.

Figure 2 illustrates the experimental arrangement and geoacoustic parameterization used for this study. The experiment was conducted in a water depth of 16.7 m. An acoustic projector was suspended above the seafloor at a height above bottom of 8.4 m. Directly beneath the projector were located four acoustic vector sensors arranged in a vertical line that spanned the seafloor. Two sensors were suspended above the bottom at heights of 10 and 25 cm. Two sensors were buried in the sediments. The intended burial depths were 50 and 100 cm, although there was uncertainty in the actual burial depths as will be discussed later. Acoustic waveforms were transmitted at a variety of frequencies. Data used for this work ranged from 400 to 2000 Hz with a pulse width of 100 ms. All data were collected at normal incidence.

The environment was parameterized as an isospeed water column with unknown sound speed and depth. The seabed was parameterized as three finite layers with unknown thickness overlying a sediment half space. Unknown geoacoustic properties in all sediment layers included density, compression wave speed and shear wave speed. Thus, the inverse methods developed for this study attempted to estimate a total of 17 unknown parameters using data collected with four acoustic vector sensors that spanned an aperture of about one wavelength at

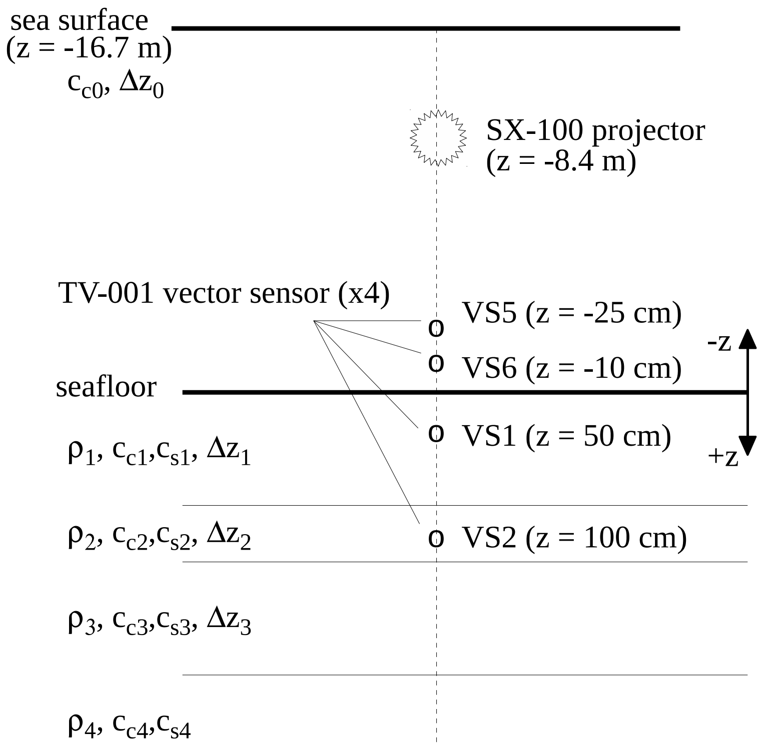

Figure 2. Experimental arrangement. Source and sensor locations were as illustrated. The geoacoustic parameterization used for the inversions is also illustrated. A total of 17 unknown parameters were estimated.

the highest frequency analyzed.

Methods to invert the complex acoustic transfer functions between pairs of sensors were developed. A method to invert the specific acoustic impedance observed by the acoustic vector sensors was also developed. Central to these methods was the definition of an objective function that was normalized to facilitate sensitivity comparisons among data vectors of differing lengths and magnitudes. A sensitivity analysis was performed using synthetic data generated by a seismo-acoustic propagation model. Performance of the inversion methods were also tested using synthetic data to verify the performance of the global optimization method, and to provide a comparison between results of the sensitivity study and the inversions of synthetic data. Finally, the data collected during the SAX04 experiment were inverted for a bottom that was parameterized as a horizontally stratified environment with multiple, elastic layers.

1.4 Outline

Chapter 2 provides a review of seismo-acoustic propagation in a horizontally stratified, range independent waveguide. The numerical code used for this research was the Ocean Acoustic and Seismic Exploration Synthesis (OASES) [13]. The code implements a full wave solution to the Helmholtz equation including numerical methods to evaluate the integral transforms. The resulting numerical model provided several features required by this research including treatment of both the scalar and vector acoustic fields, solutions for propagation in layered viscoelastic media, and accurate calculations in the acoustic near field. This chapter reviews the theory for the generation and propagation of seismo-acoustic waves implemented by OASES and used to support this research.

Chapter 3 discusses measurement of the acoustic vector field. The functional design of the Wilcoxon Research TV–001, an *inertial acoustic vector sensor*, is introduced. A dynamic model for the response of the vector sensor to an incident acoustic vector field is presented. Physics describing specific cases for the motion of an acoustic vector sensor immersed in an inviscid fluid, and when embedded in an elastic solid, are detailed. Transfer functions operating between the incident acoustic vector field, and data representing that field, are derived.

Chapter 4 provides a discussion of the SAX04 experiment. Characteristics of the test site, experiment plan and environmental factors are discussed. An important consideration for this research was the test site itself. Location of a test site with benign environmental characteristics was the principle objective of the site selection processes. However, six weeks before the experiment began, Hurricane Ivan made landfall about 100 km to the west of the test site. The approaching storm drove seas with a significant wave height of 12 m and a storm surge of 3.5 to 4.0 m up onto the shelf resulting in significant redistribution of sediment at the test site. The end result was a seabed that was different, and less homogeneous, than when the site was selected for the SAX04 experiment. [14]

Chapter 4 also presents the data collection method and pre-processing for the SAX04 data set. The data acquisition system is described and an analysis of its noise characteristics is presented. Methods to reduce the gated continuous wave signals transmitted into the seabed are discussed. The variance observed in the data is discussed.

Chapter 5 presents the inversion methods developed for this work. A fundamental component of this research was the definition of an appropriate objective function to support a global, nonlinear search strategy. The objective function derived for this research operated on complex acoustic field data including acoustic transfer functions and specific acoustic impedance. The function was normalized by the data and weighted by the inverse of the data variance such that inversion performance achieved with distinctly different data sets, and derivative acoustic quantities could be compared on a quantitative and objectively verifiable basis. This chapter also reviews the evolutionary algorithm used to execute the global search. The geoacoustic parameterization adopted by the inversion is described.

Chapter 6 presents methods to invert complex acoustic transfer functions for geoacoustic properties of the seabed. Among the primary objectives of this research was to assess the value that knowledge of the acoustic vector field represents, relative to knowledge of the acoustic scalar field alone. The sensitivity of the objective function to variations in the desired geoacoustic parameters is detailed. The studied cases are applicable to the inversion of complex transfer functions for the acoustic scalar field (e.g., pressure), the acoustic vector field (e.g., particle velocity) and combinations of both. In addition, sensitivity of the objective function to sensor burial depth uncertainty is discussed. Inversions of a synthetic data set designed to emulate the reported conditions at the SAX04 experiment site are presented and compared. Finally, inversion of the complex acoustic transfer functions measured during the SAX04 experiment are presented. The relative merits of the various approaches are discussed.

Chapter 7 presents a method to invert the specific acoustic impedance for geoacoustic properties of the seabed. The sensitivity study and synthetic inversions performed for this case are presented and compared to inversions of acoustic transfer functions. Results obtained by inversion of the specific acoustic impedance measured during the SAX04 experiment are presented.

Chapter 8 discusses the results and conclusions of this research. The challenges, complications and potential pitfalls associated with the use of this emerging technology are discussed.

List of References

[1] G. J. Heard, D. Hannay, and S. Carr, "Genetic algorithm inversion of the 1997 geoacoustic inversion workshop test case data," *Journal of Computational Acoustics*, vol. 6, no. 1, pp. 61–71, Mar. 1998.

[2] M. R. Fallat and S. E. Dosso, "Geoacoustic inversion via local, global, and hybrid algorithms," *Journal of the Acoustical Society of America*, vol. 105, no. 6, pp. 3219–3230, June 1999.

[3] G. R. Potty, J. H. Miller, P. H. Dahl, and C. J. Lazauski, "Geoacoustic inversion results from the ASIAEX East China Sea experiment," *IEEE Journal of Oceanic Engineeering*, vol. 29, no. 4, pp. 1000–1010, Jan. 2005.

[4] C. H. Sherman and J. L. Bulter, *Transducers and Arrays for Underwater Sound*. New York: Springer, 2007.

[5] J. C. Shipps and K. Deng, "A minature vector sensor for line array applications," in *Proceedings OCEANS 2003*, 2003, pp. 2367–2370.

[6] A. Nehorai and E. Paldi, "Acoustic vector-sensor array processing," *IEEE Transactions on Signal Processing*, vol. 42, no. 9, pp. 2481–2491, Sept. 1994.

[7] B. A. Cray and A. H. Nuttall, "Directivity factors for linear arrays of velocity sensors," *Journal of the Acoustical Society of America*, vol. 110, no. 1, pp. 324–331, July 2001.

[8] K. B. Smith and A. V. van Leijen, "Steering vector sensor array elements with linear cardiods and nonlinear hippioids," *Journal of the Acoustical Society of America*, vol. 122, no. 1, pp. 370–377, July 2007.

[9] P. Han-Shu and L. Feng-Hua, "Geoacoustic inversion based on a vector hydrophone array," *Chinese Physics Letters*, vol. 24, no. 7, pp. 1977–1980, July 2007.

[10] P. Santos, O. Rodriguez, P. Felisberto, and S. Jesus, "Geoacoustic matched-field inversion using a vertical vector sensor array," in *Proceedings of the Third International Conference and Exhibition on Underwater Acoustic Measurements: Technologies & Results*, June 2009.

[11] R. A. Koch, "Proof of principle for inversion of vector sensor array data," *Journal of the Acoustical Society of America*, vol. 128, no. 2, pp. 590–599, Aug. 2010.

[12] National Geophysical Data Center. "A global self-consistent, hierarchical, high-resolution shoreline database." Feb. 2010. [Online]. Available: http://www.ngdc.noaa.gov/mgg/shorelines/gshhs.html

[13] H. Schmidt, *OASES Version 3.1 User Guide and Reference Manual*, Massachuesetts Institute of Technology, July 2006. [Online]. Available: http://acoustics.mit.edu/faculty/henrik/oases.html

[14] W. C. Vaughan, K. B. Briggs, J.-W. Kim, T. S. Bianchi, and R. W. Smith, "Storm-generated sediment distribution along the northwest Florida inner continental shelf," *IEEE Journal of Oceanic Engineering*, vol. 34, no. 4, pp. 495–515, Oct. 2009.

CHAPTER 2

Review of Sound Propagation

2.1 Acoustic Modeling Approaches

Seismo-acoustic environments encountered in the ocean are generally quite complex. Sound speed in the water column varies with both space and time due to changes in temperature, salinity and density resulting from the transfer of heat at the ocean's surface, tides, currents, eddies and runoff from nearby landmasses. The depth of the water column can vary significantly, particularly in near shore environments. The local geology may be characterized by complex and irregular stratification in which certain physical and geoacoustic properties may be anisotropic. Since acoustic propagation is highly dependent on these properties, exact models require exact knowledge of the environmental properties to the smallest detail, an impossibility for realistic ocean environments.

Acoustic models of the ocean invariably require the judicial use of approximations to obtain a simplified representation of the environment in which the wave equation can be solved numerically. Several specific modeling approaches have been developed, each with its specific assumptions, approximations and limited domain of application. The finite difference [1] and finite element [2] techniques require the fewest approximations for the environment, but the extensive computational requirements have hindered their development and wide use in ocean acoustic applications.

Several efficient techniques have been developed to the general problem, with each employing specific assumptions concerning the environment and acoustic field. Ray tracing methods [3] have received wide use in high frequency open ocean problems where the wavefront is assumed to be locally planar and the wavelength is small relative to the scale at which the environment varies. The parabolic equation approximation [4] effectively treats low frequency propagation in range-dependent environments, but the results are only accurate for moderate grazing angles.

One class of solution technique that has received wide attention requires that the environment be described by a physical model for which the wave equation is separable. The principle of wave equation separation for horizontally stratified media was introduced in underwater acoustics by Pekeris [5], who treated the problem of acoustic propagation in plane layered wave guides using simple two and three layered environmental models. The general approach is to apply a series of integral transforms to the Helmholtz wave equation to reduce the original four dimensional partial differential equation to a series of ordinary differential equations in the depth coordinate. Solutions in this class included the normal mode techniques [6], which are limited to propagation at grazing angles less than critical.

Full wave solutions solve the differential equations within each layer in terms of unknown amplitudes that are determined by matching the boundary conditions at the interfaces between layers. The displacement and stress quantities are determined by evaluation of the inverse integral transforms. These methods can, in principle, yield an exact solution to the wave equation in a horizontally stratified environment. In practice, the accuracy of full wave solutions is limited by the numerical methods used to evaluate the integral transforms. For example, the Fast Field Program (FFP) [7] is effective except for ranges less than a few wavelengths and very steep propagation angles [8] due to the use of an asymptotic approximation for the Hankel transform. The Ocean Acoustics and Seismic Exploration Synthesis (OASES) [9] and its predecessor the Seismo-Acoustic Fast Field Algorithm for Range Independent Environments (SAFARI) [10] addressed these limitations with improved numerical methods to evaluate the integral transforms.

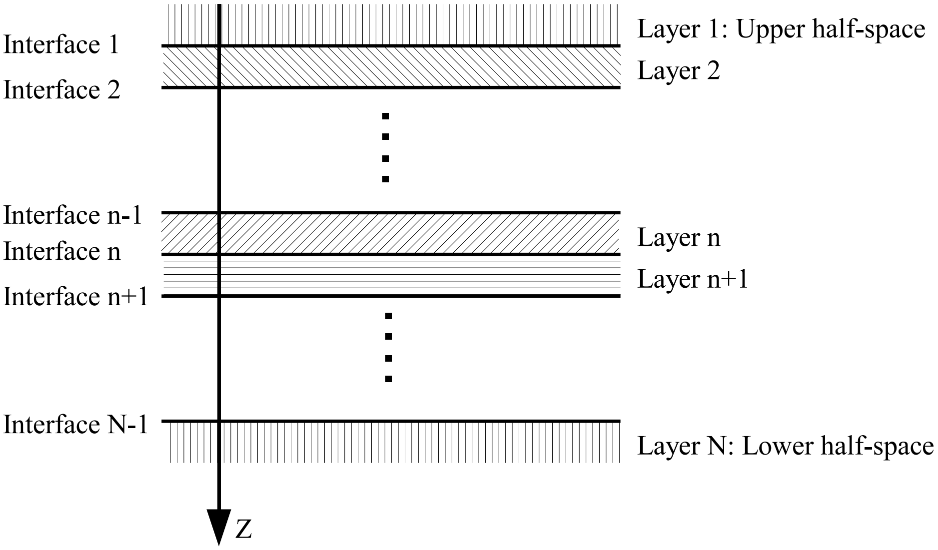

Figure 3. Horizontally stratified environment

2.2 The Seismo-Acoustic Model

Following the development of Schmidt [11], the environment is assumed to be horizontally stratified, with all interfaces plane and parallel. The layers, including the upper and lower half spaces, may be fluids, viscoelastic solids or empty space. The solid layers are required to be isotropic and homogeneous viscoelastic media with Lamé constants λ_n and μ_n, density ρ_n where the subscript n indicates the layer number. A cartesian system of coordinates $\{x, y, z\}$ is adopted with the z axis perpendicular to the interfaces and positive downwards as illustrated in Fig. 3. The choice of coordinates reflects the geometry of the SAX04 experiment by permitting both positive and negative wave numbers as required for accurate results at normal incidence (e.g., zero range) [9].

The y axis is oriented parallel to a line source, thus rendering the field independent of y. The displacement components $\{\xi, \nu, \eta\}$ in layer n are expressed in terms of the displacement potentials $\{\Phi_n, \Psi_n\}$, provided as Eqs. 2–4 and where body forces are assumed to be absent.

$$\xi\left(x,z\right)|_n = \frac{\partial \Phi_n}{\partial x} - \frac{\partial \Psi_n}{\partial z} \tag{2}$$

$$\nu\left(x,z\right)|_n = 0 \tag{3}$$

$$\eta\left(x,z\right)|_n = \frac{\partial \Phi_n}{\partial z} + \frac{\partial \Psi_n}{\partial z} \tag{4}$$

The displacement potentials satisfy the wave equations, Eq. 5 and Eq. 6.

$$\left(\nabla^2 - \frac{1}{c_{c_n}^2}\frac{\partial}{\partial t^2}\right)\Phi_n = 0 \tag{5}$$

$$\left(\nabla^2 - \frac{1}{c_{s_n}^2}\frac{\partial}{\partial t^2}\right)\Psi_n = 0 \tag{6}$$

The phase speeds for compression waves c_{c_n} and shear waves c_{s_n} are provided as Eq. 7 and Eq. 8. If the medium is a fluid, then μ_n and Ψ_n vanish, leaving only the potential Φ_n and the problem is reduced to the special case of classical acoustics.

$$c_{c_n} = \sqrt{\frac{\lambda_n + 2\mu_n}{\rho_n}} \tag{7}$$

$$c_{s_n} = \sqrt{\frac{\mu_n}{\rho_n}} \tag{8}$$

Acoustic sources are assumed time harmonic with angular frequency ω. The time dependence represented as $e^{j\omega t}$ is suppressed in the discussion that follows.

The wave equations now take the familiar form

$$\left(\nabla^2 + k_n^2\right)\Phi_n = 0, \tag{9}$$

$$\left(\nabla^2 + h_n^2\right)\Psi_n = 0, \tag{10}$$

where k_n and h_n are the complex wave numbers for compression and shear waves, respectively,

$$k_n^2 = \left(\frac{\omega}{c_{c_n}}\right)^2 = \frac{\omega^2 \rho_n}{\lambda_n + 2\mu_n}, \tag{11}$$

$$h_n^2 = \left(\frac{\omega}{c_{s_n}}\right)^2 = \frac{\omega^2 \rho_n}{\mu_n}. \tag{12}$$

Taking the Fourier transform of Eq. 9 and Eq. 10, the integral representations for the solutions become

$$\Phi_n\left(x, z\right) = \int_{-\infty}^{\infty} \left(A_n^-\left(s\right) e^{-zk_{z_n}(s)} + A_n^+\left(s\right) e^{zk_{z_n}(s)}\right) e^{-jsx}\ ds, \tag{13}$$

$$\Psi_n\left(x, z\right) = j\int_{-\infty}^{\infty} \left(B_n^-\left(s\right) e^{-zh_{z_n}(s)} + B_n^+\left(s\right) e^{zh_{z_n}(s)}\right) e^{-jsx}\ ds, \tag{14}$$

where A_n^-, A_n^+, B_n^- and B_n^+ are arbitrary functions in the horizontal wave number s, and where

$$k_{z_n}\left(s\right) = \sqrt{s^2 - k_n^2}, \tag{15}$$

$$h_{z_n}\left(s\right) = \sqrt{s^2 - h_n^2}. \tag{16}$$

The integral transforms of Eq. 13 and Eq. 14 effectively decompose the total fields into up and down going plane waves integrated over all wave numbers.

Substituting the displacement potentials, Eq. 13 and Eq. 14, into the equations of motion, Eq. 2 and Eq. 4, yields the following integral representations for the displacements

$$\begin{split}\xi\left(x, z\right)|_n = j\int_{-\infty}^{\infty} \Big(&-sA_n^- e^{-zk_{z_n}} - sA_n^+ e^{zk_{z_n}} \\ &+ h_{z_n} B_n^- e^{-zh_{z_n}} - h_{z_n} B_n^+ e^{zh_{z_n}}\Big) e^{-jsx}\ ds,\end{split} \tag{17}$$

$$\begin{split}\eta\left(x, z\right)|_n = \int_{-\infty}^{\infty} \Big(&-k_{z_n} A_n^- e^{-zk_{z_n}} + k_{z_n} A_n^+ e^{zk_{z_n}} \\ &+ sB_n^- e^{-zh_{z_n}} + s_n B_n^+ e^{zh_{z_n}}\Big) e^{-jsx}\ ds.\end{split} \tag{18}$$

The stresses involved in the boundary conditions conform to Hooke's law yielding Eq. 19 and Eq. 20.

$$\begin{aligned}\sigma_{zz}(x,z)\,|_n &= (\lambda_n + 2\mu_n)\frac{\partial \eta}{\partial z} + \lambda_n \frac{\partial \xi}{\partial x} \\ &= \mu_n \int_{-\infty}^{\infty} \Big(\left(2s^2 - h_n^2\right)\left(A_n^- e^{-zk_{z_n}} + A_n^+ e^{zk_{z_n}}\right) \\ &\qquad + 2sh_{z_n}\left(-B_n^- e^{-zh_{z_n}} + B_n^+ e^{zh_{z_n}}\right)\Big) e^{-jsx}\, ds\end{aligned} \tag{19}$$

$$\begin{aligned}\sigma_{xz}(x,z)\,|_n &= \mu_n \left(\frac{\partial \xi}{\partial z} + \frac{\partial \eta}{\partial x}\right) \\ &= j\mu_n \int_{-\infty}^{\infty} \Big(2sk_{z_n}\left(A_n^- e^{-zk_{z_n}} - A_n^+ e^{zk_{z_n}}\right) \\ &\qquad + \left(2s^2 - h_n^2\right)\left(B_n^- e^{-zh_{z_n}} + B_n^+ e^{zh_{z_n}}\right)\Big) e^{-jsx}\, ds.\end{aligned} \tag{20}$$

In the case of a fluid layer the displacements follow directly from Eq. 17 and Eq. 18 by setting B_n^+ and B_n^+ to zero. The shear stress σ_{xz} vanishes, whereas Eq. 20 is replaced by

$$\sigma_{zz}(x,z)\,|_n = -\lambda_n k_n^2 \int_{-\infty}^{\infty} \left(A_n^- e^{-zk_{z_n}} + A_n^+ e^{zk_{z_n}}\right) e^{-jsx}\, ds. \tag{21}$$

Contribution from sources within layer n must be added to produce expressions for the total field in the layer. Since we have restricted ourselves to compressional line sources at $x = 0$, the field produced in an infinite medium with the material properties of layer n, has the integral representation provided as

$$\overset{*}{\Phi}_n(x,z) = -\int_{-\infty}^{\infty} \frac{e^{-|z-z_s|k_{z_n}}}{k_{z_n}} e^{-jsx}\, ds, \tag{22}$$

$$\overset{*}{\Psi}_n(x,z) = 0, \tag{23}$$

where z_s is the source depth.

The corresponding displacements involved in the boundary conditions are again obtained from Eq. 2 and Eq. 4 as

$$\overset{*}{\xi}(x,z)\,|_n = j \int_{-\infty}^{\infty} \frac{s e^{-|z-z_s|} k_{z_n}}{k_{z_n}} e^{-jsx}\, ds, \tag{24}$$

$$\overset{*}{\eta}(x,z)\,|_n = \int_{-\infty}^{\infty} \operatorname{sign}(z - z_s)\, e^{-|z-z_x|k_{z_n}} e^{-jsx}\; ds, \tag{25}$$

while the stresses are given by Hooke's law:

$$\overset{*}{\sigma}_{zz}|_n = -\mu_n \int_{-\infty}^{\infty} \left(2s^2 - h_n^2\right) \frac{e^{-|z-z_s|k_{z_n}}}{k_{z_n}} e^{-jsx}\; ds, \tag{26}$$

$$\overset{*}{\sigma}_{xz}|_n = -j\mu_n \int_{-\infty}^{\infty} 2s\ \operatorname{sign}(z - z_s)\, e^{-|z-z_s|k_{z_n}} e^{-jsx}\; ds. \tag{27}$$

In the fluid case Eq. 26 is replaced by

$$\overset{*}{\sigma}_{zz}(x,z)\,|_n = \lambda_n k_n^2 \int_{-\infty}^{\infty} \frac{e^{-|z-z_x|k_{z_n}}}{k_{z_n}} e^{-jsx}\; ds. \tag{28}$$

2.2.1 Boundary Conditions

The boundary conditions that must be satisfied at an interface are determined by the materials on either side of that interface.

- If the interface separates two fluids, the vertical displacement η and the normal stress σ_{zz} are continuous. If one of the media is a vacuum, then the normal stress σ_{zz} vanishes.

- If one of the layers is solid and the other is a vacuum, both σ_{zz} and σ_{xz} vanish. An interface separating a fluid and solid requires that η and σ_{zz} are continuous and that σ_{xz} vanish.

- Displacements η, ξ and stresses σ_{zz}, σ_{xz} must be continuous at a no-slip interface between two solid media.

Since the boundary conditions are satisfied at all ranges x, they must also be satisfied by the kernels in the integral representations. The radiation conditions for $z \to \pm\infty$ together with the simultaneous satisfaction of the boundary conditions at all interfaces, lead to a linear system of equations in the unknown functions A^-, A^+, B^- and B^+.

Exact solutions require that one solve this system for all horizontal wave numbers, followed by evaluation of the inverse integral transforms. Only for a few trivial cases are exact solutions known. In general, solution of the linear system of equations and the evaluation of the inverse transforms must be done numerically. Thus the horizontal wave number axis over which the integration is performed must be sampled over a finite interval.

2.2.2 Attenuation

Assume a plane harmonic wave of angular frequency ω propagating in a homogeneous medium in the positive x direction of a cartesian coordinate system having the form

$$F\left(x,t\right)=Ae^{j\left(\omega t-k_m x\right)}, \tag{29}$$

where k_m is the medium wave number for either compression or shear waves. The wave amplitude A is constant for all ranges x in the case of k_m purely real. Attenuation in viscous fluids [12] and viscoelastic solids [13] is frequently accounted for by letting the medium wave number k_m be complex,

$$\widetilde{k}_m=k_m\left(1-j\delta\right), \quad \delta>0. \tag{30}$$

Substitution of the complex wave number into the expression for a plane propagating wave yields

$$F\left(x,t\right)=Ae^{-\delta k_m x}e^{j\left(\omega t-k_m x\right)}. \tag{31}$$

The amplitude decays exponentially in range as required for linear viscoelastic fluid and solid media. Since the full wave field solution is based on decomposition of the field into plane wave components, viscoelastic attenuation may be taken into account by letting the medium wave numbers and the Lamé constants be complex where

$$\widetilde{\lambda}=\lambda+j\lambda', \tag{32}$$

$$\widetilde{\mu} = \mu + j\mu'. \tag{33}$$

It has been experimentally observed [13] that most solid media exhibit an attenuation that increases linearly with frequency (e.g., δ = constant). For these solids,

$$\frac{\lambda' + 2\mu'}{\lambda + 2\mu} = \frac{1}{Q_c}, \tag{34}$$

$$\frac{\mu'}{\mu} = \frac{1}{Q_s}, \tag{35}$$

where Q_c and Q_s are constants. By inserting the complex Lamé constants in Eq. 34 and Eq. 35, we get from Eq. 36 and Eq. 37 the following value of δ for compressional and shear waves respectively, assuming $Q_c,\ Q_s \gg 1$

$$\delta_c = \frac{1}{2Q_c}, \tag{36}$$

$$\delta_s = \frac{1}{2Q_s}. \tag{37}$$

In underwater acoustics it is more common to express the linear frequency dependent attenuation in decibels per wave length

$$\begin{aligned} \alpha &= -20\log_{10}\left(\frac{F\left(x+\Lambda,t\right)}{F\left(x,t\right)}\right) \\ &= -20\log_{10}\left(e^{-\delta k_m \Lambda}\right) \\ &= \ 40\pi\delta\log_{10}(e) \\ &\approx \frac{27.29}{Q}. \end{aligned} \tag{38}$$

A physically meaningful solution requires that pure dilation of a solid does not produce energy. Therefore, the bulk modulus, $K = \lambda + \frac{2}{3}\mu$ must have a positive imaginary part, which yields

$$\frac{\alpha_s}{\alpha_c} = \frac{\delta_x}{\delta_c} < \frac{3}{4}\left(\frac{c_c}{c_s}\right)^2. \tag{39}$$

The linear elastic fluid media are limiting cases of solids with $\mu \to 0$.

List of References

[1] R. A. Stephen, "A review of finite difference methods for seismo-acoustics problems at the seafloor," *Reviews of Geophysics*, vol. 26, no. 3, pp. 445–458, 1988.

[2] C. P. Vendhan, G. C. Diwan, and S. K. Bhattacharyya, "Finite-element modeling of depth and range dependent acoustic propagation in oceanic waveguides," *Journal of the Acoustical Society of America*, vol. 127, no. 6, pp. 3319–3326, June 2010.

[3] C. A. Boyles, *Acoustic Waveguides: Applications to Oceanic Science.* New York: John Wiley and Sons, 1984.

[4] F. D. Tappert, *The Parabolic Approximation Method*, ser. Lecture Notes in Physics. New York: Springer-Verlag, 1977, vol. 70.

[5] C. L. Pekeris, "Theory of propagation of explosive sound in shallow water," in *Memiors*, vol. 27. Geological Society of America, 1948.

[6] R. B. Evans, "A coupled mode solution for acoustic propagation in a waveguide with stepwise depth variations of a penetrable bottom," *Journal of the Acoustical Society of America*, vol. 74, no. 1, pp. 188–195, July 1983.

[7] F. R. DiNapoli and R. L. Davenport, "Theoretical and numerical Green's function field solution in a plane multilayered medium," *Journal of the Acoustical Society of America*, vol. 67, no. 1, pp. 92–105, Jan. 1980.

[8] F. B. Jensen, W. A. Kuperman, M. B. Porter, and H. Schmidt, *Computational Ocean Acoustics*, ser. Modern Acoustics and Signal Processing. New York: Springer-Verlag, 1993.

[9] H. Schmidt, *OASES Version 3.1 User Guide and Reference Manual*, Massachuesetts Institute of Technology, July 2006. [Online]. Available: http://acoustics.mit.edu/faculty/henrik/oases.html

[10] H. Schmidt, *SAFARI Seismo-Acoustic Fast Field Algorithm for Range Independent Environments*, Supreme Allied Command Anti-Submarine Warfare Research Center, La Spezia, Italy, Sept. 1988.

[11] H. Schmidt and F. B. Jensen, "A full wave solution for propagation in multilayered viscoelastic media with application to Gaussian beam reflection at fluid-solid interfaces," *Journal of the Acoustical Society of America*, vol. 77, no. 3, pp. 813–825, Mar. 1985.

[12] S. Temkin, *Elements of Acoustics.* New York: John Wiley and Sons, 1981.

[13] H. Kolsky, *Stress Waves in Solids.* New York: Dover Publications, 1963.

CHAPTER 3

Acoustic Vector Field Measurement

3.1 Acoustic Vector Sensor Description

The acoustic vector sensors used for this study were model TV–001 manufactured by Wilcoxon Research [2]. The TV–001 belongs to the *inertial* class of acoustic vector sensors in that it responds to the motion of the sensor package. The basic operational principle is illustrated in Fig. 4 as disclosed in the patent [1] applicable to the TV-001 sensor. The following parenthetical numbering scheme refers to elements in the patent drawing of Fig. 4. A piezoelectric material (204), in this case a shear mode single crystal, is sandwiched between a proof mass (202) and a foundation (206). The foundation is rigidly fixed to the sensor case. When subjected to acceleration, the inertia of the proof mass causes a shear strain in the piezoelectric crystal, resulting in an electric charge that is sensed, conditioned and output as a voltage at the sensor leads. The arrangement functions as a single axis accelerometer. The sensor includes three such arrangements that are oriented to resolve acceleration into three orthogonal components. In addition, the sensor provides a collocated measurement of the acoustic pressure using a hydrophone.

The design objective for an inertial acoustic vector sensor is to provide an output signal that is proportional to the local acoustic vector field, in this case the acoustic particle acceleration. The primary means of realizing this objective is to design the acoustic vector sensor system such that the motion of the sensor case is identical to that of the medium in which the sensor is immersed, typically seawater. However, sensor designers often do not know the details of the applications in which their sensors will be used. Thus, it is incumbent on the end user to verify that details of the system design do not adversely affect sensor performance. In particular, the potential for the sensor motion to be appreciably different from that

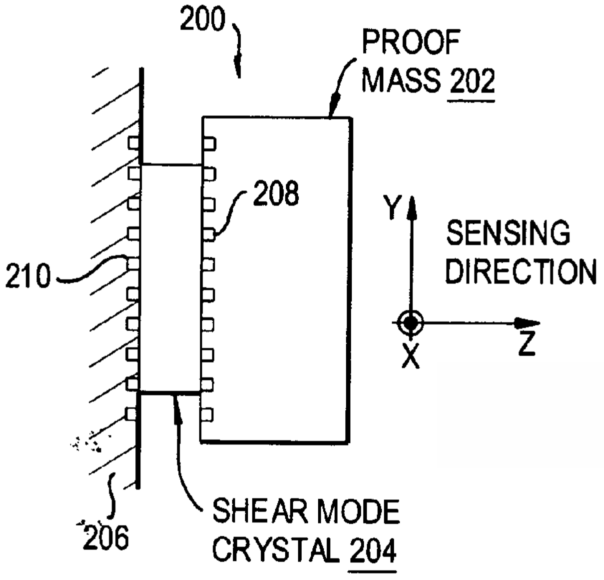

Figure 4. Inertial acoustic vector sensor. Operational principle for the Wilcoxon Research TV–001 acoustic vector sensor. [1]

of the acoustic vector field must be understood and properly accounted for when processing data from the vector channels.

Specifications for the TV–001 acoustic vector sensors are provided as Table 1.

3.2 Acoustic Vector Sensor Suspension Response

Acoustic vector sensors are designed for operation in fluids, typically seawater. Data provided by an inertial vector sensor reflect the motion of the sensor package, not necessarily that of the surrounding medium. Thus, requirements for the successful design and use of acoustic vector sensors are more stringent than those for hydrophones due to the dynamics of the vector sensing mechanism.

Practical applications using vector sensors invariably involve a mount, or similar physical constraint, that is applied to the sensor case. This has the effect of modifying the response by creating a velocity transfer function between the sensor

Table 1. Wilcoxon Research TV-001 specifications [2]

Dynamic	
Output Sensitivity	
Accelerometer	1.0 V/g
Hydrophone	-174 dB re 1.0 V/μPa
Full Scale Input Range	
Accelerometer	3.0 g peak-to-peak
Hydrophone	200 Pa peak
Resonance Frequency	$>$ 10 kHz (design)
Frequency Response	3 Hz to 9 kHz (design)
Transverse Sensitivity	$<$ 5%
Electrical	
Power	
Voltage	6.8 VDC typical
Current	$<$ 25 mA
Output Impedance	$<$ 100 Ω and 10 nF
Environmental	
Temperature Range	
Operational	−40°C to 60°C
Pressure Range	
Operational	0 to 10 MPa
Survival	17 MPa
Physical	
Mass	54 gram (without cables)
Length	71.3 mm
Diameter	40.7 mm
Case	Polyurethane encapsulated

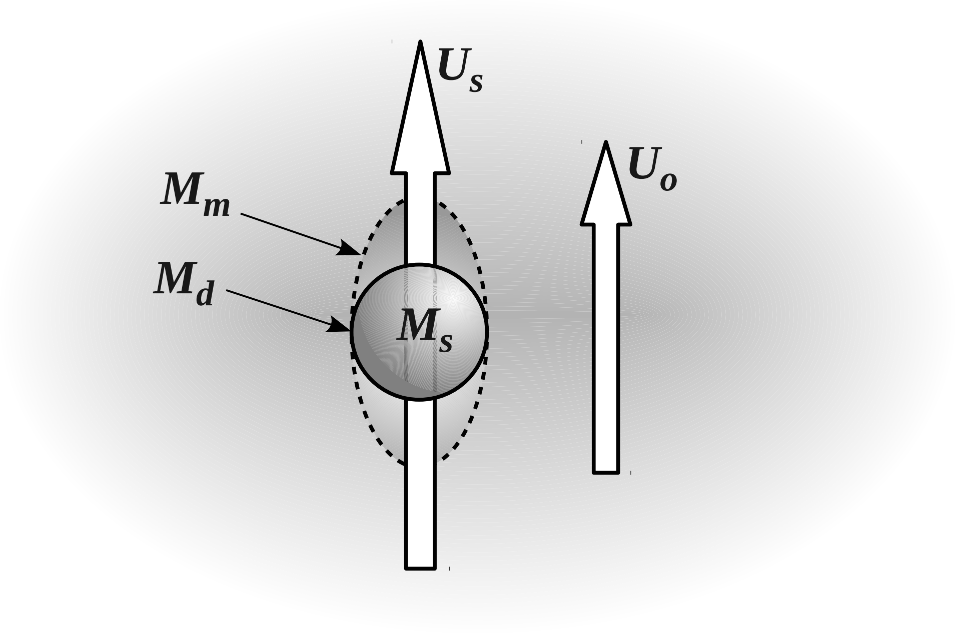

Figure 5. Acoustic vector sensor dynamic model. Model parameters include the sensor mass M_s, mass displaced by the sensor M_d, added (or inertial) mass due to sensor motion M_m, sensor velocity U_s and incident acoustic particle velocity $U_\circ$.

and the medium with which the sensor is in direct contact. Design requirements for an effective vector sensor mount include a) a natural frequency well outside the intended range of acoustic sensing; b) fix the average position and orientation of the sensor body, c) permit movement of the sensor body in response to the acoustic field, d) isolate the sensor from structure-born noise, and e) not distort the response of the sensor in either magnitude or phase [3].

Figure 5 illustrates the dynamic model of a rigid sensor case in direct communication (e.g., immersed or embedded) with a propagating medium. The sensor velocity U_s, medium (e.g. vector field) velocity $U_\circ$, sensor mass M_s, added mass M_m and mass of material displaced by the sensor M_d are annotated.

The steady-state equation of motion (Eq. 40), derived for an accelerated frame of reference in which the medium (e.g., seawater or sediment) is at rest was developed [4] as an extension of the analysis for the dynamic response of an ocean bottom seismometer [5]. In this reference frame, the sensor velocity is $(U_s - U_\circ)$ and its acceleration is $j\omega\left(U_s - U_\circ\right)$. The forcing function is the oscillatory term $-j\omega U_\circ\left(M_s - M_d\right)$ due to the net weight of the sensor in the pseudo-gravitational field $-j\omega U_\circ$ opposed by the "buoyancy" of the sensor due to the material displaced by the sensor. A term for the restoring force due to the mechanical impedance Z_m of the interaction between the sensor and the surrounding medium is also required. The added mass having been accounted for, the term $-\widetilde{Z}_m\left(U_s - U_\circ\right)$ accounts only for the stiffness and resistance that may be present.

$$j\omega\left(U_s - U_\circ\right)\left(M_s + M_m\right) = -j\omega U_\circ\left(M_s - M_d\right) - \widetilde{Z}_m\left(U_s - U_\circ\right) \tag{40}$$

Rearrangement of Eq. 40 provides the sensor-to-medium velocity ratio for a rigid sensor body, oscillating with a wavelength that is sufficiently long that the medium velocity can be approximated as spatially uniform in the vicinity of the sensor and time harmonic. The mass and stiffness of the sensor leads were assumed to be negligible. Equation 41 represents the transfer function between the particle velocity due to wave motion in the propagating medium and the resultant motion of the acoustic vector sensor

$$H_s\left(\omega, M_s, M_m, M_d, \widetilde{Z}_m\right) = \frac{U_s}{U_\circ} = \frac{j\omega\left(M_d + M_m\right) + \widetilde{Z}_m}{j\omega\left(M_s + M_m\right) + \widetilde{Z}_m}. \tag{41}$$

Oestreicher [6] derived the mechanical impedance for a rigid sphere, oscillating in a compressible viscoelastic material from first principles for biophysical applications. The impedance, including terms representing the contribution from the added mass, was provided as Eq. 42 as a function of the sphere radius a, shear wave number h, compression wave number k, and medium density $\rho_\circ$

$$Z_m = -j\omega\rho_\circ \frac{4\pi a^3}{3} \frac{\left(1 - \frac{j3}{ha} - \frac{3}{(ha)^2}\right) - 2\left(\frac{j}{ha} + \frac{1}{(ha)^2}\right)\left(3 - \frac{(ka)^2}{jka+1}\right)}{\left(\frac{j}{ha} + \frac{1}{(ha)^2}\right)\left(\frac{(ka)^2}{jka+1}\right) + \left(2 - \frac{(ka)^2}{jka+1}\right)}. \tag{42}$$

The shear and compression wave numbers are related to their respective material properties by Eqs. 43 and 44, where μ_1 and μ_2 are the coefficients of shear elasticity and shear viscosity. Likewise, λ_1 and λ_2 are the coefficients of volume elasticity and volume viscosity.

$$h = \left(\frac{\rho_\circ\omega^2}{\mu}\right)^{\frac{1}{2}} \qquad \mu = \mu_1 + j\omega\mu_2 \tag{43}$$

$$k = \left(\frac{\rho_\circ\omega^2}{2\mu + \lambda}\right)^{\frac{1}{2}} \qquad \lambda = \lambda_1 + j\omega\lambda_2 \tag{44}$$

3.2.1 Acoustic Vector Sensor in an Inviscid Fluid

The special case for the mechanical impedance $Z_m^{(f)}$ of a small rigid spherical body oscillating in an inviscid, compressible fluid is given when the shear elasticity, shear viscosity and volume viscosity vanish (e.g., $\mu_1 = \mu_2 = \lambda_2 = 0$). In this case, the impedance of Eq. 42 is reduced to

$$Z_m^{(f)} = -j\omega\rho_\circ \frac{4\pi a^3}{3} \left(\frac{2 + (ka)^2 - j(ka)^3}{4 + (ka)^4}\right) \tag{45}$$

Under these circumstances, the mechanical impedance results from the inertia of the added mass and a radiation resistance associated with the acoustic field. A useful form of Eq. 45 is

$$Z_m^{(f)} = -\left(j\omega M_m^{(f)} + R_m^{(f)}\right) \tag{46}$$

where terms for the added mass $M_m^{(f)}$ and resistance $R_m^{(f)}$ are given by

$$M_m^{(f)} = \rho_\circ \frac{4\pi a^3}{3} \left(\frac{2 + (ka)^2}{4 + (ka)^4}\right), \tag{47}$$

$$R_m^{(f)} = \frac{1}{3} S \rho_\circ c_p \, \frac{(ka)^4}{4 + (ka)^4}, \tag{48}$$

and S is the surface area of the sphere. The compression wave speed is c_p. Non-dimensional forms of the added mass and resistance are presented in Fig. 6.

When the body is small relative to a wavelength (e.g., $ka \ll 1$), inspection of Eqs. 47 and 48 shows that the added mass $M_m^{(f)}$ is half the displaced mass, the resistance $R_m^{(f)}$ is proportional to $(ka)^4$ and the impedance is controlled by the inertia associated with the added mass (e.g., $j\omega M_m^{(f)} \gg R_m^{(f)}$). Under these conditions, it is easily confirmed that the velocity transfer function of Eq. 41 reduces to the classic case [7] where the sensor-to-fluid velocity ratio $U_s/U_\circ$ is given by

$$H_s^{(f)} = \frac{U_s}{U_\circ} = \frac{3\rho_\circ}{2\rho_s + \rho_\circ} \tag{49}$$

when ρ_s and $\rho_\circ$ are the densities of the sensor and fluid, respectively. Consistent with the result of Eq. 41, the sensor velocity U_s is equal to the fluid particle velocity $U_\circ$ when the sensor is neutrally buoyant (e.g. $\rho_s = \rho_\circ$).

The velocity of an acoustic vector sensor immersed in an inviscid, compressible fluid equals that of the incident acoustic vector field only when the sensor is small relative to a wavelength (e.g., $ka \ll 1$) and the sensor displaces its own mass in the fluid (e.g., neutrally buoyant). Acoustic vector sensors designed for use in seawater, including those used for this study, usually satisfy both of these conditions. Thus, the velocity transfer function for the vector sensors suspended above the seafloor was taken to be unity (e.g. $H_s^{(f)} \equiv 1$).

3.2.2 Acoustic Vector Sensor in an Elastic Solid

The mechanical impedance $Z_m^{(\varepsilon)}$ of a small, rigid spherical body embedded in marine sediment was similarly reduced to simplified form by approximating the sediment as an incompressible, elastic medium. Setting $\lambda_1 = \infty$, the impedance of

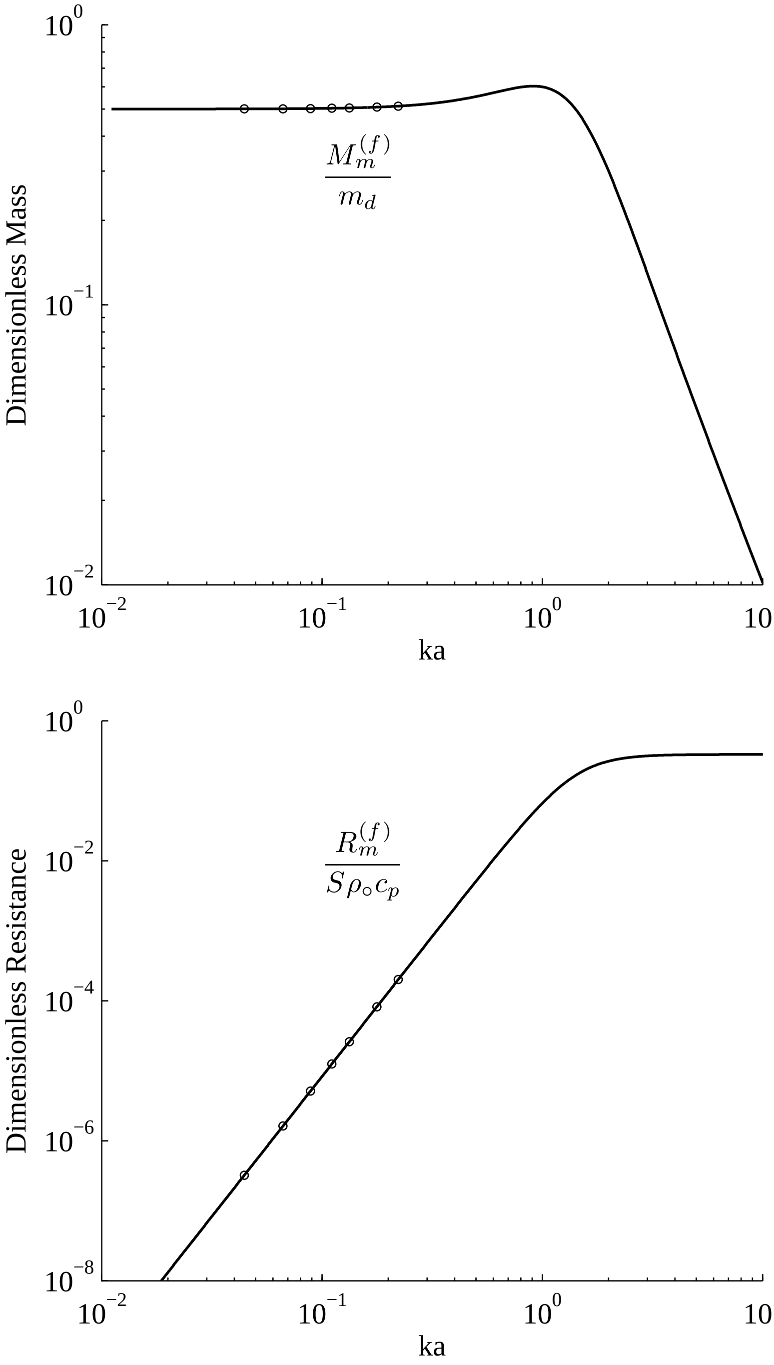

Figure 6. Immersed sensor impedance. Added mass and resistance for an acoustic vector sensor immersed in an inviscid, compressible fluid. Terms are provided in non-dimensional form as indicated in each panel. Values applicable to the vector sensors suspended above the seafloor during the SAX04 experiment are indicated with markers.

the buried sensor becomes

$$Z_m^{(\varepsilon)} = -j\omega\rho_\circ \frac{2\pi a^3}{3}\left(1 - \frac{j9}{ha} - \frac{9}{(ha)^2}\right). \tag{50}$$

An alternate form for the mechanical impedance of Eq. 50 separates the individual contributions as

$$Z_m^{(\varepsilon)} = -\left(j\omega M_m^{(\varepsilon)} + R_m^{(\varepsilon)} + \frac{1}{j\omega}K_m^{(\varepsilon)}\right) \tag{51}$$

where terms for the added mass $M_m^{(\varepsilon)}$, resistance $R_m^{(\varepsilon)}$ and stiffness $K_m^{(\varepsilon)}$ are given by

$$M_m^{(\varepsilon)} = \frac{2}{3}\pi\rho_\circ a^3, \tag{52}$$

$$R_m^{(\varepsilon)} = \frac{3}{2}S\rho_\circ c_s, \tag{53}$$

$$K_m^{(\varepsilon)} = 6\pi\rho_\circ a c_s^2, \tag{54}$$

and c_s is the shear wave speed in the sediment. As before, the surface area of the spherical body is S. The added mass $M_m^{(\varepsilon)}$ is equal to half the mass of sediment displaced by the sensor. In the case where the sediment is further approximated as lossless (e.g., $\mu_2 = 0$), the individual terms are all independent of frequency. When viscous losses are included, frequency dependent attenuations are represented in the resistance $R_m^{(\varepsilon)}$ and stiffness $K_m^{(\varepsilon)}$ as a complex shear wave speed

$$c_s = \left(\frac{\rho_\circ}{\mu_1 + j\omega\mu_2}\right)^{\frac{1}{2}}. \tag{55}$$

Figure 7 provides a comparison of the full and simplified expressions for the impedance of a buried sensor using parameters that are representative of the experimental conditions. The resistance and reactance (e.g., the real and imaginary parts of the impedance) are plotted as functions of frequency. Sediment properties were compiled from test site measurements with density (2.04 g/cm^3), compression wave speed (1680 m/s), compression wave attenuation (1.0 dB/m/kHz), shear wave speed (120 m/s) and shear wave attenuation (30 dB/m/kHz) as reported for the SAX99 [8] and SAX04 [4] experiments. The approximation error for this case is also illustrated where the specific inversion frequencies are indicated with markers. As shown in the figure, the difference between the full and simplified impedance was less than 1% throughout the measurement band, with the error tending to increase with frequency.

The full and simplified expressions for the impedance were also compared as a function of sediment shear wave speed as illustrated by Fig. 8. The comparison was performed at the upper end of the analysis band due to the generally increasing error at the higher frequencies as the finite volume elasticity of the sediment became more important. The upper panel of the figure shows good agreement between the full and simplified impedance for a wide range of sediment shear wave speeds. The lower panel of the figure provides a more detailed view of the approximation error. While the error in the resistance increased somewhat for decreasing shear wave speed, both the resistance and reactance errors were less than 2% for all probable values of this parameter.

The simplified expression for the impedance of a buried sensor Eq. 51 is in a convenient form for use in the velocity transfer function of Eq. 41. Substitution of the terms for the mechanical impedance into the Eq. 41 yields an expression for the velocity transfer function of an acoustic vector sensor embedded in a seabed approximated as an elastic solid

$$H_s^{(\varepsilon)} = \frac{j\omega\left(M_d + M_m^{(\varepsilon)}\right) + \widetilde{Z}_m^{(\varepsilon)}}{j\omega\left(M_s + M_m^{(\varepsilon)}\right) + \widetilde{Z}_m^{(\varepsilon)}}. \tag{56}$$

Terms for the resistance and stiffness of the mechanical impedance are given as

$$\widetilde{Z}_m^{(\varepsilon)} = -\left(R_m^{(\varepsilon)} + \frac{K_m^{(\varepsilon)}}{j\omega}\right) \tag{57}$$

where $M_m^{(\varepsilon)}$, $R_m^{(\varepsilon)}$ and $K_m^{(\varepsilon)}$ were provided as Eqs. 52–54.

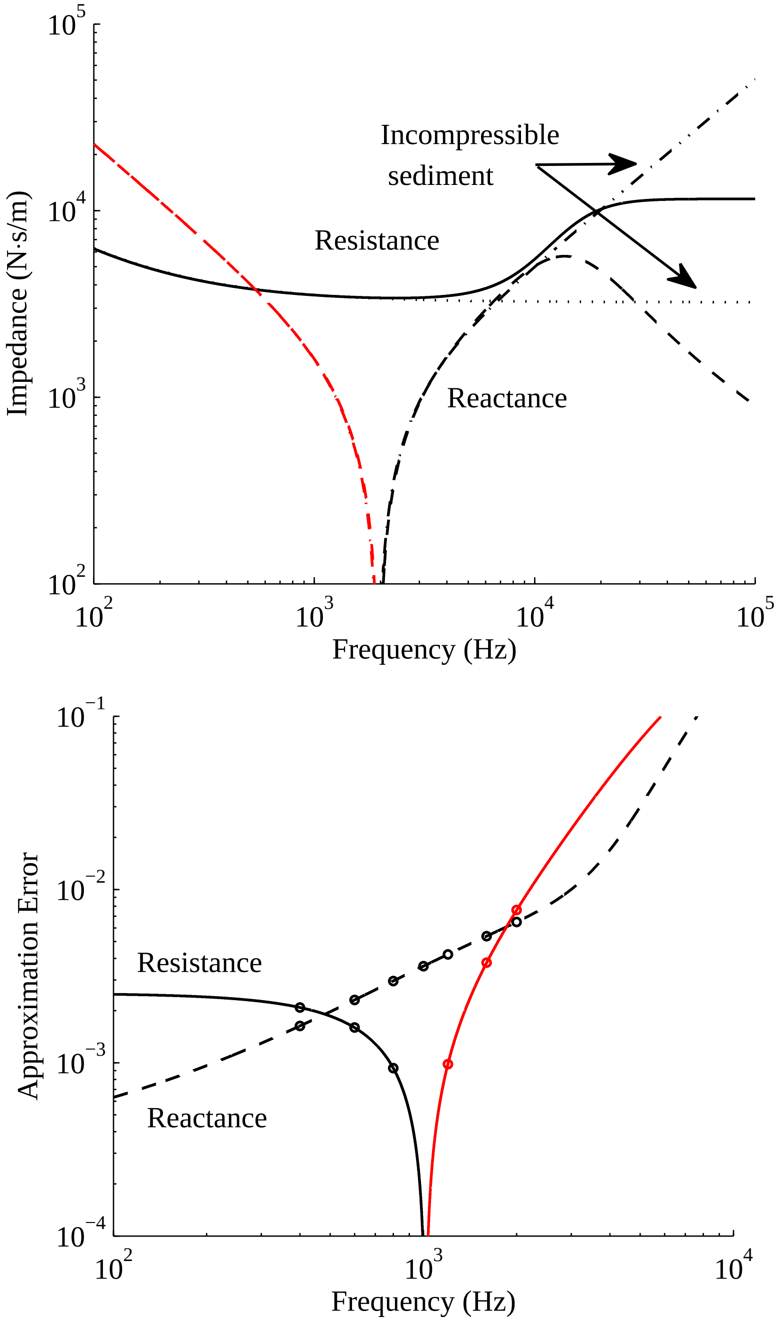

Figure 7. Buried sensor impedance: variation with frequency. Mechanical impedance and approximation error $(Z_m^{(\varepsilon)}/Z_m - 1)$ for acoustic vector senosr embedded in marine sediment. In regions where values are less than zero, the negative is shown in red to facilitate display.

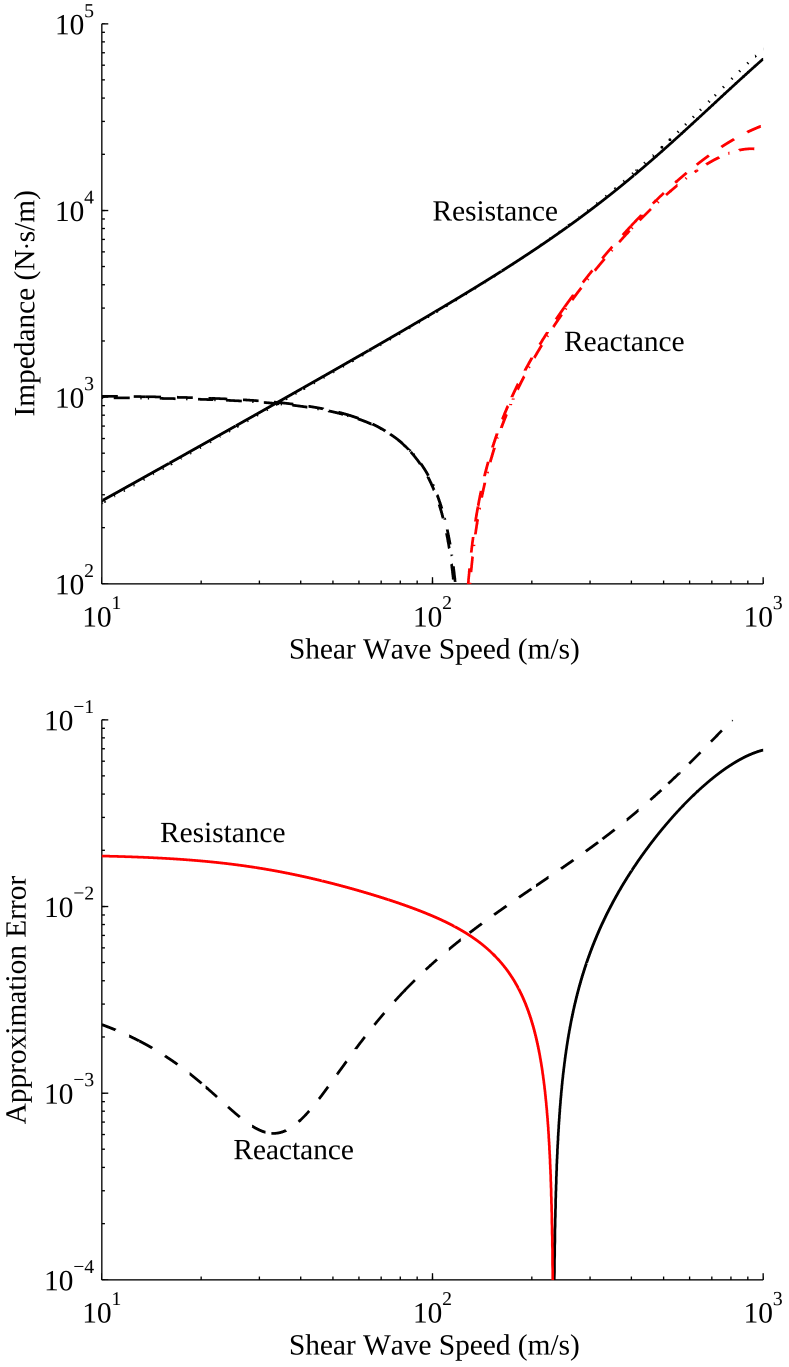

Figure 8. Buried sensor impedance: variation with shear wave speed. Mechanical impedance and approximation error at 2000 Hz ($Z_m^{(\varepsilon)}/Z_m - 1$). In regions where values are less than zero, the negative is shown in red to facilitate display.

As was the case for a vector sensor immersed in an inviscid fluid, inspection of Eq. 56 shows that the velocity of the sensor equals that of the medium in which it is embedded when the sensor displaces its own mass of embedding material, regardless of the resistance and stiffness terms for the impedance.

Analysis of the velocity transfer function Eq. 56 for the buried sensor indicates the presence of a suspension resonance within the processing band. As illustrated in Fig. 9, the resonant frequency was sensitive to the shear wave speed where it increased from 320 Hz to 1910 Hz for shear wave speeds of 25 m/s and 150 m/s, respectively. Thus, data provided by the vector channels of the buried acoustic vector sensors were quite likely to have been affected by a frequency dependent transfer function between the acoustic vector field and the data representing that field. In principle, data provided by the vector channels of the buried sensors could be corrected by compensating for the frequency dependent transfer function associated with the suspension response. However, implementation of the correction would require a priori information about the sediment shear wave speed and density; parameters that were to have been estimated by the inversion. As a result, the inversion method needed to account for unknown sediment parameters that contributed to a frequency dependent transfer function located between the acoustic vector field and data representing that field.

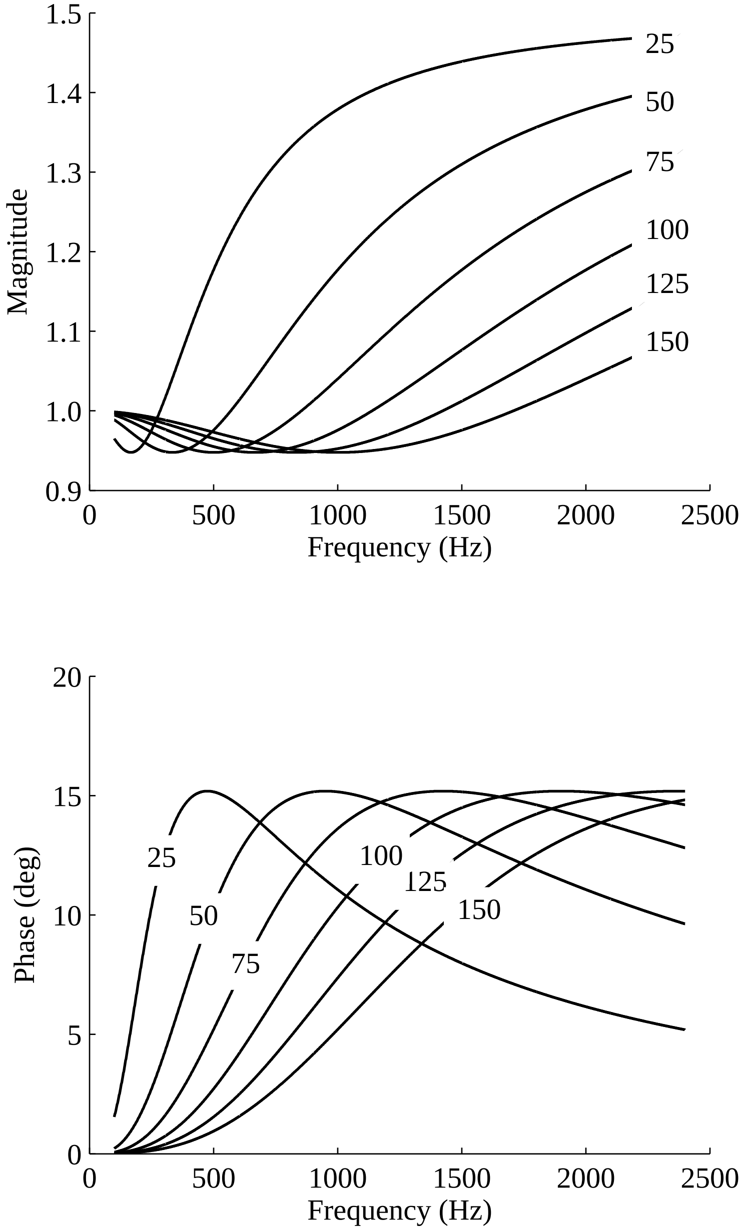

Figure 9. Buried sensor velocity transfer function $H_s^{(\varepsilon)}$. Individual curves representing shear wave speeds of 25–150 m/s are indicated in the figure.

List of References

[1] K. K. Deng, "Underwater acoustic vector sensor using transverse-response free, shear mode, PMN-PT crystal," U.S. Patent 7 066 026, 2006.

[2] *The TV-001 Miniature Vector Sensor*, Wilcoxon Research, Inc., Gaithersburg, MD, 2003.

[3] J. A. McConnell, "Analysis of a compliantly suspended acoustic velocity sensor," *Journal of the Acoustical Society of America*, vol. 113, no. 3, pp. 1395–1405, Mar. 2003.

[4] J. C. Osler, D. M. F. Chapman, P. C. Hines, G. P. Dooley, and A. P. Lyons, "Measurement and modeling of seabed particle motion using buried vector sensors," *IEEE Journal of Oceanic Engineering*, vol. 35, no. 3, pp. 516–537, July 2010.

[5] J. C. Osler and D. M. F. Chapman, "Quantifying the interaction of an ocean bottom seisometer with the seabed," *Journal of the Geophysical Research*, vol. 103, no. B5, pp. 9879–9894, May 1998.

[6] H. L. Oestreicher, "Field and impedance of an oscillating sphere in a viscoelastic medium with an application to biophysics," *Journal of the Acoustical Society of America*, vol. 23, no. 6, pp. 707–714, Nov. 1951.

[7] E. Skudrzyk, *The Foundations of Acoustics.* New York: Springer-Verlag, 1971.

[8] M. J. Buckingham, "Compressional and shear wave properties of marine sediments: Comparisons between theory and data," *Journal of the Acoustical Society of America*, vol. 117, no. 1, pp. 137–152, Jan. 2004.

CHAPTER 4

Sediment Acoustics Experiment 2004

4.1 Test Site

The SAX04 experiment was conducted in the Northern Gulf of Mexico during September–November 2004 as part of an Office of Naval Research (ONR) department research initiative on high-frequency sound interaction in ocean sediments. The objectives of the experiment were far reaching and included 1) measurement and modeling of sediment hydrodynamic, geological, and biological properties and processes that pertain to sediment geoacoustics; 2) monostatic and bistatic scattering from the seafloor; 3) scattering from discrete scatterers; 4) acoustic penetration into seafloor sediments, especially at subcritical grazing angles; 5) volume scattering and its effects on wave propagation in sediments; 6) modeling of wave propagation in sediments, including the dependence of wave speeds and attenuations on physical properties as well as frequency; and 7) acoustic detection and classification of buried objects. [1]

The experiment was conducted near the site of a previous high frequency acoustic experiment conducted in 1999 (SAX99). Among the primary considerations for selection of the test site was the need for the seafloor to have a relatively high critical angle (e.g., 25°–30°) to support the study of acoustic penetration and scattering both above and below the critical angle. This translated into a sediment-to-sound speed ratio greater than about 1.1, a condition that was satisfied by the selection of a sandy bottom. In addition, the experiment plans called for the insertion of hydrophones and acoustic vector sensors into the bottom. A surface sand layer that was at least one meter thick was required. Initially, a site near Panama City, Florida was considered, but was ultimately rejected in favor of the site off Fort Walton Beach due to the high density of mud inclusions near Panama City [2].

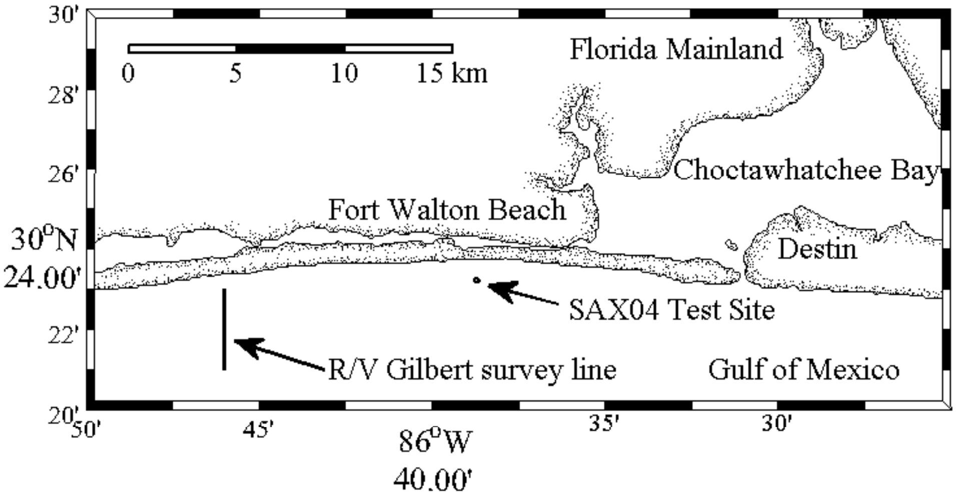

Figure 10. SAX04 experiment location. Coastline data extracted from the Global Self-consistent, Hierarchical, High-resolution Shoreline Database (GSHHS) [3]
.

The Fort Walton Beach site was selected as best satisfying the requirements of the planned experiments including sediment type, sediment homogeneity, bathymetry and shallow water. The experiment was conducted in 16.7 meters of water located one kilometer offshore of Fort Walton Beach, Florida as illustrated in Fig. 10.

Fort Walton Beach is located along the northwest Florida panhandle. The adjacent shelf is wide with generally low gradient. Surface sediments in the area are referred to as the Mississippi–Alabama–Florida (MAFLA) sand sheet lying within the Eastern Gulf sediment province. The sediments are medium to fine grained quartz sand with few accessory minerals. Grain size decreases size westward, in the direction of long-shore sediment transport. The source of sediments in the vicinity of the SAX04 test site is an eroding headland east of Destin. [4]

Santa Rosa Island is a narrow, low-profile, barrier island located directly north of the test site. The island is about 500 m wide, with Santa Rosa Sound lying between the island and the mainland Florida panhandle. Santa Rosa Sound is a

Figure 11. Storm surge during Hurricane Ivan's landfall. Photo taken at Fort Walton Beach, Florida from Wright Parkway, 1.6 km north of the coastline looking south. Image credit: Chris Duval [8].

narrow lagoon about 400 m wide, with a maximum depth of 7.5 m and is bounded on the east by Choctawhatchee Bay. Santa Rosa Island and Sound constitute part of a barrier island complex separating a series of lagoons, bays, and estuaries from the Gulf of Mexico. The estuaries north of the barrier islands are sinks for fine-grained sediment. Little sediment is transported to the Gulf except from Mobile Bay (to the west) or during hurricane events. [5]

On September 16, Hurricane Ivan made landfall 100 km west of the test site as a category 3 hurricane with sustained winds of 105 kts [6]. Ivan produced significant wave heights of 12 m at the experiment site resulting in the destruction and loss of bottom mounted equipment [7]. Photographs during the storm (see Fig. 11) and aerial reconnaissance immediately afterward indicated that parts of Santa Rosa Island were completely submerged by the 3.0 to 4.5 m storm surge.

The test site and surrounding waters were surveyed in July–August 2005, nine months after the passage of Hurricane Ivan. The survey included side scan sonar, multibeam backscatter imagery, numerous grab samples and twenty-six cores, fifteen from the SAX04 test site. The remaining cores were collected 11 km to the west of the SAX04 site, including five that were arranged in a line perpendicular to the shore in water depths ranging from 3.5 to 18 m (see Fig. 10). The cores were collected by the U.S. Geological Survey (USGS) *R/V Gilbert* using 7.6 cm diameter, six meter length aluminum barrels that were driven into the seabed with a pneumatic vibrator. Survey results were used to characterize the area, and to develop a general chronology of storm driven erosion, transport and deposition processes. [5]

Figure 12 summarizes the regional sediment profile as reflected in results of the shore-perpendicular line (see Fig. 10) of grab samples and cores collected by *R/V Gilbert*. The figure illustrates the regions depositional pattern beginning with Pleistocene deposits laid down during the last global sea-level minimum of the late Wisconsinan glacial stage. Facies 3 and 4 were deposited during the post-glacial rise in sea-level. The depositional environment was a partially enclosed estuary with deposits consisting of an organic-rich, muddy quartz sand with shells, wood and peat throughout. Continued rise in sea-level transformed the depositional environment from a partially closed estuary to an open marine environment resulting in a sand deposit (e.g., Facies 5 and 6) that is a combined 3.0–5.5 m thick. Facies 6 is the barrier island shoreface composed of well sorted quartz sand deposited and reworked by ongoing processes. [5]

Ongoing erosion, transportation and deposition processes continue to rework the surficial sediments. While redistribution and sorting of sand is a continual process, strong storms can submerge barrier island systems redistributing sand on the shelf and introducing fine grained material as sediment outflow from the

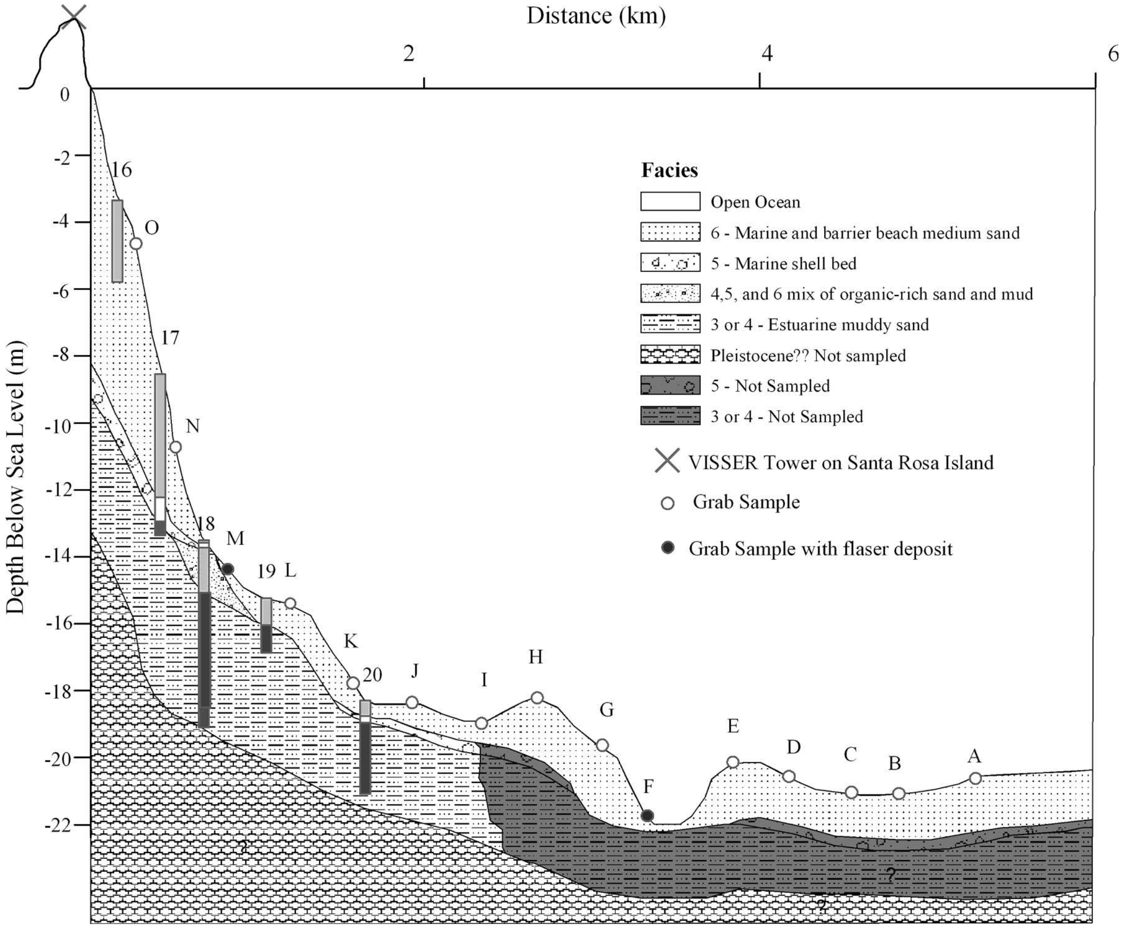

Figure 12. Mississippi–Alabama–Florida (MAFLA) sand sheet profile. Near shore sediment profile and core locations for survey line located 11 km west of the SAX04 test site. Image reproduced from [5].

bays and lagoons. Wind and wave generated currents at the base of the barrier island shoreface act to erode much of the sand sheet and allow sand and organic rich, fine grained material to mix together near the seafloor surface above the older sedimentary deposits. As a result, sediments in the upper half meter of the seabed contain layers with elevated quantities of silt, clay, wood, peat and other organic materials. Evidence of shallow mud flasers, or lenses, were found in the grab samples and cores that were collected. [5]

Four cores (e.g. 4A–4D) were taken in the immediate vicinity of the site where the acoustic data for this study were collected. Core 4A showed no evidence of layering, while core 4B contained evidence of a muddy layer at a depth of four meters. As illustrated in Fig. 13, cores 4C and 4D showed evidence of muddy layers at depths of 140 and 100 cm, respectively. It is estimated that these two cores were collected less than 20 m from the acoustic data collection site. [9]

Data collected 11 km to the west of the SAX04 test site also show evidence of a muddy layer embedded within the surface sediments. Data collected on core 25 included compression wave speed and density, from which the characteristic impedance was computed. As shown in Fig. 14, both the compression wave speed and density were significantly lower in this muddy layer than in the bounding sediments.

The sequence of events by which the SAX04 test site was affected by the landfall and passage of Hurricane Ivan was reconstructed from basic knowledge about local sedimentary processes, by observations during and immediately after the storm, and by analysis of the data collected by *R/V Gilbert* in July 2005. Following the passage of Ivan, retreating surge water transported a significant amount of mud, likely derived from Santa Rosa Sound, onto the shelf. A large, nearly continuous drape of mud was deposited at the test site and surrounding shelf

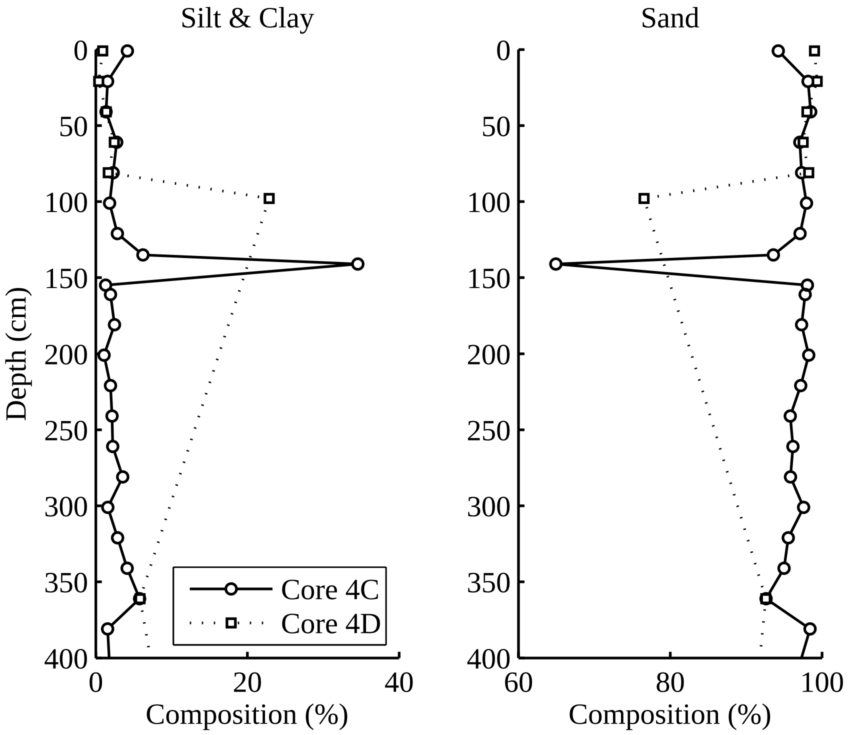

Figure 13. SAX04 core sediment composition

waters. Subsequent wind-wave activity mobilized sediment resulting in suspension and subsequent resettling of mud onto sand ripples. Lens shaped mud inclusions (e.g., flasers) within the sand sediment were created when the mud that settled into the troughs was covered by migrating sand. The result was that some mud was incorporated into the seafloor sediments. Mud lenses were protected from further suspension and transport by bottom currents. Subsequent storm events continued to break up the surface mud layer into smaller deposits, which were subsequently isolated and buried by migrating sand. Although the experiment site was selected for its well-sorted quartz sand, the presence of mud layers of limited horizontal extent created a more heterogeneous sediment than existed before the storm. [5], [10]

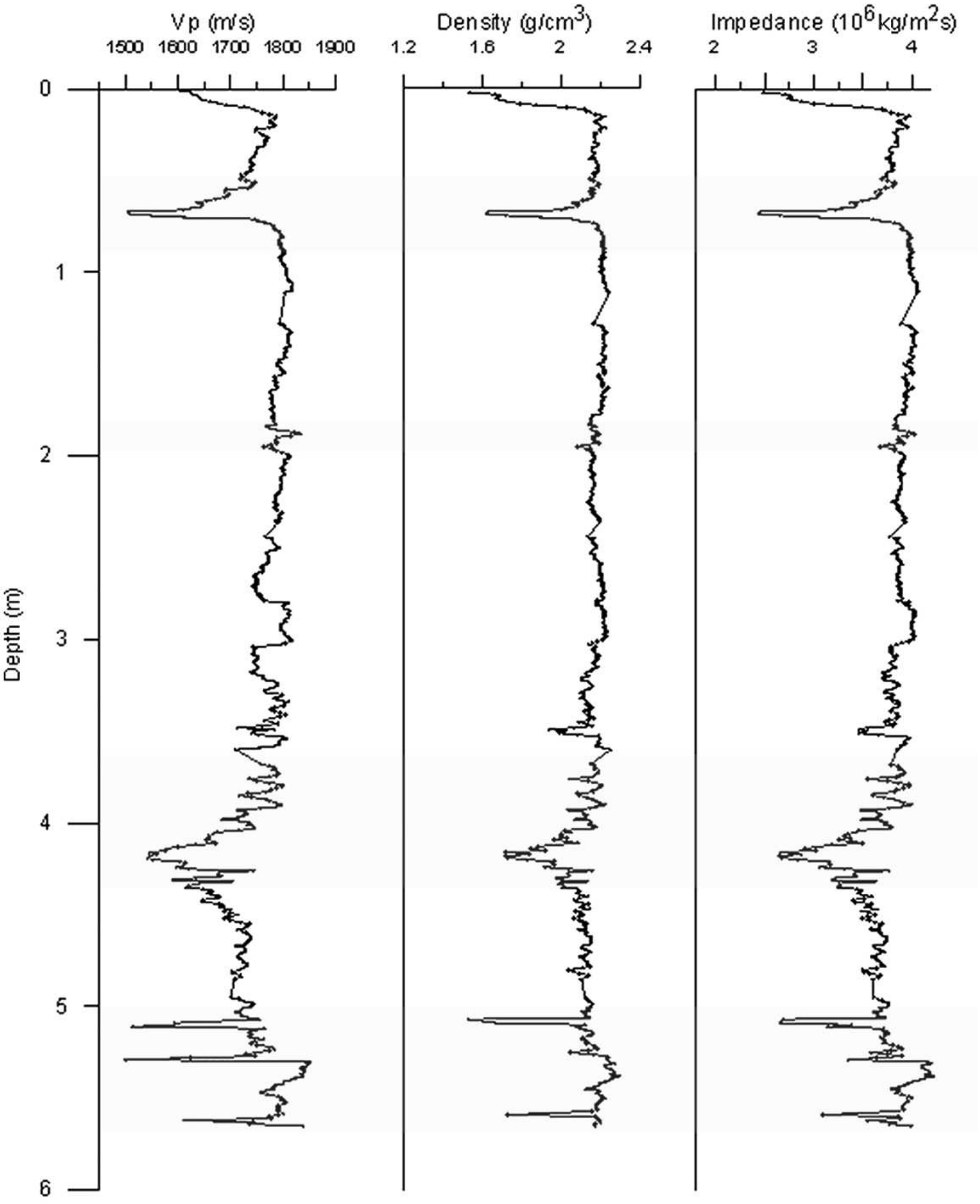

Figure 14. Multisensor core logger data. Core was taken at a located 11 km west of the SAX04 test site. A clay rich layer at a depth of 65 cm separates Facies 6 from an organic rich sand layer below. Image reproduced from [5].

4.2 Test Geometry

The SAX04 experiment was conducted from the *R/V Seward Johnson* as it lay in a four point mooring, one kilometer south of Fort Walton Beach, Florida. The experiment included several distinct components, each with its own equipment and resources. The experimental component on which this study was based was led by a team from Defence Research and Development Canada (DRDC) Atlantic. As shown in Fig. 15, DRDC equipment was located about 70 m directly astern of the ship.

Figure 16 illustrates the experimental arrangement used to collect the data on which this work was based. The experiment was conducted in a water depth of 16.7 m. An acoustic projector was suspended above the seafloor at a height above bottom of 8.4 m. Directly beneath the projector were located four Wilcoxon Research TV–001 acoustic vector sensors arranged in a vertical line that spanned the seafloor. Two sensors (e.g., VS5 and VS6) were suspended above the seafloor at heights of 10 and 25 cm, respectively. Two sensors were buried in the sediments (e.g., VS1 and VS2). The intended burial depths were 50 and 100 centimeters, although there was uncertainty in the actual burial depths as reported in [12]. All data were collected at normal incidence.

The suspended sensors were fastened by compliant elastic bands to a PVC cage as illustrated in Fig. 17 as the cage was being prepared for deployment. The buried sensor were inserted into the seabed using a purpose built burial jig designed to deposit the sensors at known depths and rotation angles as shown in the lower panel of Fig. 17. Note that while sensors were buried with non-zero horizontal displacements relative to the normal incidence arrival line, only data collected with the sensors placed for normal incidence arrivals were available for this study.

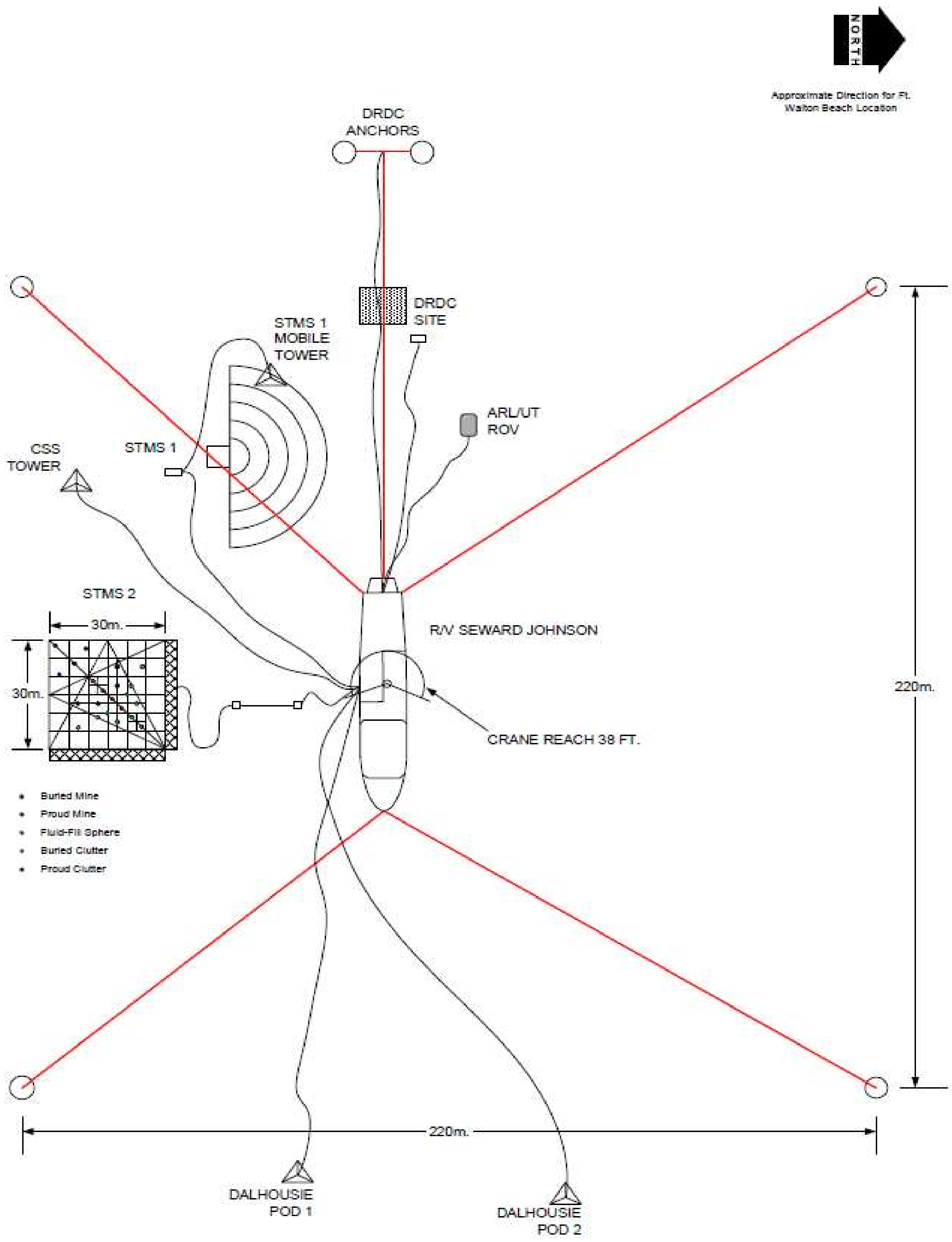

Figure 15. SAX04 test site arrangement. Image reproduced from [11].

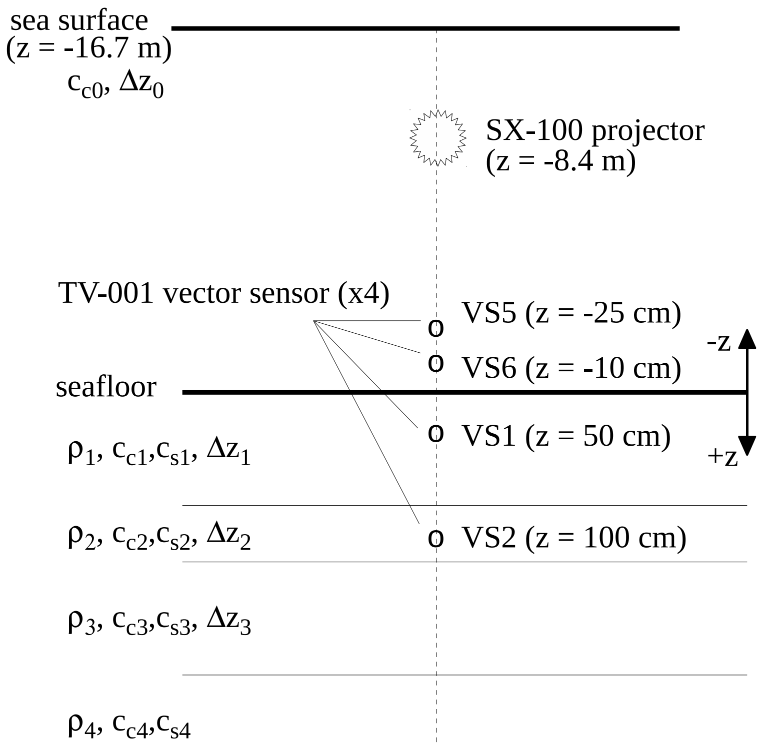

Figure 16. Acoustic data collection geometry

4.3 Measurement System

Acoustic data were collected using a Nicolet Liberty data acquisition system. The system acquired 32 simultaneously sampled data channels with 16-bit resolution. The sample rate was 40 kHz. The input range of the data channels was ±5.4613 volts, set to prevent clipping of signals received from the acoustic projector operated at a nominal source level of 175 dB re 1 μPa at 1 meter. The source-to-receiver ranges were less than 10 m for all sensors.

The noise characteristics of the data were largely controlled by the limited resolution of the Nicolet Liberty data acquisition system. Neglecting all noise sources, the theoretical dynamic range of the acoustic data was 96 dB. However, analysis of ambient noise records showed that the effective dynamic range of the system was significantly less.

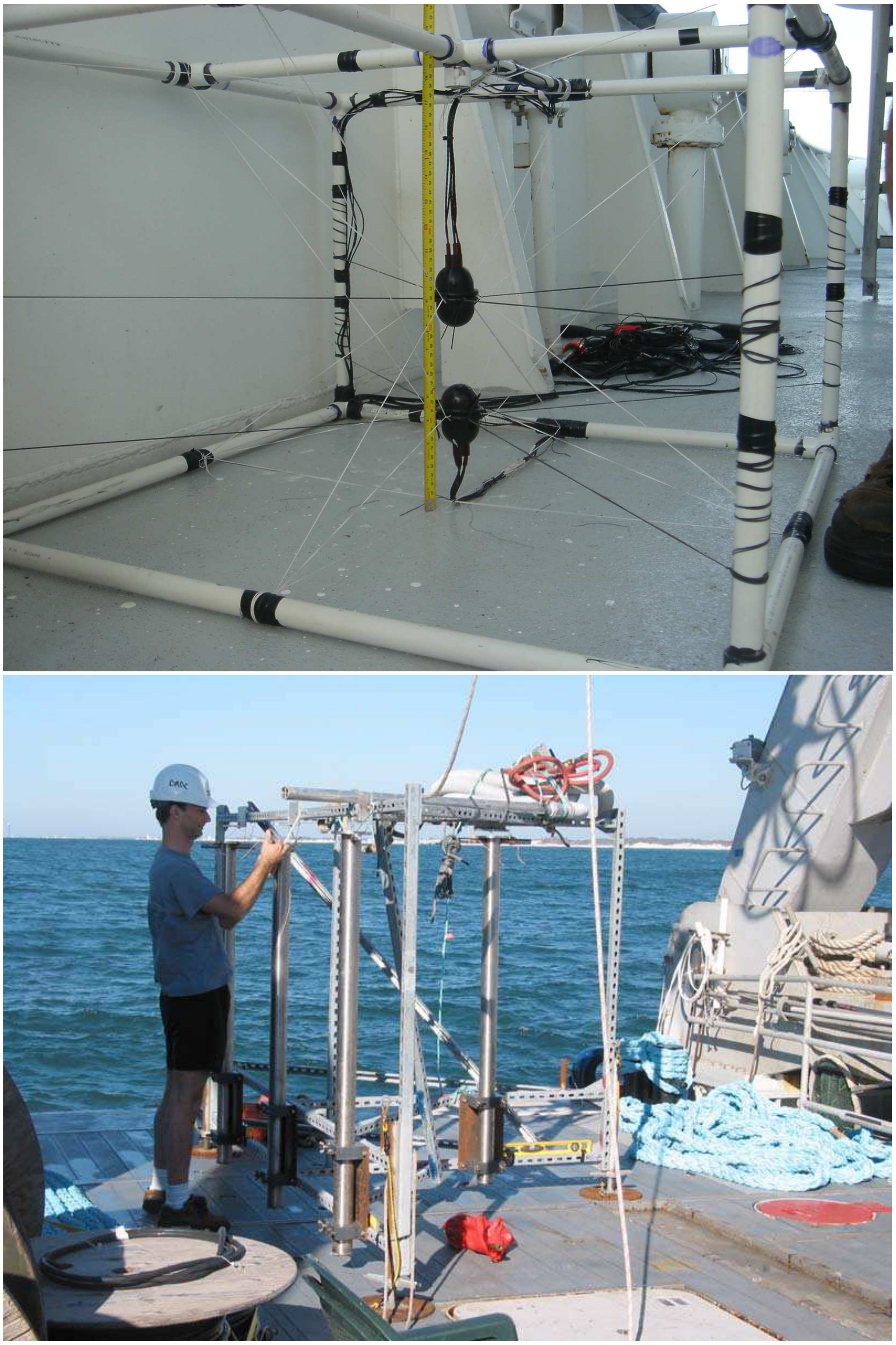

Figure 17. Acoustic vector sensor deployment fixtures. Upper panel shows PVC cage used to support the sensors at 10 and 25 cm above the seafloor. The lower panel shows the burial jig used to insert the sensors with controlled horizontal and vertical displacements and angular orientations. Images reproduced from [13].

Noise spectra for the acoustic channels of a buried vector sensor (e.g. VS1) are illustrated as Fig. 18 where electronic noise is shown to dominate the noise spectrum for the pressure channel for frequencies above about 2500 Hz. Electronic noise dominated throughout the spectrum for the acceleration channels, with the exception of a small region near 1000 Hz for the y-axis transverse channel where noise from the anchored research vessel can be seen.

Figure 19 presents the same data where the voltage spectra were converted to equivalent plane wave pressure for both the hydrophone and the accelerometers. Conversion of the voltage measured on the accelerometer V_a to equivalent plane wave pressure P_{eq} was accomplished by integration and application of the impedance ρc for a plane propagating wave as

$$|P_{eq}| = \frac{\rho c |V_a|}{\omega M_a} \tag{58}$$

where M_a is the acceleration sensitivity.

Review of the manufacturer's specifications [14] for the TV-001 vector sensor confirms that the electronic noise floor illustrated in Fig. 18 and Fig. 19 did not originate with the sensor. Wilcoxon Research specified the noise levels of the TV-001 sensor as equivalent plane wave pressure for both the hydrophone and the accelerometers. The specified noise levels at 1000 Hz were 28 and 45 dB re $\mu\text{Pa}^2/\text{Hz}$ for the hydrophone and accelerometers, respectively. Thus the specified noise levels for the sensor were well below that observed by the data acquisition system.

Noise characteristics of the data acquisition system were estimated using noise data for the vertical acceleration channel during the ambient noise measurement. The *noise-free code resolution* and *effective resolution* of the 16-bit data acquisition system were estimated using methods common to many manufacturers of electronic components, analog-to-digital converters in particular [15]. Figure 20 illustrates the noise data displayed in the output codes (e.g. bits) of the analog-

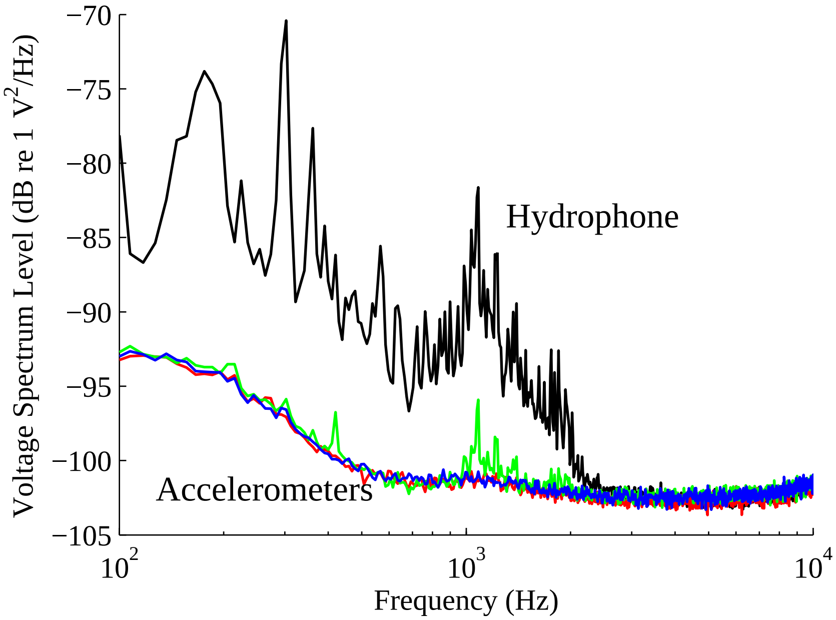

Figure 18. Vector sensor voltage noise spectrum. Data was collected with buried sensor (e.g. VS1). Electronic noise on the acceleration channels was sufficient to preclude detection of the ambient noise spectrum.

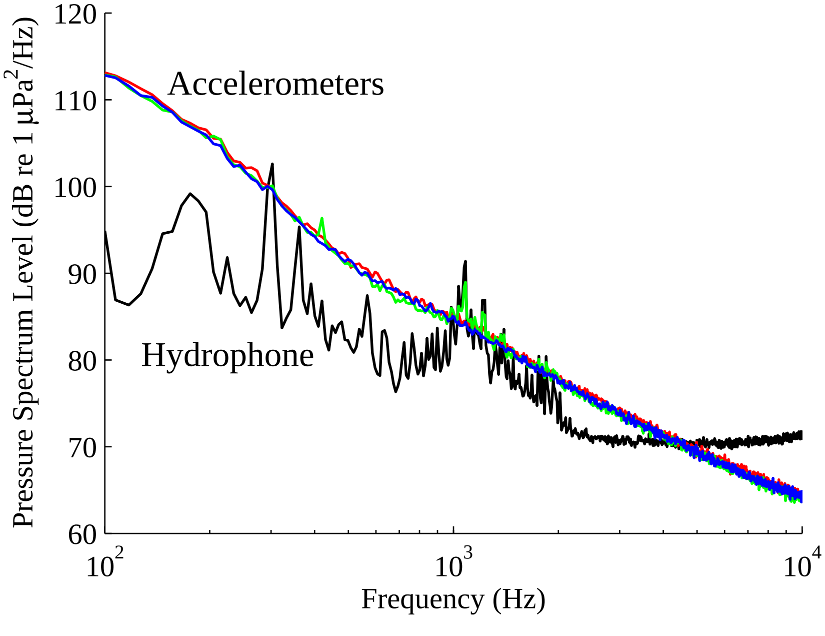

Figure 19. Vector sensor acoustic noise spectrum. Data was collected with buried sensor (e.g. VS1) and was converted to equivalent plane wave pressure.

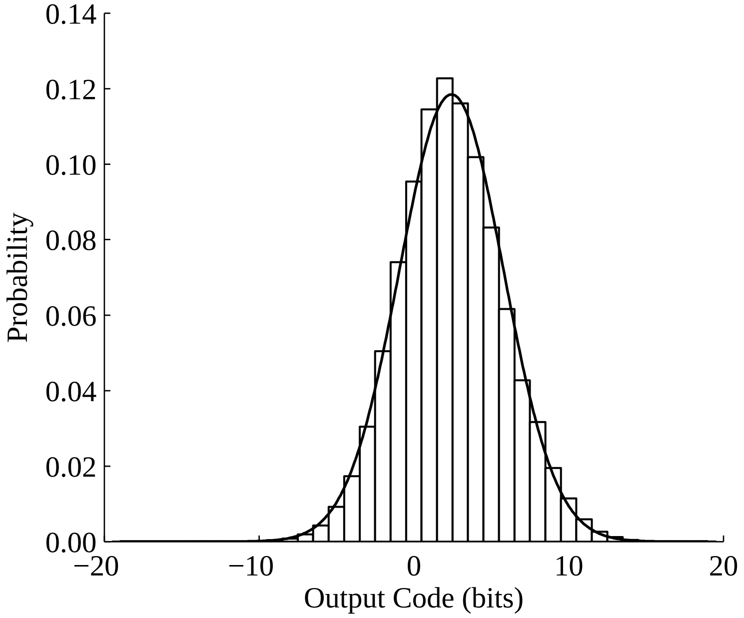

Figure 20. Vector sensor noise histogram. Data was collected with buried sensor (e.g. VS1). The resolution of the digital data was 0.167 mV/bit. The mean μ_{lsb} and standard deviation σ_{lsb} of the output were 2.4 and 3.4 bits respectively.

to-digital converter. The mean μ_{lsb} and standard deviation σ_{lsb} of the noise data were 2.4 and 3.4 bits respectively. A chi-squared goodness-of-fit test [16] of the noise data confirmed that the null hypothesis could be rejected at the 5% significance level, confirming that the noise data were Gaussian distributed. Therefore, the root-mean-squared (rms) noise output of the system was 3.4 bits, equivalent to a 0.57 mV noise source connected to the input of a noise-free analog-to-digital converter.

The *noise-free code resolution* R_{nf} of an analog-to-digital converter is the number of bits of resolution beyond which it is impossible to distinctly resolve individual output codes. This limitation is due to the effective input noise (or input-referred noise) associated with all analog-to-digital converters. The noise-free code resolution provided by a given N-bit analog-to-digital converter is

$$R_{nf} = \log_2\left(\frac{2^N}{6.6\ \sigma_{lsb}}\right) \tag{59}$$

which in the case of this data acquisition system equates to 11.5 bits where the factor of 6.6 was used to convert the root-mean-squared noise input to peak-to-peak.

The *effective resolution* R_{eff} is an alternative measure that reports the ratio of the full-scale range to the *rms* input noise (rather than peak-to-peak) as

$$R_{eff} = \log_2\left(\frac{2^N}{\sigma_{lsb}}\right) \tag{60}$$

which for the present system equates to 14.2 bits of *effective resolution.* The latter measure is cited by some manufacturers as an alternative to the *noise-free code resolution.* The realized dynamic range of the SAX04 data was estimated to be 69 dB where the *noise-free code resolution* was used to characterize the system.

4.4 Acoustic Field Data and Reduction

Processing of the SAX04 data began with band pass filtering, application of the calibration coefficients and extraction of time aligned waveforms for further processing. Alignment of the individual waveforms onto a common time base was desired to facilitate the use of complex signal representations in the inversion process. Had the signals not been aligned to a common time base, then the phase of the individual waveforms would have varied due to the process used to apply gates to the data as opposed to being influenced only by the experimental conditions, including the environment.

Filtered and calibrated time series for a buried vector sensor (e.g., VS1) are illustrated as Fig. 21. The figure shows the first five waveforms transmitted at a frequency of 800 Hz. A total of 28 waveforms were transmitted at this frequency.

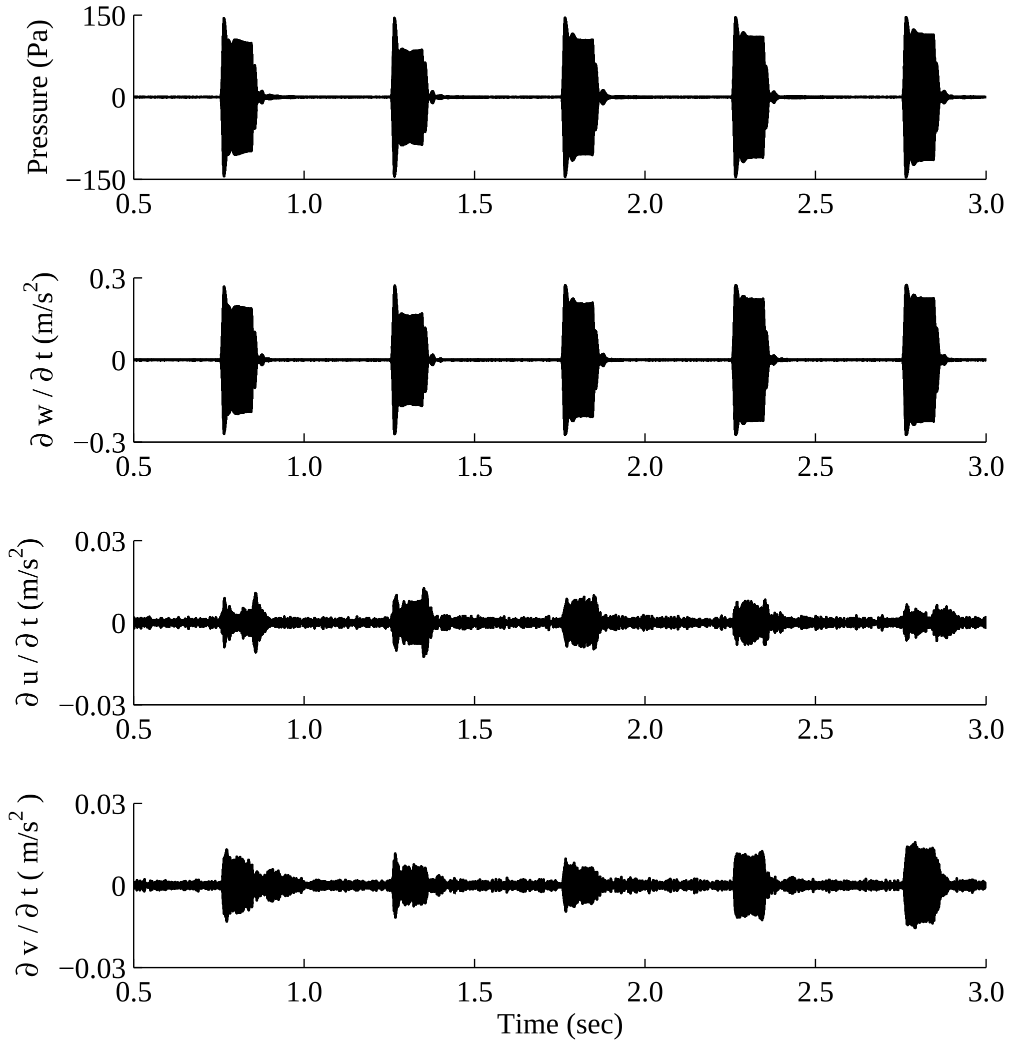

Figure 21. Acoustic waveform time series. Data was collected with buried vector sensor (e.g., VS1). The transmit frequency was 800 Hz. The pulse repetition frequency was 2.0 Hz. A total of 28 waveforms were transmitted. Data in the top panel were from the hydrophone. All other panels show data from the vector channels as acoustic particle acceleration in the vertical $\partial w/\partial t$ and horizontal $\partial u/\partial t$ and $\partial v/\partial t$ directions. Note the different vertical scales for the vertical and horizontal acoustic particle accelerations.

The acoustic pressure and all three components of the acoustic particle acceleration are shown. Note that the scale for the ordinate applied to the transverse acceleration channels, $\partial u/\partial t$ and $\partial v/\partial t$, is one tenth that of the vertical channel $\partial w/\partial t$. All data were passed through a third order Butterworth filter with bandwidth proportional to the transmit frequency. Specifically, the pass bands for the filters were one octave with the center frequency equal to the transmit frequency.

Among the questions addressed as part of the inversion process was the uncertainty in the experiment geometry. In principle, both the displacement and rotation of the the vector sensors must be defined in six degrees of freedom. Inspection of Fig. 21 shows that the magnitude of the transverse acceleration measurements were 3% to 4% of those measured in the vertical direction, suggesting a slight inclination of the vector sensor's vertical acceleration axis relative to the local wave number vector. In principle, these angles can be calculated from the relative magnitudes of the acceleration signals. However, the *transverse sensitivities* of the accelerometers were not zero (e.g. sensitivity to acceleration orthogonal to the accelerometer axis). As listed in Table 1, the transverse sensitivity of the accelerometers was specified to be less than 5%. Therefore, it was not possible to differentiate a small sensor rotation from the finite response of the accelerometers to accelerations that were orthogonal to their respective axes. As a result, the sensors were treated as having been exactly vertical and collinear along the axis for normal incidence arrivals.

Individual waveforms were gated and time aligned to facilitate the use of their complex representations in the inversion process as illustrated in Fig. 22. The trigger signal that was used to drive the acoustic projector served as the reference to which data from the other sensors were aligned. Signals from the individual vector sensors were gated and interpolated using a set of parameters

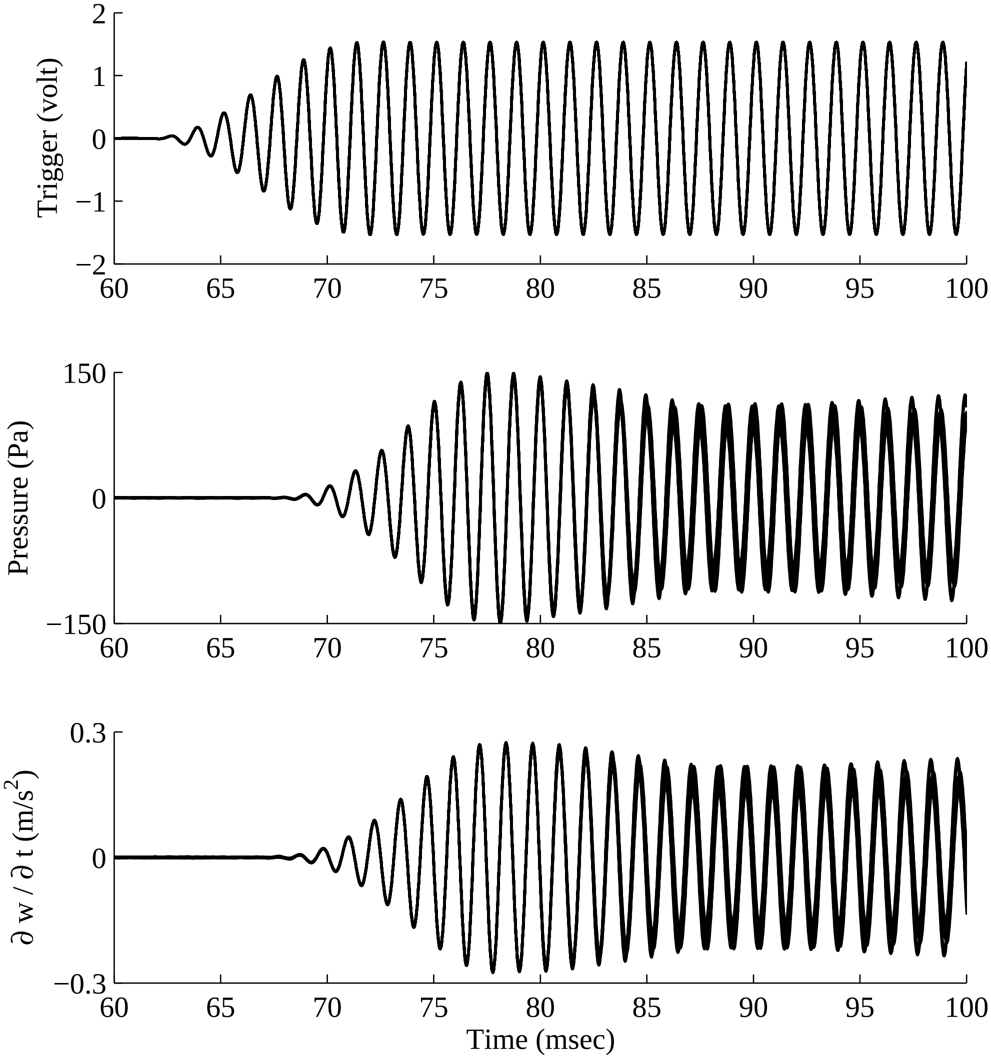

Figure 22. Gated and aligned acoustic time series. Data was collected with buried vector sensor (e.g., VS1). The transmit frequency was 800 Hz. A total of 28 waveforms are represented on a common time base prior to calculation of Fourier transformed complex signals. Alignment was performed using the trigger as the time reference. Pressure and acceleration signals show evidence of surface reflection with little scattering beginning at 80 – 85 milliseconds.

determined from the trigger. Interpolation was required because there remained an offset of a fraction of one sample between adjacent waveforms when gated to the pulse repetition period. As shown in the figure, the individual waveforms are indistinguishable for the first 15 milliseconds. There is some misalignment evident for later times once the surface reflection, and its corresponding surface scattering, arrives at the sensor.

Complex signal representations for these waveforms are presented as Fig. 23 where the acoustic pressure and particle accelerations observed at 800 Hz are displayed in the upper row. Inspection of these data shows that despite the apparently good time alignment that was achieved (see Fig. 22), scatter among the individual waveforms remained.

The lower row of Fig. 23 illustrates two distinct acoustic quantities. The left panel illustrates the scalar acoustic transfer function between a hydrophone located one meter distant from the source and the scalar channels of all four vector sensors where VS5 and VS6 were suspended above the seafloor, while VS1 and VS2 were buried within it. The close proximity of the suspended vector sensors is evident in the close grouping of data representing the individual waveform transfer functions. Likewise, the approximate quarter wavelength spacing from the suspended sensors to the shallow buried sensor (e.g., VS1) and half wavelength to the more deeply buried vector sensor (e.g., VS2) are evident. The right panel illustrates the specific acoustic impedance measured by each of the vector sensors. Perhaps the most noteworthy aspect of this representation is the significantly reduced scatter among the individual observations, suggesting that the computed impedance was less influenced by acoustic scattering and source variation.

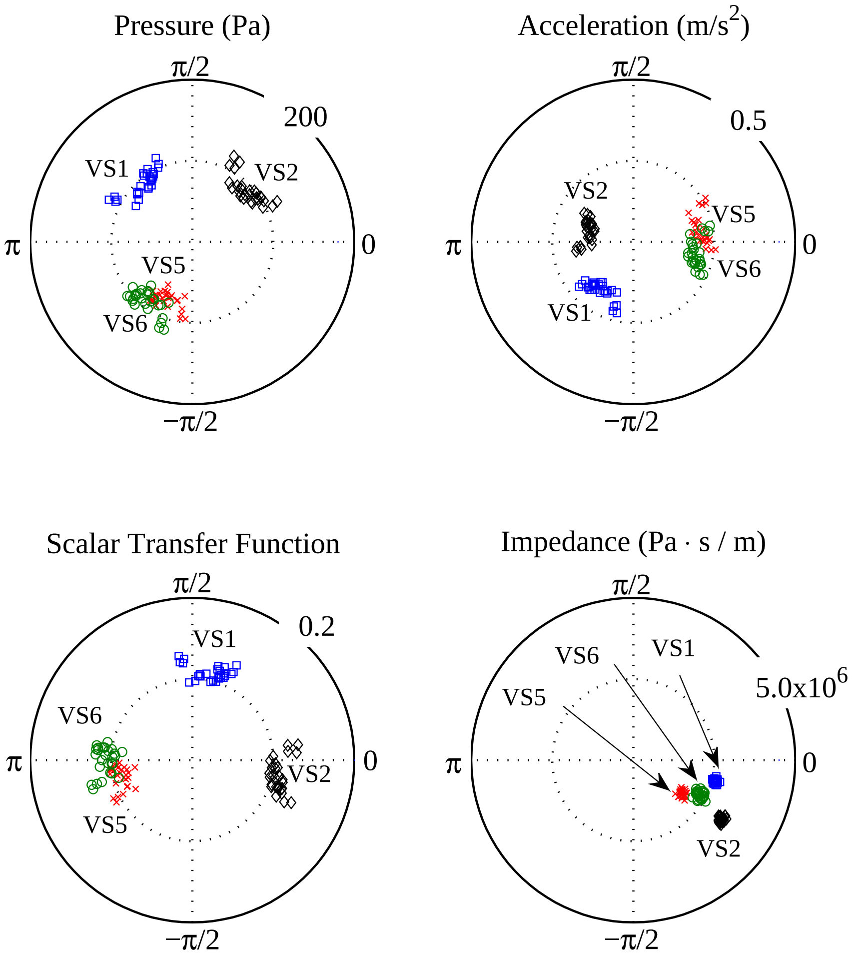

Figure 23. Complex signal representations. The transmit frequency was 800 Hz. Complex pressure and acceleration for 28 waveforms are represented. Also shown are the complex specific acoustic impedance and intensity for the received waveforms. Note the significantly decreased scatter in the calculated impedance relative to the intensity.

4.5 A Note About Notation

As this discussion has shown, the present problem was effectively reduced to a single dimension. Thus far, we have adopted the usual notation for a velocity vector as $\{u, v, w\}$ representing the $\{x, y, z\}$ components of the vector field. However, since the acoustic vector field, as observed by the sensors of this experiment, was confined to the vertical dimension z, maintenance of all three components was unnecessary.

From this point forward, the acoustic particle velocity shall be denoted as u in keeping with conventional acoustic notation, with the understanding that the vector $\mathbf{u}$ is aligned with the vertical.

List of References

[1] E. I. Thoros, M. D. Richardson, and J. F. Lynch, "Guest editorial special issue on sediment acoustic processes," *IEEE Journal of Oceanic Engineering*, vol. 33, no. 4, pp. 357–358, Oct. 2008.

[2] E. I. Thoros, K. L. Williams, N. P. Chotiors, J. T. Christoff, K. W. Commander, C. F. Greenlaw, D. V. Holliday, D. R. Jackson, J. L. Lopes, D. E. McGehee, J. E. Piper, M. D. Richardson, and D. Tang, "An overview of SAX99: Acoustic measurements," *IEEE Journal of Oceanic Engineering*, vol. 26, no. 1, pp. 4–25, Jan. 2001.

[3] National Geophysical Data Center. "A global self-consistent, hierarchical, high-resolution shoreline database." Feb. 2010. [Online]. Available: http://www.ngdc.noaa.gov/mgg/shorelines/gshhs.html

[4] L. J. Doyle and T. M. Sparks, "Sediments of the Mississippi, Alabama, and Florida (MLFA) continental shelf," *Journal of Sedimentary Research*, vol. 50, no. 3, pp. 905–915, Sept. 1980.

[5] W. C. Vaughan, K. B. Briggs, J.-W. Kim, T. S. Bianchi, and R. W. Smith, "Storm-generated sediment distribution along the northwest Florida inner continental shelf," *IEEE Journal of Oceanic Engineering*, vol. 34, no. 4, pp. 495–515, Oct. 2009.

[6] S. R. Stewart. National Hurricane Center. "Tropical cyclone report, Hurricane Ivan, 2–24 September 2004." May 2005. [Online]. Available: http://www.nhc.noaa.gov/2004ivan.shtml

[7] R. T. Guza and W. O'Reilly, "Attenuation of ocean waves by ripples on the seafloor," Scripps Institution of Oceanography, La Jolla, CA, Tech. Rep., Mar. 2007.

[8] C. Duval. Florida Division of Library and Information Services. "Storm surge during Hurricane Ivans's landfall: Fort Walton Beach, Florida." Aug. 2011. [Online]. Available: http://fpc.dos.state.fl.us/prints/pr75883.jpg

[9] P. C. Hines, J. C. Osler, J. G. E. Scrutton, and L. J. S. Halloran, "Time-of-flight measurements of acoustic wave speed in sandy sediment at 0.6–20 kHz," *IEEE Journal of Oceanic Engineering*, vol. 35, no. 3, pp. 502–515, July 2010.

[10] K. B. Briggs, A. H. Reed, D. R. Jackson, and D. Tang, "Fine-scale volume heterogeneity in a mixed sand/mud sediment off Fort Walton Beach, FL," *IEEE Journal of Oceanic Engineering*, vol. 35, no. 3, pp. 471–487, July 2010.

[11] University of Washington, Applied Physics Laboratory. "SAX04 deployment plan revision 1.2." Feb. 2007. [Online]. Available: http://www.apl.washington.edu/projects/SAX04/sax04_layout.pdf

[12] J. C. Osler, D. M. F. Chapman, P. C. Hines, G. P. Dooley, and A. P. Lyons, "Measurement and modeling of seabed particle motion using buried vector sensors," *IEEE Journal of Oceanic Engineering*, vol. 35, no. 3, pp. 516–537, July 2010.

[13] J. C. Osler, "Cruise report SAX04," Nov. 2004, unpublished.

[14] *The TV-001 Miniature Vector Sensor*, Wilcoxon Research, Inc., Gaithersburg, MD, 2003.

[15] W. Kester, *ADC Input Noise: The Good, The Bad, and The Ugly. Is No Noise Good Noise?*, Analog Devices, Norwood, MA, 2006.

[16] J. S. Bendat and A. G. Piersol, *Random Data Analysis and Measurement Procedures*, 3rd ed. New York: John Wiley and Sons, 2000.

CHAPTER 5

Inversion Method

5.1 Inverse Problem Definition

Inversion of acoustic field data is widely employed to estimate geoacoustic parameters of the ocean bottom. Specifically, geoacoustic inverse problems are designed to estimate a set of environmental parameters $\mathbf{m}$ using acoustic field data $\mathbf{d}$ and a physically realistic model f relating the parameters to the data. The fundamental relationship employed by the inverse problem is summarized by Eq. (61)–(63), where T signifies the transpose operator. [1]

$$\mathbf{d} = \left[d_1, d_2, d_3, \cdots, d_N\right]^T \tag{61}$$

$$\mathbf{m} = \left[m_1, m_2, m_3, \cdots, m_M\right]^T \tag{62}$$

$$\mathbf{d} = f\left(\mathbf{m}\right) \tag{63}$$

The problem of parameter estimation, then becomes one of inverting Eq. (63) to provide an estimate of the geoacoustic parameters using the acoustic field data as input.

$$\mathbf{m} = f^{-1}\left(\mathbf{d}\right) \tag{64}$$

Various methods exist to compute the inverse Eq. (64). In the simplest case, the data are linearly related to the parameters and the problem can be cast as a linear system of equations solved by matrix inversion. However, for most geoacoustic problems of practical interest, the data are non-linearly related to the parameters. Therefore, the geoacoustic inverse problem is typically posed as a non-linear optimization problem that includes a global search strategy to minimize the error between the acoustic field data and fields that are computed for specific instances of the parameter set as indicated by Eq. (65).

$$\mathbf{e}\left(\mathbf{m}\right) = \mathbf{d} - f\left(\mathbf{m}\right) \tag{65}$$

The inverse problem then becomes a search for the set of parameters that minimizes the error between the data and the model output. The parameter set $\mathbf{m}_\circ$ that successfully minimizes this error is taken as the best estimate of the geoacoustic parameters of interest. In short, the objective is to "estimate environmental characteristics from measured acoustic field values, with the aid of a physically realistic computational model" [2] and an efficient global search strategy.

5.2 Objective Function

An objective function ϕ was derived to facilitate both the global search strategy and to estimate the associated uncertainties in the parameter estimates. Among the attributes of the desired objective function were that it was 1) based on a known functional form with a history of good performance in similar inversion approaches; 2) normalized in a way that simplified interpretation of results; and 3) weighted individual measurements by the inverse of their respective variances.

Careful selection of the objective function has a considerable influence over the performance of any inversion approach. Objective functions based on the Euclidean norm have been shown to provide good performance for complex error vectors [3]. Thus, derivation of the objective function began by taking the Euclidean norm of the error vector, Eq. (65), to yield

$$\|\mathbf{e}\left(\mathbf{m}\right)\| = \sqrt{\left(\mathbf{d} - f\left(\mathbf{m}\right)\right)^{H}\left(\mathbf{d} - f\left(\mathbf{m}\right)\right)} \tag{66}$$

where both the data $\mathbf{d}$ and forward model predictions f were assumed complex, with H the Hermitian transpose. A more compact expression for Eq. 66, adopted for this study, is provided as Eq. 67 where the dependence of the error on the model has been suppressed.

$$\|\mathbf{e}\| = \sqrt{\mathbf{e}^H\mathbf{e}} \tag{67}$$

Equation 67 was normalized by the Euclidean norm of the data vector to define an objective function that simplified interpretation of the inversion results.

$$\phi\left(\mathbf{m}\right)_{unweighted} = \left(\frac{\mathbf{e}^H\mathbf{e}}{\mathbf{d}^H\mathbf{d}}\right)^{\frac{1}{2}} \tag{68}$$

Finally, Eq. 68 was modified to provide data exhibiting lower variance with proportionally greater influence. The errors were weighted by taking the inner product of the error vector **e** and weight vector **w** to yield Eq. 69, a normalized and weighted objective function based on the Euclidean norm of the error vector.

$$\phi\left(\mathbf{m}\right)_{weighted} = \left(\frac{\left(\mathbf{w}\cdot\mathbf{e}\right)^H\left(\mathbf{w}\cdot\mathbf{e}\right)}{\mathbf{d}^H\mathbf{d}}\right)^{\frac{1}{2}} \tag{69}$$

The weights **w**, provided as Eq. 70, were conservative in the sense that they summed to the number of observations. Thus, they provided greater weight to measurements with lower variance, without compromising the normalization of the objective function introduced in Eq. 68

$$\mathbf{w} = \frac{N_{obs}}{\displaystyle\sum_{n=1}^{N_{obs}}\frac{|d_n|}{\sigma_n}}\left[\frac{|d_1|}{\sigma_1},\frac{|d_2|}{\sigma_2},\frac{|d_3|}{\sigma_3},\cdots,\frac{|d_N|}{\sigma_N}\right]^T, \tag{70}$$

and σ_n is the standard deviation of the n^{th} observation.

5.3 Uncertainty Estimates

A complete solution to an inverse problem includes not only the parameter estimates, but some measure of the uncertainties in those estimates. Thus, assessment of the value represented by the information in the acoustic vector field considered both the parameter estimates and their associated uncertainties. This was accomplished through implementation of an empirical method to characterize the uncertainties in the geoacoustic parameter estimates for different approaches to the inversion of acoustic scalar and vector field data.

Parameter uncertainty in non-linear inverse problems is typically expressed as the *a posteriori* probability distribution [4]. This study adopted a maximum likelihood approach [5] where the *a priori* P and *a posteriori* G probability distributions are related through a likelihood function L as indicated by Eq. 71.

$$G\left(\mathbf{m}\right) = L\left(\mathbf{m}\right) P\left(\mathbf{m}\right) \tag{71}$$

The one-dimensional marginal *a posteriori* probability density function for the i^{th} parameter $G_i(m_i)$ is provided by integrating the M dimensional probability density with respect to all parameters m_j for $j = 1, 2, \cdots, M$ and $i \neq j$ to yield

$$G_i\left(m_i\right) = \int \cdots \int G\left(\mathbf{m}\right) dm_1 \cdots dm_{i-1}\ dm_{i+1} \cdots dm_M. \tag{72}$$

Evaluation of Eq. 72 may be accomplished by several means including grid search, Monte Carlo and importance sampling. Grid search is a computationally impractical approach when the number of parameters in the model vector is larger than about four. Monte Carlo methods sample the distributions randomly as a means to reduce the computational work to estimate the integrals, but may spend a significant fraction of the computational effort in regions that contribute little to the value of the integral. Importance sampling attempts to exploit some knowledge about the integrands to develop non-uniform sampling distributions that concentrate in areas that contribute most to the integral. Nonlinear optimization approaches such as genetic algorithms and simulated annealing employ such importance sampling. These approaches use a generating distribution for selecting the next model vector. However, this distribution is unknown and evolves over the course of the optimization.

When performing a non-linear inversion, one generates a large number of observations of candidate solutions N_{obs} from the total model parameter space $\mathbf{M}$.

The objective function values associated with these model runs can be used to approximate the above integrals. The *a posteriori* probability distribution for the k^{th} model vector using the N_{obs} observations is provided as

$$\widehat{G}\left(\mathbf{m}_k\right) = \frac{L\left(\mathbf{m}_k\right) P\left(\mathbf{m}_k\right)}{\displaystyle\sum_{j=1}^{N_{obs}} L\left(\mathbf{m}_j\right) P\left(\mathbf{m}_j\right)}. \tag{73}$$

For the i^{th} parameter m_i in the model vector, the marginal probability distribution for obtaining the particular value K can be estimated using Eq. 74

$$\widehat{G}_i\left(K\right) = \sum_{k=1}^{N_{obs}} \widehat{G}\left(\mathbf{m}_k\right) \delta\left(m_{k,i} - K\right). \tag{74}$$

Since, the likelihood function is usually related to the objective function $\phi(\mathbf{m})$ through an exponential, an estimate of the empirical likelihood function is

$$L_{emp}\left(\mathbf{m}\right) = \exp\left(\frac{-\left(\phi\left(\mathbf{m}\right) - \phi\left(\mathbf{m}_\circ\right)\right)}{T}\right) \tag{75}$$

where $\mathbf{m}_\circ$ is the estimated parameter vector for the optimum value of the objective function and T is a constant that is particular to each optimization. A common value for T is the average of the 50 best objective functions obtained during the optimization minus the best value of the objective function

$$T = \frac{1}{50}\sum_{n=1}^{50} \phi\left(\mathbf{m}_n\right) - \phi\left(\mathbf{m}_\circ\right). \tag{76}$$

5.4 Geoacoustic Model

A geoacoustic model was implemented that would 1) permit the comparison of inversion performance with and without use of the vector field data; and 2) address the physical complexity reported for the experiment site. The acoustic field variable upon which a given inversion scheme operates has often been derived from the acoustic transfer function between two or more spatial coordinates and frequently contains less information than the transfer function itself. As two examples consider inversion schemes based on measured transmission loss of a narrow band signal and mode dispersion for a broadband signal. In the case of the former, the transmission loss curve is simply the magnitude of the complex, range dependent transfer function between a set of source–receiver coordinate pairs with increasing separation. Similarly, the set of mode dispersion curves between two spatial coordinates is related to the phase of the complex, frequency dependent transfer function between these coordinates. Therefore, an inversion method that operates directly on complex acoustic transfer functions may have an informational advantage relative to one that operates on an incomplete representation of the transfer function.

In addition to the potential informational advantage gained by inverting the complex acoustic transfer function, the method lends itself to performance comparisons among competing approaches involving the acoustic scalar and vector fields. For example, comparing the performance of inversion schemes operating on the instantaneous intensity or specific acoustic impedance with approaches based solely on the scalar acoustic field would be complicated by the lack of an obvious scalar analogue to the vector field quantities. On the contrary, comparison of inversions performed using the scalar and vector transfer functions is straight forward.

5.4.1 Geoacoustic Parameterization

The parameter set comprising the physical geoacoustic model was developed to reflect the reported complexity of the experiment site. Acoustic data collected at the site was consistent with the presence of a low impedance reflector located within the top meter of sediment [6]. Evidence for a second reflector at a depth of 3.43 m was also reported [7]. A geoacoustic model with horizontal stratification sufficient for the reported environment is illustrated in Fig. 24. The model included the water

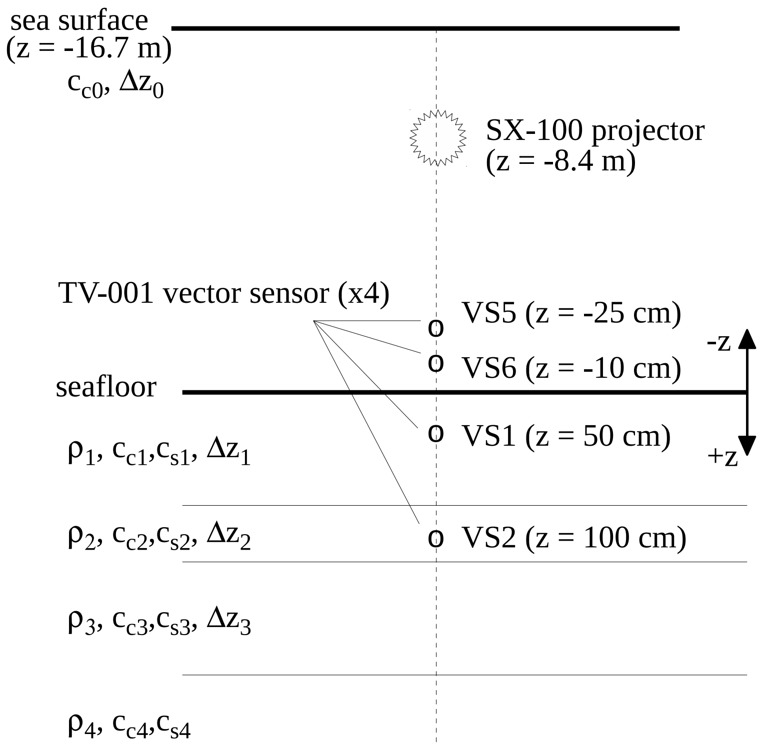

Figure 24. Model of experiment for inversions

column, three sediment layers and a sediment half-space. It was described by a total of 17 geoacoustic parameters including layer thicknesses Δz_n, densities ρ_n, compression wave speeds c_{c_n} and shear wave speeds c_{s_n}. Geoacoustic parameters were bounded to preclude the expenditure of computational effort on non-physical or unrealistic values as shown in Table 2.

Due to the experimental arrangement, few acoustic propagation codes were available to support the inversion process. An acoustic model was needed that 1) provided both the acoustic scalar and vector fields; 2) included both compression and shear waves; 3) provided accurate results in the acoustic near field, the acoustic far field and the transition between them. As a result OASES [8], a seismo-acoustic code based on wavenumber integration, was selected as the best option to satisfy these requirements.

Table 2. Geoacoustic model parameterization

Symbol	**Parameter**	**Layer**	**Bounds**		**Units**
			Lower	Upper	
Δz_0	Depth	Water Column	16.0	17.5	m
c_{c_0}	Sound Speed	Water Column	1500	1550	m/s
Δz_1	Thickness	Sediment Layer 1	0	2	m
ρ_1	Density	Sediment Layer 1	1.0	2.5	g/cm^3
c_{c_1}	Sound Speed	Sediment Layer 1	1400	2800	m/s
c_{s_1}	Shear Speed	Sediment Layer 1	0	200	m/s
Δz_2	Thickness	Sediment Layer 2	0	2	m
ρ_2	Density	Sediment Layer 2	1.0	2.5	g/cm^3
c_{c_2}	Sound Speed	Sediment Layer 2	1400	2800	m/s
c_{s_2}	Shear Speed	Sediment Layer 2	0	200	m/s
Δz_3	Thickness	Sediment Layer 3	0	2	m
ρ_3	Density	Sediment Layer 3	1.0	2.5	g/cm^3
c_{c_3}	Sound Speed	Sediment Layer 3	1400	2800	m/s
c_{s_3}	Shear Speed	Sediment Layer 3	0	200	m/s
ρ_4	Density	Sediment Half Space	1.0	2.5	g/cm^3
c_{c_4}	Sound Speed	Sediment Half Space	1400	2800	m/s
c_{s_4}	Shear Speed	Sediment Half Space	0	200	m/s

5.4.2 Acoustic Field Computations

Taking a linear systems approach to the problem, the scalar acoustic field at any position $\vec{r}_n$ is computed as the convolution of a source pressure $p\left(t, \vec{r}_1\right)$ located at position $\vec{r}_1$ with the impulse response function $h_a^{(p)}\left(t, \vec{r}_1, \vec{r}_n\right)$ for the acoustic channel between the source $\vec{r}_1$ and receiver $\vec{r}_n$ positions. Equation 77 illustrates the relation, in addition to the frequency domain representation provided by the Fourier transform of the convolution integral. An equivalent expression yielding the acoustic vector field $u_\circ\left(t, \vec{r}_n\right)$ at position $\vec{r}_n$ based on the scalar field $p\left(t, \vec{r}_1\right)$ at position $\vec{r}_1$ is provided as Eq. 78. All of the acoustic computations performed for this study were based on these fundamental relationships.

$$p\left(t, \vec{r}_n\right) = h_a^{(p)}\left(t, \vec{r}_1, \vec{r}_n\right) * p\left(t, \vec{r}_1\right) \Leftrightarrow P\left(\omega, \vec{r}_n\right) = H_a^{(p)}\left(\omega, \vec{r}_1, \vec{r}_n\right) P\left(\omega, \vec{r}_1\right) \tag{77}$$

$$u_\circ\left(t, \vec{r}_n\right) = h_a^{(u)}\left(t, \vec{r}_1, \vec{r}_n\right) * p\left(t, \vec{r}_1\right) \Leftrightarrow U_\circ\left(\omega, \vec{r}_n\right) = H_a^{(u)}\left(\omega, \vec{r}_1, \vec{r}_n\right) P\left(\omega, \vec{r}_1\right) \tag{78}$$

The OASES-OASP code for wide band transfer functions was used for all acoustic field calculations. The code calculates the depth-dependent Green's function for a selected number of frequencies and determines the transfer function between the source and a receiver at any position by evaluating the wavenumber integral. In this way both the scalar $H_a^{(p)}\left(\omega, \vec{r}_1, \vec{r}_n\right)$ and vector $H_a^{(u)}\left(\omega, \vec{r}_1, \vec{r}_n\right)$ acoustic transfer functions between the source and receivers were readily computed.

5.4.3 Buried Sensor Suspension Response

As will be detailed in Chapters 6 and 7, distinct inversion approaches were implemented. Particular acoustic quantities that were inverted were acoustic transfer functions between pairs of sensors and specific acoustic impedance measured at each sensor position. As a result, the forward model used to support the inversions needed to account for the velocity transfer function $H_s^{(\varepsilon)}$ for the buried sensor suspension response.

The scalar and vector acoustic transfer functions between the source and a receiver were provided by Eq. 77 and Eq. 78, abbreviated here as

$$P\left(\omega,\vec{r}_n\right)=H_a^{(p)}\left(\omega,\vec{r}_1,\vec{r}_n\right)P\left(\omega,\vec{r}_1\right), \tag{79}$$

$$U_\circ\left(\omega,\vec{r}_n\right)=H_a^{(u)}\left(\omega,\vec{r}_1,\vec{r}_n\right)P\left(\omega,\vec{r}_1\right), \tag{80}$$

where $U_\circ$ is the acoustic particle velocity in the sediment, not necessarily that of the sensor case. Thus, the scalar and vector acoustic transfer functions between the locations occupied by sensor m and sensor n are given by Eq. 81 and Eq. 82 where the respective positions of the sensors are $\vec{r}_m$ and $\vec{r}_n$

$$H_a^{(p)}\left(\omega,\vec{r}_m,\vec{r}_n\right)=\frac{P\left(\omega,\vec{r}_n\right)}{P\left(\omega,\vec{r}_m\right)}=\frac{H_a^{(p)}\left(\omega,\vec{r}_1,\vec{r}_n\right)}{H_a^{(p)}\left(\omega,\vec{r}_1,\vec{r}_m\right)}, \tag{81}$$

$$H_a^{(u)}\left(\omega,\vec{r}_m,\vec{r}_n\right)=\frac{U_\circ\left(\omega,\vec{r}_n\right)}{U_\circ\left(\omega,\vec{r}_m\right)}=\frac{H_a^{(u)}\left(\omega,\vec{r}_1,\vec{r}_n\right)}{H_a^{(u)}\left(\omega,\vec{r}_1,\vec{r}_m\right)}. \tag{82}$$

The forward model used to support the inversion was required to predict not only the acoustic field variables, but also to consider any distortion to measurements of the acoustic particle velocity that resulted from the suspension response. This required replacement of the acoustic particle velocity $U_\circ$ with the velocity of the sensor case U_s in the forward model. Thus, between any two sensors, the observed vector acoustic transfer function $\widehat{H}_a^{(u)}$ becomes

$$\widehat{H}_a^{(u)}\left(\omega,\vec{r}_m,\vec{r}_n\right)=\frac{U_s\left(\omega,\vec{r}_n,\rho_n,c_{s_n}\right)}{U_s\left(\omega,\vec{r}_m,\rho_m,c_{s_m}\right)}=\frac{H_a^{(u)}\left(\omega,\vec{r}_1,\vec{r}_n\right)H_s^{(\varepsilon)}\left(\omega,\rho_n,c_{s_n}\right)}{H_a^{(u)}\left(\omega,\vec{r}_1,\vec{r}_m\right)H_s^{(\varepsilon)}\left(\omega,\rho_m,c_{s_m}\right)} \tag{83}$$

where $H_s^{(\varepsilon)}$ is the velocity transfer function for the suspension response, and ρ_n, c_{s_n} are the density and shear wave speed at the location of the n^{th} sensor. Recall that the velocity transfer function for sensors suspended above the seafloor was taken to be unity $H_s^{(f)}\equiv 1$.

The specific acoustic impedance observed by the n^{th} sensor was computed similarly, where the impedance observed by a suspended sensor is

$$Z_a^{(f)}\left(\omega,\vec{r}_n\right)=\frac{P\left(\omega,\vec{r}_n\right)}{U_\circ\left(\omega,\vec{r}_n\right)}=\frac{H_a^{(p)}\left(\omega,\vec{r}_1,\vec{r}_n\right)}{H_a^{(u)}\left(\omega,\vec{r}_1,\vec{r}_n\right)}, \tag{84}$$

and the impedance observed by a buried sensor is

$$\widehat{Z}_a^{(\varepsilon)}\left(\omega,\vec{r}_n\right)=\frac{P\left(\omega,\vec{r}_n\right)}{U_s\left(\omega,\vec{r}_n,\rho_n,c_{s_n}\right)}=\frac{H_a^{(p)}\left(\omega,\vec{r}_1,\vec{r}_n\right)}{H_a^{(u)}\left(\omega,\vec{r}_1,\vec{r}_n\right)H_s^{(\varepsilon)}\left(\omega,\rho_n,c_{s_n}\right)}. \tag{85}$$

5.5 Differential Evolution

Evolutionary algorithms have been widely used to solve optimization problems, including various geophysical inverse problems [4], [9], [10], [11]. Differential evolution is a particular evolutionary algorithm [12] proposed to solve optimization problems in continuous search spaces. It is a population based stochastic heuristic characterized by simplicity, effectiveness and robustness.

Differential evolution shares some similarities with more traditional evolutionary algorithms. However, in contrast to the more common genetic algorithms, it does not use binary encoding nor does it use a probability density function to self-adapt its parameters as an evolution strategy. Instead, differential evolution performs mutation based on the distribution of the solutions in the current population. In this way, search directions and possible step sizes depend on the locations of the individuals selected to calculate the mutation vectors.

Differential evolution uses only three parameters to control its operation; the population size N_{pop}, a scale factor F, and a crossover rate CR governing the process of recombination. The population size N_{pop} is the number of individuals evaluated with each generation, typically ten times the dimensionality of the problem. The scale factor F controls the step size used in the calculation of mutation values with higher values associated with more vigorous exploration of the search space. The crossover rate CR controls the influence of mutations in the generation of offspring, with higher values tending to emphasize mutant traits at the expense of those belonging to the parent.

5.5.1 Differential Evolution Variants

A system of nomenclature to identify the variants of the differential evolution algorithm has been widely adopted. The most popular algorithm variant is identified as *DE/rand/1/bin* where "*DE*" refers to differential evolution, "*rand*" indicates that individuals are selected at random to compute the mutation values, "*1*" is the number of member pairs used to compute a difference vector and "*bin*" specifies that binomial recombination is used.

Algorithm variants differ in their mutation and recombination operators. The mutation operators vary in the number of member pairs used to develop mutations, and in the relative influence given the best member of the population in the formation of the trial vectors. The variants also differ in the way traits are selected for incorporation into the trial vectors to define distinctly different recombination processes.

Mutation

Mutation in differential evolution has the role of constructing mutant vectors by perturbing elements of the current population. The unique feature of the mutation operator is that the perturbation term is related to the difference between randomly selected members of the population. The operator functions as a self-referential mutation that results in gradual exploration of the search space.

The general form of the mutation operator is

$$\mathbf{x}_n = \lambda \mathbf{m}_{best} + (1-\lambda)\,\mathbf{m}_{n_1} + \sum_{l=1}^{L} F_l \cdot \left(\mathbf{m}_{n_{l,2}} - \mathbf{m}_{n_{l,3}}\right) \tag{86}$$

where $\mathbf{m}_{best}$ is the best member of the current population, $\lambda \in [0,1)$ is a coefficient which controls the influence of the best member, L is the number of differences, $F_l > 0$ is for each $l \in \{1,\dots,L\}$ a scale factor. The indices n_1, $n_{l,2}$ and $n_{l,3}$ are distinct random values uniformly selected from $\{1,\dots,N\}$. The most frequently used cases are when $L = 1$ and $\lambda \in \{0, 1\}$. Thus for $\lambda = 1$ one obtains the *DE/best/1/** variant

$$\mathbf{x}_n = \mathbf{m}_{best} + F \cdot (\mathbf{m}_{n_2} - \mathbf{m}_{n_3}) \tag{87}$$

and for $\lambda = 0$ one obtains the *DE/rand/1/** variant

$$\mathbf{x}_n = \mathbf{m}_{n_1} + F \cdot (\mathbf{m}_{n_2} - \mathbf{m}_{n_3}) \,. \tag{88}$$

Recombination

In evolutionary algorithms the recombination operator usually combines features from different parents. In the case of differential evolution, the mutation operator is already based on a recombination of individuals. Recombination in differential evolution functions somewhat differently by combining a member of the current population (e.g., target vector) with a vector generated by mutation (e.g., mutant vector) to form a candidate for propagation into the next generation (e.g., trial vector). This can be implemented by mixing the components (as in exponential and binomial recombination) or by an arithmetical recombination between the target and the mutant vectors (as in the *DE/current-to-rand* variants).

In exponential recombination the trial vector is constructed by taking consecutive components from the mutant vector

$$y_{n,d} = \begin{cases} x_{n,d} & \text{for } d \in \{d_r, d_{r+1}, d_{r+2}, \ldots, d_K\} \\ m_{n_4,d} & \text{otherwise} \end{cases} \tag{89}$$

where d_r is a randomly selected index. Subsequent indices $d_{r+1}, \ldots, d_K$ are those for which $randUniform[0, 1) < CR$. The first index for which $randUniform[0, 1) \geq CR$ is d_{K+1}. The probability that the number of parameters s copied from the mutant vector $\mathbf{x}_n$ to the trial vector $\mathbf{y}_n$ is not greater than q is given by

$$P\,(s \leq q) = 1 - CR^q. \tag{90}$$

In the case of binomial recombination individual components of the trial vector

$\mathbf{y}_n$ are obtained as

$$y_{n,d} = \begin{cases} x_{n,d} & \text{if } randUniform\,[0,1) < CR \text{ or } d = d_r \\ m_{n_4,d} & \text{otherwise} \end{cases} \tag{91}$$

where d_r is a randomly selected value from $\{1, \ldots, D\}$ to ensure that the trial vector $\mathbf{y}_n$ is not identical to its corresponding target vector $\mathbf{m}_{n_4}$. The crossover rate $CR \in [0,1)$ controls the number of components taken from the mutant vector, $\mathbf{x}_n$. The number of components taken from the mutant vector follows the binomial distribution $P_b = CR\,(1 - 1/D) + 1/D$ where D is the dimensionality of the problem. The value P_b provides the probability that any given component will be copied from the mutant vector $\mathbf{x}_n$ into the trial vector $\mathbf{y}_n$.

Classic Differential Evolution

The most popular algorithm variant performs mutation using members selected from the population at random, with only one pair used to form the differential mutation. In addition, classic differential evolution implements a binomial process of recombination. Pseudo-code outlining the procedure for the classic differential evolution algorithm *DE/rand/1/bin* is presented as Algorithm 1. [13]

5.5.2 Performance Comparisons

Several studies have been completed in order to characterize the performance of the differential evolution variants with respect to a broad range of problems. One study considered 14 different variants of the differential evolution algorithm [14] toward the solution of 14 high dimensional ($D = 30$) benchmark problems categorized by their modality and separability. The unimodal class of problems is characterized by a single minimum, whereas the multimodal problems include multiple, relative minima in addition to a single global minimum. The separability of a problem relates to the degree of coupling among the model parameters with separable problems having uncoupled parameters and non-separable problems hav-

Algorithm 1 Classic Differential Evolution – *DE/rand/1/bin*

```
begin
  $g = 0$
  Create a random initial population $\mathbf{m}_{g,n} \forall, n = 1, \ldots, N_{pop}$      Initialization
  Evaluate $\phi\left(\mathbf{m}_{g,n}\right) \forall, n = 1, \ldots, N_{pop}$      Objective
  for $g = 1$ to $G$ do
      for $n = 1$ to $N_{pop}$ do
          Select four members such that $n_1 \neq n_2 \neq n_3 \neq n_4$
          $n_{1,2,3,4} = randInteger\left(1, N_{pop}\right)$
          $\mathbf{x}_n = \mathbf{m}_{g,n_1} + F \cdot \left(\mathbf{m}_{g,n_2} - \mathbf{m}_{g,n_3}\right)$      Mutation
          Select one trait to be copied from mutant vector
          $d_r = randInteger\left(1, D\right)$
          for $d = 1$ to $D$ do
              if $randUniform\left[0, 1\right) < CR$ or $d = d_r$      Cross-over
                  then $y_{n,d} = x_{n,d}$
                  else $y_{n,d} = m_{g,n_4,d}$
              fi;
          od;
          if $\phi\left(\mathbf{y}_n\right) \leq \phi\left(\mathbf{m}_{g,n}\right)$      Objective
              then $\mathbf{m}_{g+1,n} = \mathbf{y}_n$      Selection
              else $\mathbf{m}_{g+1,n} = \mathbf{m}_{g,n}$
          fi;
      od;
      $g = g + 1$
  od;
end
```

ing various degrees of coupling among the model parameters comprising the search space. Each variant was assessed according to both its probability of convergence and convergence rate. It was found that the *DE/rand/1/bin* was among the most competitive for the broadest selection of test cases.

A similar study, composed of 8 differential evolution variants and 13 benchmark problems [15], concluded that the *DE/best/1/bin* was the most competitive option, but required careful selection of the cross-over rate CR for different problem classes. In addition, use of the "*best*" selection option brings with it the risk of premature convergence, particularly for multimodal problems.

In a more focused study, limited to comparison of the "*rand*" and "*best*" crossover strategies [16], it was found that while either method could produce good results, use of the "*best*" option benefited from careful selection, or tuning, of the crossover rate CR and scale factor F. Low performing selections for these parameters were prone to premature convergence due to less vigorous exploration of the search space.

More recent work has explored the potential for self-adaptive algorithms to improve the probability and rate of convergence with mixed results [17], [18], [19]. While certain of these approaches have demonstrated improved performance in selected benchmark cases, none have yet demonstrated the kind of robust, reliable performance on the wide variety of problems as has been demonstrated by the classic *DE/rand/1/bin* algorithm.

List of References

[1] W. Menke, *Geophysical Data Analysis: Discrete Inverse Theory*, ser. International Geophysics Series, R. Dmowska and J. R. Holton, Eds. San Diego: Academic Press, 1989, vol. 45.

[2] D. M. F. Chapman, "What are we inverting for?" in *Inverse Problems in Underwater Acoustics*, M. I. Taroudakis and G. N. Makrakis, Eds. New York, NY: Springer-Verlag, 2001.

[3] C. F. Mecklenbräuker and P. Gerstoft, "Objective functions for ocean acoustic inversion derived by likelihood methods," *Journal of Computational Acoustics*, vol. 8, no. 2, pp. 259–270, June 2000.

[4] P. Gerstoft, "Inversion of seismoacoustic data using genetic algorithms and *a posteriori* probability distributions," *Journal of the Acoustical Society of America*, vol. 95, no. 2, pp. 770–782, Feb. 1994.

[5] P. Gerstoft and C. F. Mecklenbräuker, "Ocean acoustic inversion with estimation of *a posteriori* probability distributions," *Journal of the Acoustical Society of America*, vol. 104, no. 2, pp. 808–819, Aug. 1998.

[6] J. C. Osler, D. M. F. Chapman, P. C. Hines, G. P. Dooley, and A. P. Lyons, "Measurement and modeling of seabed particle motion using buried vector

sensors," *IEEE Journal of Oceanic Engineering*, vol. 35, no. 3, pp. 516–537, July 2010.

[7] P. C. Hines, J. C. Osler, J. G. E. Scrutton, D. M. F. Chapman, and A. Lyons, "Using buried vector sensors to examine seabed layering in sandy sediment," *Journal of the Acoustical Society of America*, vol. 120, no. 5, p. 3181, Nov. 2006.

[8] H. Schmidt, *OASES Version 3.1 User Guide and Reference Manual*, Massachuesetts Institute of Technology, July 2006. [Online]. Available: http://acoustics.mit.edu/faculty/henrik/oases.html

[9] G. R. Potty, J. H. Miller, J. F. Lynch, and K. B. Smith, "Tomographic inversion for sediment parameters in shallow water," *Journal of the Acoustical Society of America*, vol. 108, no. 3, pp. 973–986, Sept. 2000.

[10] G. R. Potty and J. H. Miller, "Nonlinear optimization techniques for geoacoustic tomography," in *Inverse Problems in Underwater Acoustics*, M. I. Taroudakis and G. N. Makrakis, Eds. New York, NY: Springer-Verlag, 2001.

[11] D. G. Simons, C. V. Moll, and C. H. Harrison, "Inversion of shallow water ambient noise data by means of differential evolution as a global search method," in *Acoustic Sensing Techniques for the Shallow Water Environment*, A. Caiti, N. R. Chapman, J.-P. Hermand, and S. M. Jesus, Eds. Dordrecht, The Netherlands: Springer-Verlag, 2006.

[12] R. M. Storn and K. V. Price, "Differential evolution – a simple and efficient heuristic for global optimization over continuous spaces," *Journal of Global Optimization*, vol. 11, no. 4, pp. 341–359, Dec. 1997.

[13] K. V. Price, , R. M. Storn, and J. A. Lampinen, *Differential Evolution A Practical Approach to Global Optimization*, ser. Natural Computing Series. Heidelberg Germany: Springer-Verlag, 2005.

[14] G. Jeyakumar and C. S. Velayuthan, "An empirical comparison of differential evolution variants on different classes of unconstrainted global optimization problems," in *World Congress on Nature and Biologically Inspired Computing*, 2009, pp. 866–871.

[15] E. Mezura-Montes, J. Velázquez-Reyes, and C. A. Coello, "A comparative study of differential evolution variants for global optimization," in *Proceedings of the 8th Annual Conference of Genetic and Evolutionary Computation*, 2006, pp. 485–492.

[16] D. Zaharie, "A comparative analysis of crossover variants in differential evolution," in *Proceedings of the International Multiconference on Computer Science and Information Technology*, 2007, pp. 171–181.

[17] D. Zaharie, “Adaptive differential evolution and exponential crossover,” in *Proceedings of the International Multiconference on Computer Science and Information Technology*, 2008, pp. 927–931.

[18] K. Zielinski, X. Wang, and R. Laur, “Comparison of adaptive approaches for differential evolution,” in *Parallel Problem Solving from Nature*, ser. Lecture Notes in Computer Science, G. Rudolph, T. Jansen, S. Lucas, C. Poloni, and N. Beume, Eds., vol. 5199. Heidelberg Germany: Springer-Verlag, 2008, pp. 641–650.

[19] G. Jeyakumar and C. S. Velayuthan, “A comparative performance analysis of differential evolution and dynamic differential evolution variants,” in *World Congress on Nature and Biologically Inspired Computing*, 2008, pp. 463–468.

CHAPTER 6

Inversion of Complex Acoustic Transfer Functions

6.1 Inversion Data

Acoustic transfer functions were a natural choice to support the inversion process since they carry information about the physical properties of the paths over which the wave has traversed, and they are readily computed. A set of overlapping paths that spanned the space sampled by the acoustic vector sensors was chosen as the basis for the inversion process. Figure 25 illustrates the acoustic paths for which transfer functions were computed. The location of each vector sensor is indicated, as is the path over which each transfer function was computed. Transfer function subscripts identify the end points of each acoustic path.

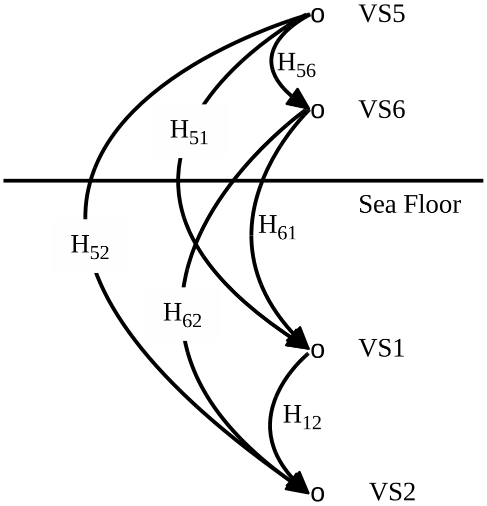

Figure 25. Acoustic transfer function paths. Relative locations for acoustic vector sensors VS5, VS6, VS1, VS2 are annotated. The end points for each acoustic path is indicated by a curved line. For example, H_{52} is the acoustic path extending from VS5 to VS2.

Recall that the complex acoustic transfer functions used to support the inversions were provided as Eq. 81 and Eq. 83, and restated below as

$$H_a^{(p)}\left(\omega,\vec{r}_m,\vec{r}_n\right)=\frac{P\left(\omega,\vec{r}_n\right)}{P\left(\omega,\vec{r}_m\right)}=\frac{H_a^{(p)}\left(\omega,\vec{r}_1,\vec{r}_n\right)}{H_a^{(p)}\left(\omega,\vec{r}_1,\vec{r}_m\right)},\tag{92}$$

$$\widehat{H}_a^{(u)}\left(\omega,\vec{r}_m,\vec{r}_n\right)=\frac{U_s\left(\omega,\vec{r}_n,\rho_n,c_{s_n}\right)}{U_s\left(\omega,\vec{r}_m,\rho_m,c_{s_m}\right)}=\frac{H_a^{(u)}\left(\omega,\vec{r}_1,\vec{r}_n\right)H_s\left(\omega,n\right)}{H_a^{(u)}\left(\omega,\vec{r}_1,\vec{r}_m\right)H_s\left(\omega,m\right)},\tag{93}$$

where $H_s\left(\omega,n\right)=H_s^{(\varepsilon)}\left(\omega,\rho_n,c_{s_n}\right)$ when sensor n was beneath the seafloor and $H_s\left(\omega,n\right)=H_s^{(f)}\equiv 1$ when sensor n was suspended above the seafloor.

Figure 26 illustrates the scalar and vector field transfer functions measured for the six receiver pair paths. The annotations indicate both the acoustic path and the type of transfer function that is depicted. For example, $H_{52}^{(p)}$ depicts the transfer function for acoustic pressure between vector sensors 5 and 2, while $H_{52}^{(u)}$ depicts the transfer function for the acoustic particle velocity over the same path. Inspection of the transfer function data shows that the scatter among the individual paths was greatest for the pressure transfer functions that crossed the seafloor interface (e.g. $H_{51}^{(p)}$, $H_{52}^{(p)}$, $H_{61}^{(p)}$ and $H_{62}^{(p)}$). Scatter among the pressure transfer function observations was notably less for acoustic paths that did not traverse this interface (e.g. $H_{56}^{(p)}$ and $H_{12}^{(p)}$). Also evident in the figure is that the scatter among the velocity transfer functions was low for all acoustic paths.

The acoustic transfer functions among six overlapping paths were computed for all transmit frequencies. In addition, the standard deviations were computed for use in the weight vector Eq. 70 included as part of the objective function Eq. 69. These data were used as the basis of the inversion process. Transfer functions among the six acoustic paths illustrated in Fig. 25 are provided as Fig. 27–29.

In the simplest case of a plane propagating wave, the transfer functions for the scalar and vector acoustic fields are identical, where the acoustic pressure and particle velocity are everywhere related by the characteristic impedance $\rho_\circ c$ of the

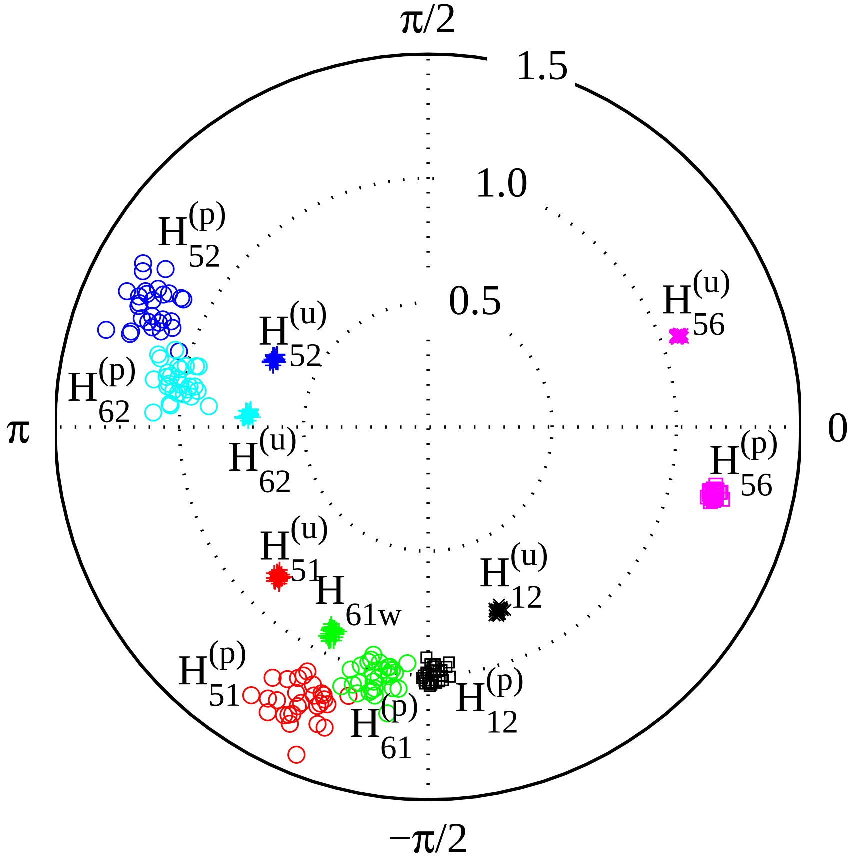

Figure 26. Complex acoustic transfer functions. The transmit frequency was 800 Hz. The annotations indicate both the acoustic path and the type of transfer function that is depicted. For example, $H_{52}^{(p)}$ depicts the transfer function for acoustic pressure between VS5 and VS2, while $H_{52}^{(u)}$ depicts the transfer function for the acoustic particle velocity over the same path.

medium. While the circumstances for a spherically divergent wave are slightly more complicated, they are important only for source-to-receiver ranges on the order of a wavelength or less. Thus, for the purposes of this discussion, we consider the incident wave field to be approximately planar. Features of the environment, reflecting boundaries in particular, change the nature of the field from a purely propagating wave, to one with standing wave characteristics. Thus information about the nature of reflecting surfaces becomes embedded in the acoustic transfer functions with the result that the scalar and vector acoustic transfer functions are no longer identical.

Consider also the effect of sediment shear elasticity in the case of a buried vector sensor where motion of the sensor case may not equal that of the surrounding sediment. In this case, a frequency dependent suspension response that is sensitive to both the sediment shear wave speed and the density contrast between the sensor and sediment was shown to exist. The effect of this response will also be reflected in the vector acoustic transfer function such that information about the sediment can be exploited by an inversion process.

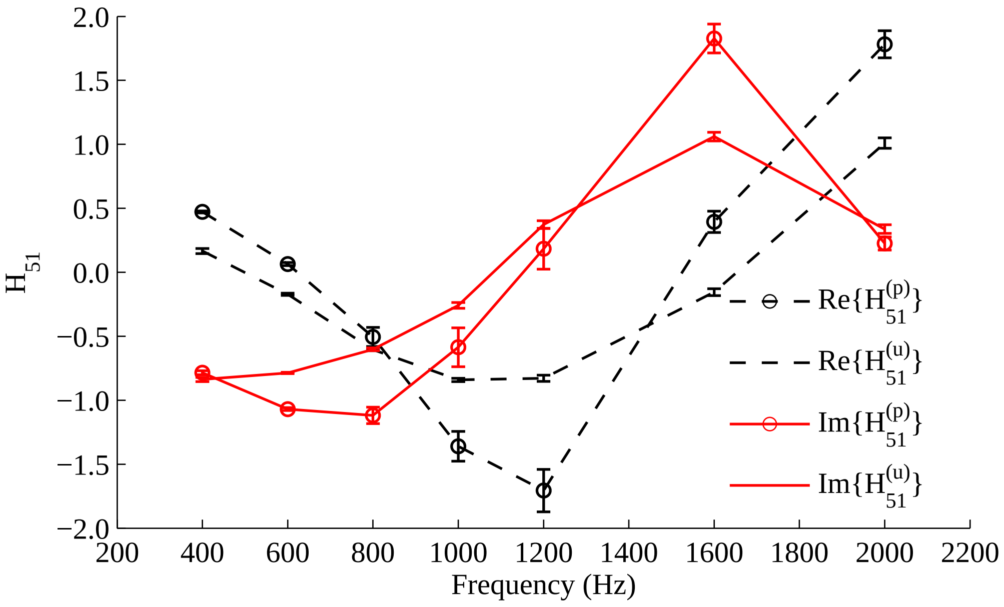

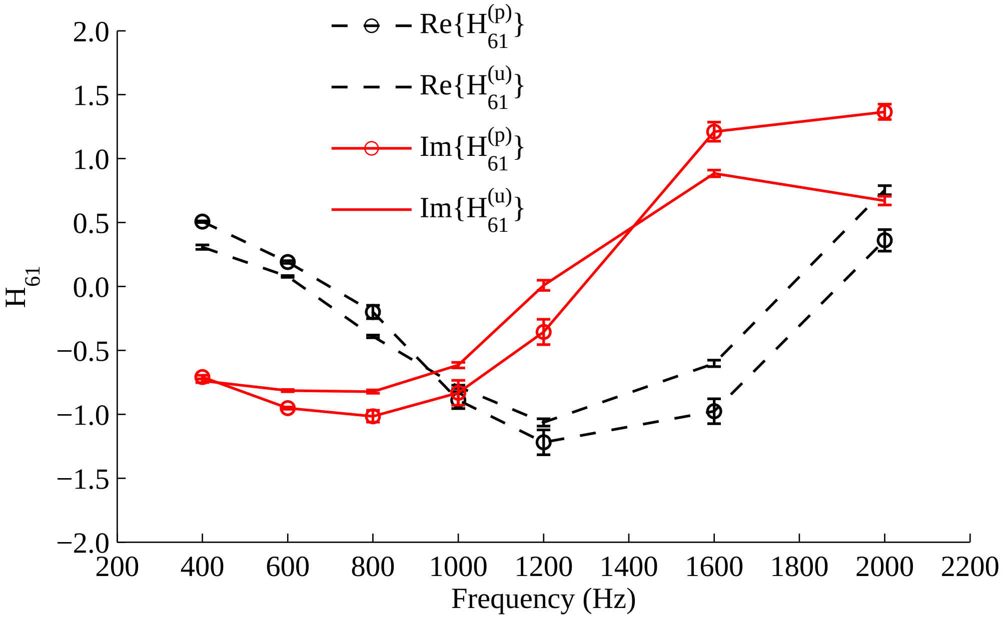

Figure 27. Complex acoustic transfer functions $H_{51}^{(p)}$, $H_{51}^{(u)}$, $H_{61}^{(p)}$ and $H_{61}^{(u)}$. Error bars represent one standard deviation.

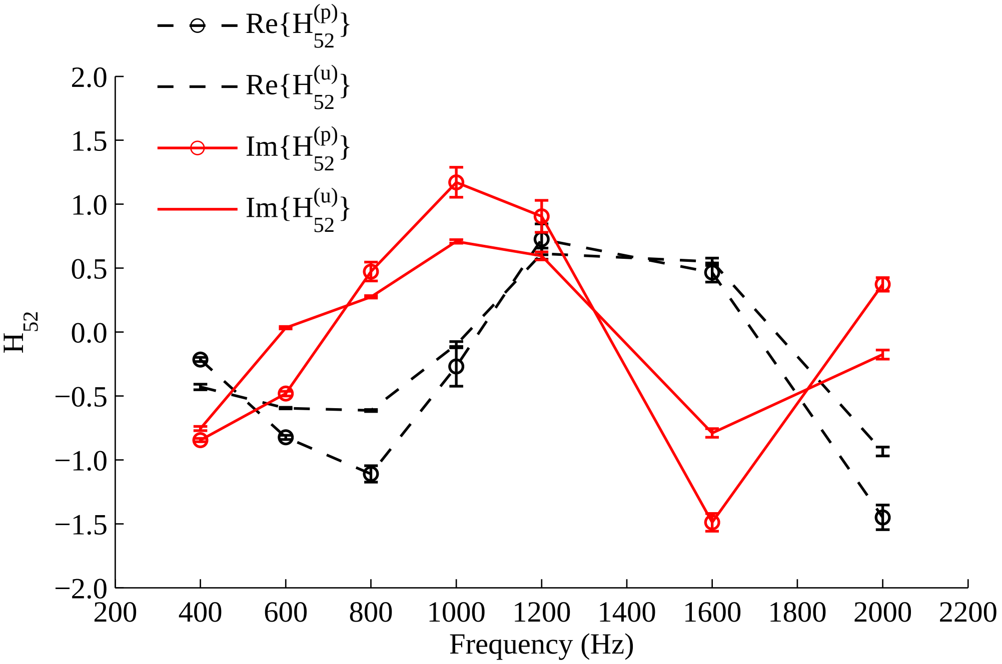

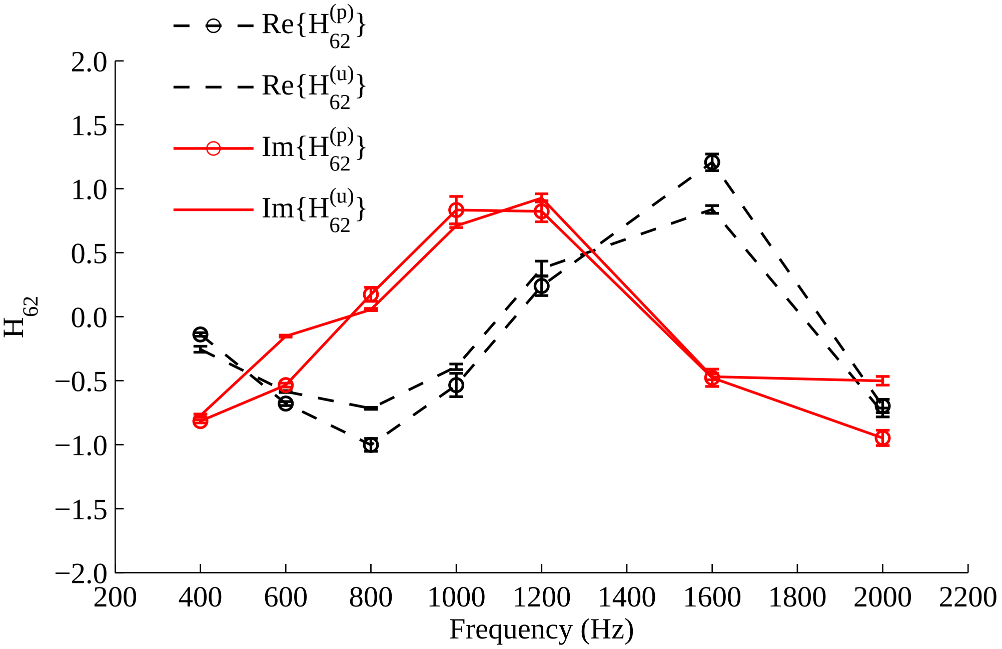

Figure 28. Complex acoustic transfer functions $H_{52}^{(p)}$, $H_{52}^{(u)}$, $H_{62}^{(p)}$ and $H_{62}^{(u)}$. Error bars represent one standard deviation.

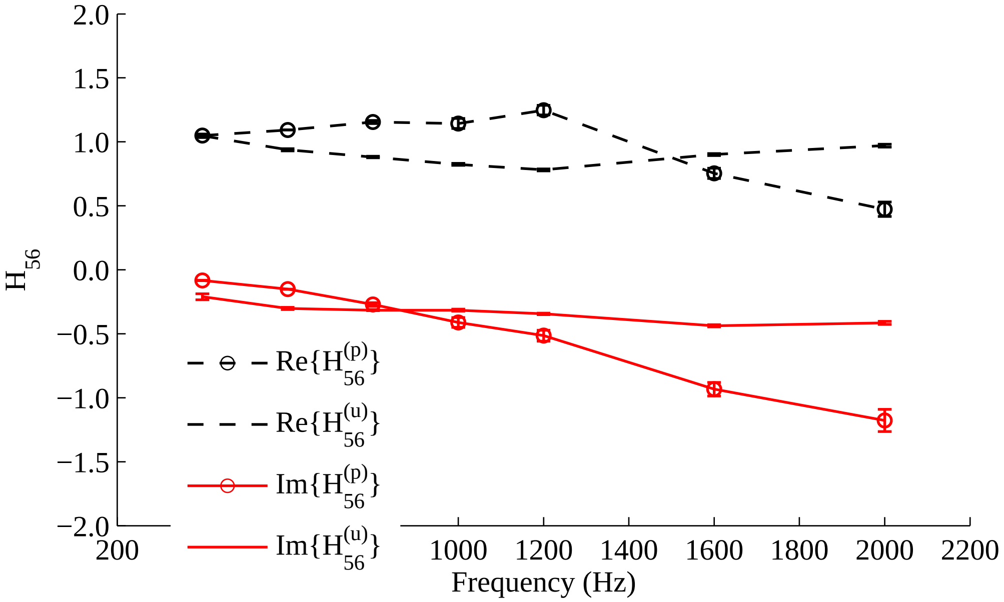

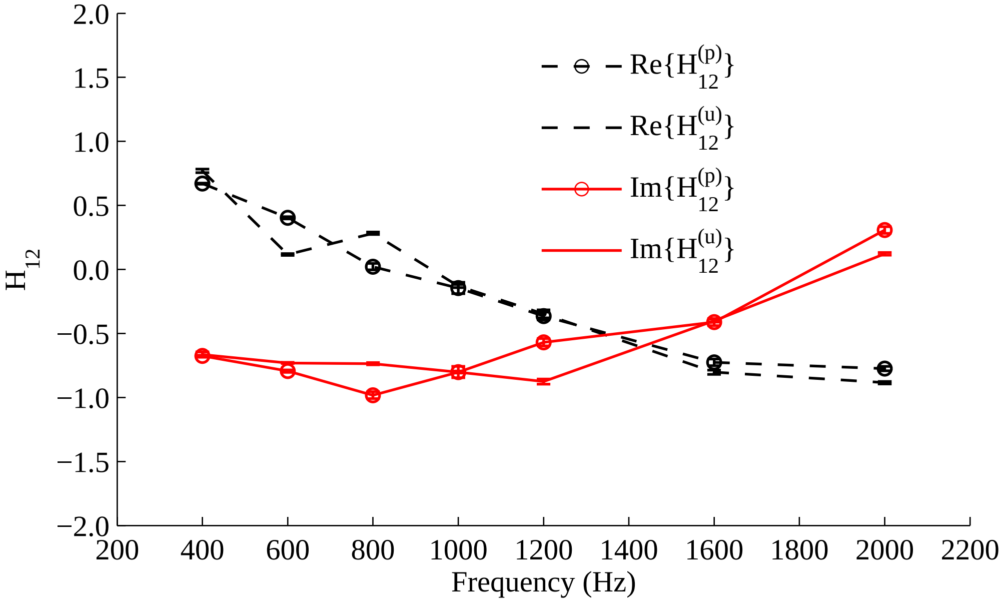

Figure 29. Complex acoustic transfer functions $H_{56}^{(p)}$, $H_{56}^{(u)}$, $H_{12}^{(p)}$ and $H_{12}^{(u)}$. Error bars represent one standard deviation.

Table 3. Environmental parameterization for synthetic data. The environment was parameterized as reported for the test site [1] and was used in the sensitivity analysis and inversion study. The reported thin, muddy layer (e.g., sediment layer two) was placed such that it contained the lower of the two buried vector sensors (e.g., VS2). The shear speed for this layer was not reported for the site, but was selected to test resolution of the inversion for this parameter.

Layer	**Parameter**	**Value**	
Water Column	Depth	16.7	m
	Sound Speed	1531	m/s
Sediment Layer One	Thickness	90	cm
	Sediment Density	2.04	g/cm^3
	Compression Wave Speed	1680	m/s
	Shear Wave Speed	120	m/s
Sediment Layer Two	Thickness	20	cm
	Sediment Density	1.68	g/cm^3
	Compression Wave Speed	1583	m/s
	Shear Wave Speed	100	m/s
Sediment Half Space	Sediment Density	2.04	g/cm^3
	Compression Wave Speed	1680	m/s
	Shear Wave Speed	120	m/s

6.2 Objective Function Sensitivity Analysis

The sensitivity of the objective function Eq. 69 to the estimated geoacoustic parameters was evaluated using a set of synthetic observations computed for parameter values reported for the SAX04 experiment site [1]. The marginal sensitivity of each parameter was then assessed by calculating the value of the objective function across the allowed range for each parameter while holding all other parameters constant at their reported value. The bottom parameterization included the reported low impedance reflector as summarized in Table 3. The reflector was reported to have been a thin muddy layer 5 to 20 cm thick and located within the top meter of sediment. The reported density and compression wave speed were 1.68 g/cm^3 and 1583 m/s, respectively. No estimate of the shear wave speed in this layer was reported. For the purposes of the sensitivity study, this layer was modeled as extending from 90 to 110 cm beneath the seafloor and with the reported density and compression wave speeds. A shear wave speed of 100 m/s was assumed, a value that was 20 m/s less than that in the bounding sediment layers. Given these modeling parameters, the deeper of the buried vector sensors would have been within this thin, muddy layer.

The analysis was performed for five distinct cases. In the first, it was assumed that only the scalar field was measured using typical hydrophones. In the second case, it was assumed that only the vector field was measured by an ideal (e.g., distortion free) sensor. The third case included both scalar and vector field data, again assuming noise and distortion free measurements. In the fourth case, it was assumed that only the vector field was measured, and that the measurements were distorted by the suspension response of a sensor with the same mass properties as the TV-001 acoustic vector sensor (e.g., neutrally buoyant in seawater). The fifth case included both the scalar and vector fields as observed by a sensor with the mass properties of the TV-001 acoustic vector sensor.

One of the goals during development of the inversion method was to minimize the influence of the water column properties on the objective function. It was this goal that influenced the decision to use a set of transfer functions that were local to the seabed and confined to the space sampled by the acoustic vector sensors. Figure 30 illustrates the sensitivity of the objective function to the water depth and sound speed in the water column. As shown in the figure, the objective function had modest sensitivity to both of these parameters. The analysis also predicted that the objective function was more sensitive to the scalar field than it was to the acoustic vector field, and that the mass properties of the buried vector sensors had negligible effect on the objective function. Finally, the multi-modal nature of the problem is illustrated by several relative minima for both the water depth and the sound speed.

Figure 31 illustrates the behavior of the objective function for variations in the estimated parameters of the first layer, beginning at the seafloor. As shown in the top panel, sensitivity of the objective function to variations in the thickness of this layer was of the same order as for the other geoacoustic parameters. As was the case for the estimation of water depth, the marginal sensitivity for thickness of the first sediment layer includes a number of relative minima that would likely prove problematic for gradient descent approaches to estimation of this parameter.

Figure 32 illustrates the sensitivity of the objective function to geoacoustic parameters of a thin, muddy layer at a nominal depth of one meter. Sensitivity of the objective function to the thickness of this layer was similar to that for the first layer, but with less pronounced relative minima. Sensitivity of the objective function to the other geoacoustic parameters was generally consistent with the first layer, but without the pronounced relative maxima for the compressional wave speed at about 2200 m/s shown in Fig. 31.

Figure 33 illustrates the sensitivity of the objective function to the geoacoustic properties of a hypothetical layer that was physically remote relative to the positions of the buried sensors. The hypothetical layer was inserted at a depth of 2.1 meters. The sensitivity of the objective function to variations in density was virtually independent of the acoustic field data used to calculate the objective function. Sensitivity to variation in compression wave speed in this remote layer is provided in the center panel where it is shown that scalar field data provides slightly greater sensitivity than was predicted for the vector field data. Finally, the objective function responded to the shear wave speed in this layer, however the variation of about 0.008 across all plausible values was too little to be of practical value. Thus, the objective function did not resolve shear wave speed in this layer.

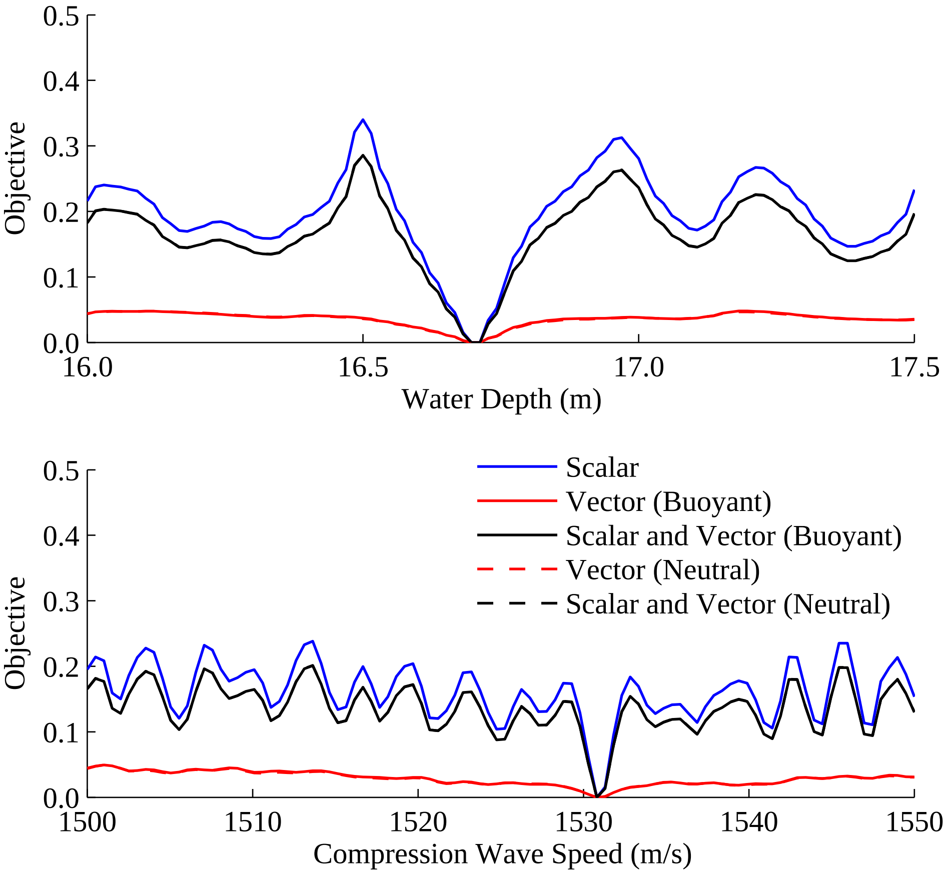

Figure 30. Objective function sensitivity ϕ_H: water column. Figure depicts the sensitivity of the objective function based on complex acoustic transfer functions to variations in properties of the water column.

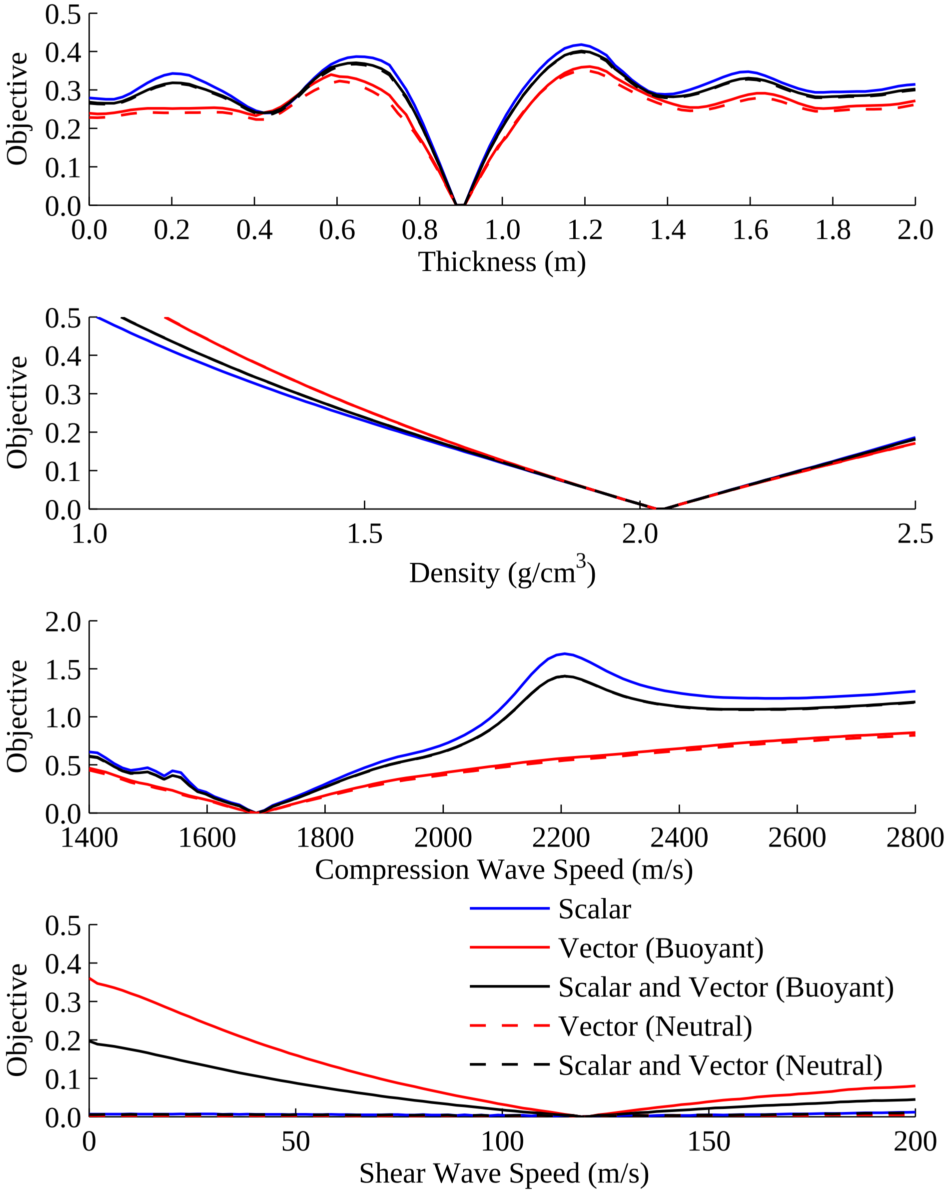

Figure 31. Objective function sensitivity ϕ_H: layer one. Figure depicts the sensitivity of the objective function based on complex acoustic transfer functions to variations in properties of the first layer.

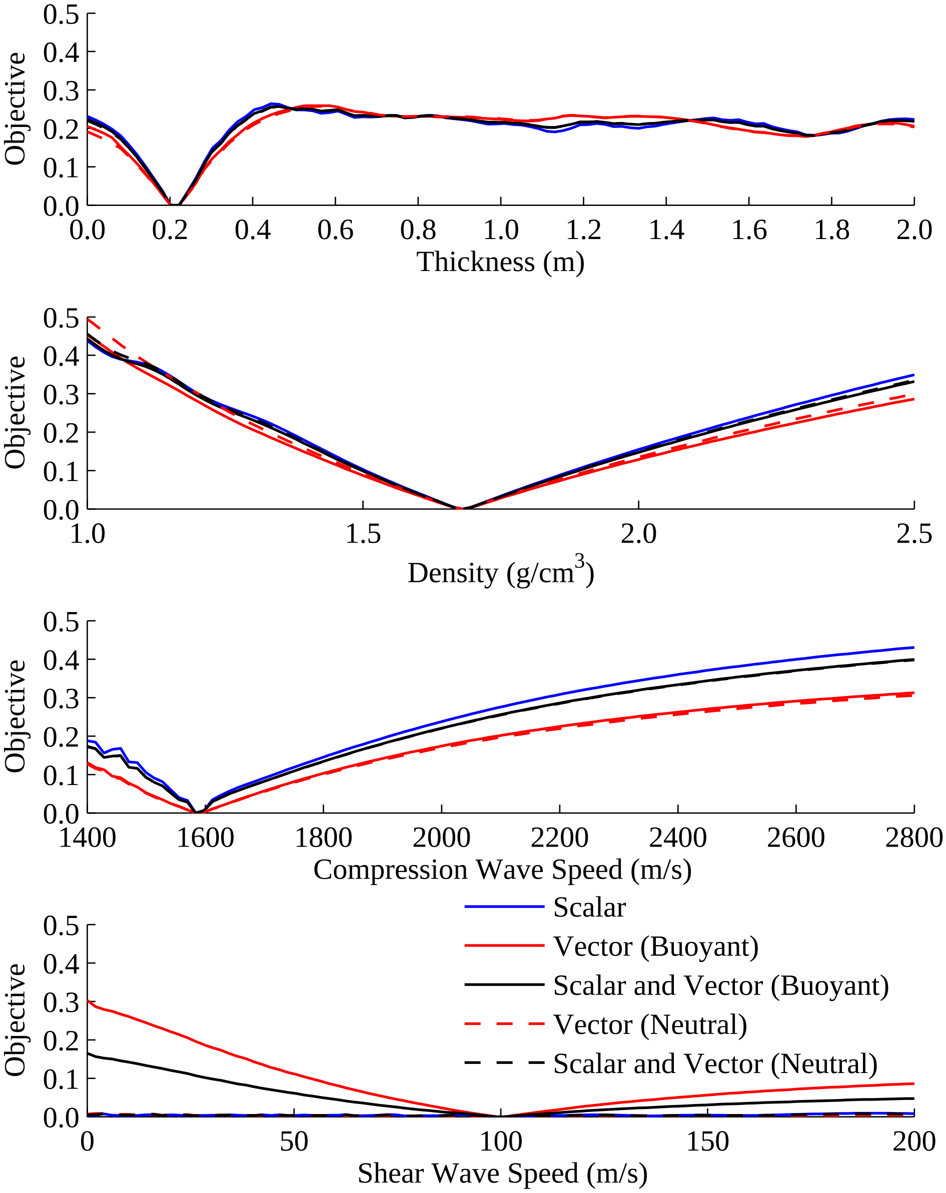

Figure 32. Objective function sensitivity ϕ_H: layer two. Figure depicts the sensitivity of the objective function based on complex acoustic transfer functions to variations in properties of the second, thin elastic layer.

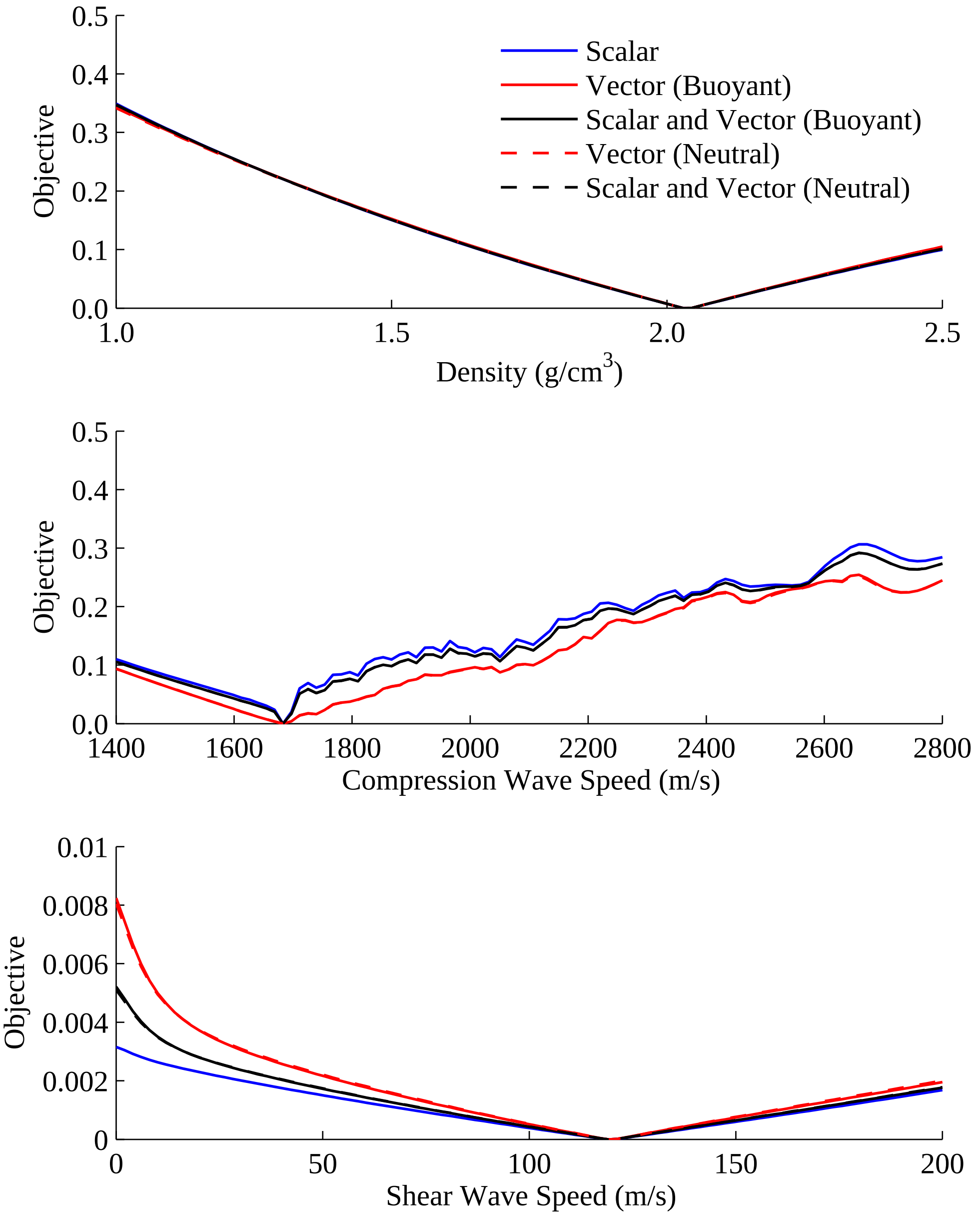

Figure 33. Objective function sensitivity ϕ_H: half space. Figure depicts the sensitivity of the objective function based on complex acoustic transfer functions to variations in properties of the half space lying beneath a thin, low impedance reflector.

A two dimensional sensitivity analysis was performed to test the objective function for correlation between certain geoacoustic parameters. For example, the sensitivity of the objective function to both the compression wave speed and density was performed to test for correlation between these two parameters. This pairing was selected to determine if these two parameters could be resolved independently, or if only their product could be resolved as would be the case if the objective function was sensitive to only the characteristic impedance of the medium.

Figure 34 illustrates the behavior of the objective function when operating on scalar field data alone. The values assumed for the compression wave speed and density in the first sediment layer are indicated by the square marker. The range of values for which their product, or characteristic impedance, was held constant are indicated by the solid red line, with ±10% indicated by dashed red lines. The result indicates that inversion of scalar field data alone should be able to independently resolve these two parameters. Figure 35 illustrates a similar result when analyzing the sensitivity of the objective function to changes in these parameters at a depth of 2.1 m. In this case, the objective function was much less sensitive and was least sensitive in the direction of constant characteristic impedance for this remote layer. Since this layer would only influence the objective function through reflection, it was not unexpected that the sensitivity varied most strongly with the characteristic impedance mismatch at this interface.

Figure 36 provides equivalent results for estimation of geoacoustic properties of the first sediment layer when only the vector field data was included in the objective function. While the sensitivity of the objective function to properties in this layer was reduced relative to that for the scalar objective function, the compression wave speed and density were independently resolved. On the contrary, at depth of 2.1 m the objective function provided good sensitivity to changes in the characteristic impedance only. As illustrated in Fig. 37, the contours of constant objective function value were nearly parallel to the line of constant characteristic impedance when only the vector field data was used. Figures 38 and 39 illustrate the objective function sensitivity when both the scalar and vector field data were included in the objective function. In this case, the behavior of the objective function was largely controlled by the scalar field data.

6.2.1 Uncertainty in Buried Sensor Depths

Additional analysis was performed to explore the impact of uncertainty in the depths of the buried sensors. Figure 40 shows the result of a two dimensional sensitivity study performed over a range of sensor depth errors spanning 20 cm. The objective function was computed using both the scalar and vector field transfer functions. Sensor burial depths used in the generation of the synthetic data were 61 and 98 cm. Objective function values were computed where the sensor positions were incorrectly estimated over the ranges illustrated in the figure. The analysis showed that sensitivity of the objective function to sensor location errors on the order of 5 cm could increase the value of the objective function to approximately 0.2 (with all other parameters held constant at their true values). Objective function values of this magnitude are of the same order as computed for plausible variations in the geoacoustic parameters of interest. Thus, the performance of inversions based on complex acoustic transfer functions could be significantly degraded by uncertainties in the sensor burial depths on the order of 5 cm.

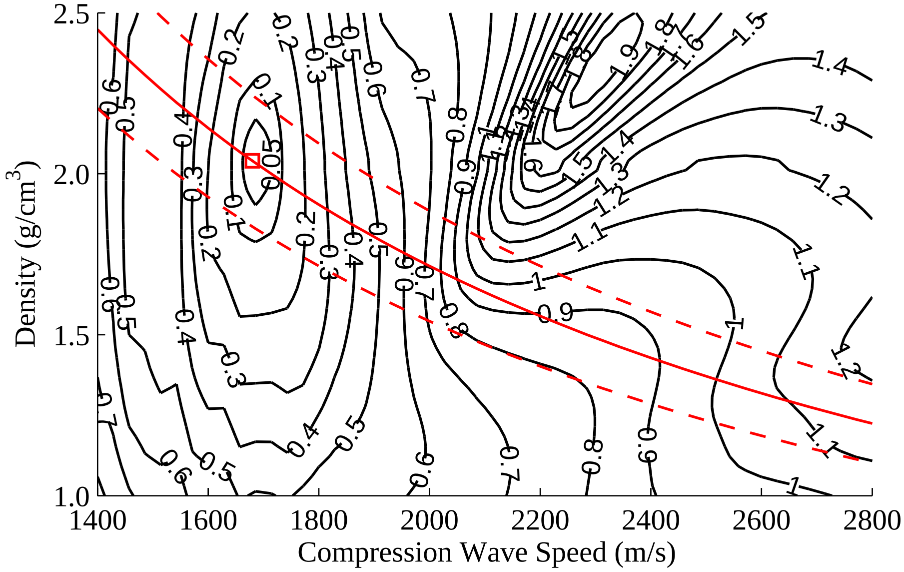

Figure 34. Objective function sensitivity ϕ_H (scalar): layer one

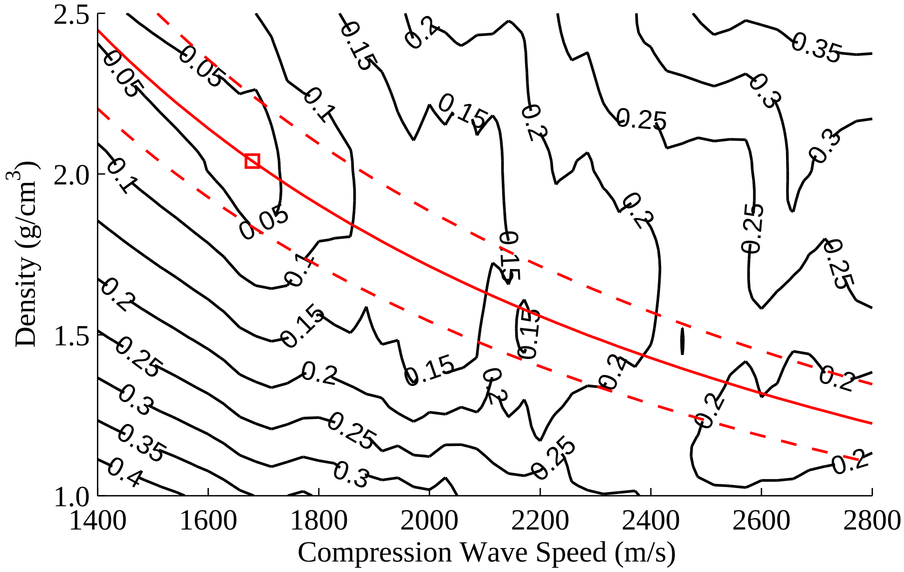

Figure 35. Objective function sensitivity ϕ_H (scalar): half space

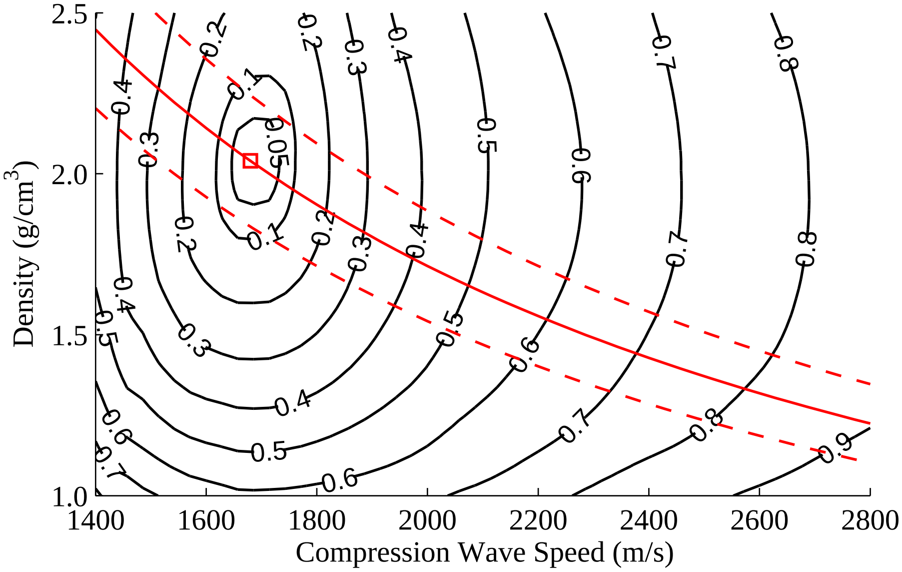

Figure 36. Objective function sensitivity ϕ_H (vector): layer one

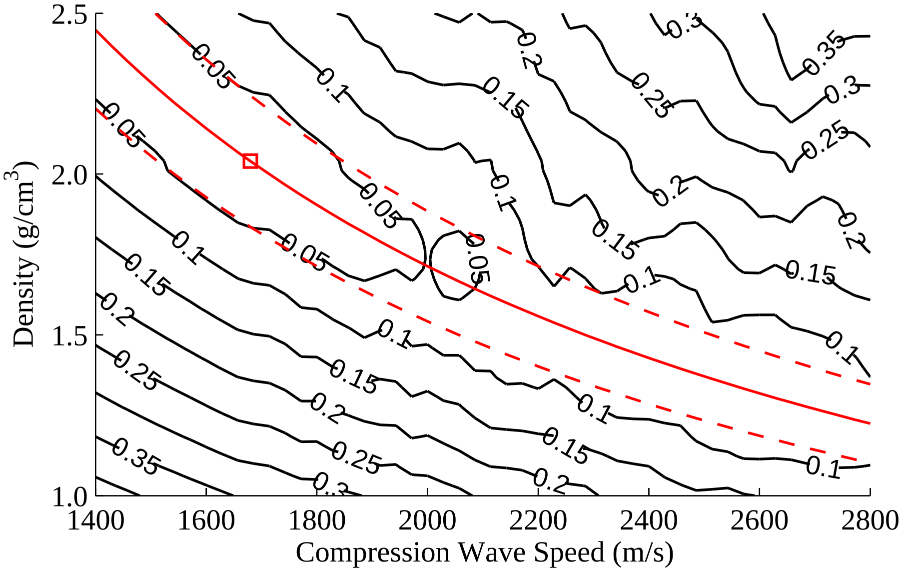

Figure 37. Objective function sensitivity ϕ_H (vector): half space

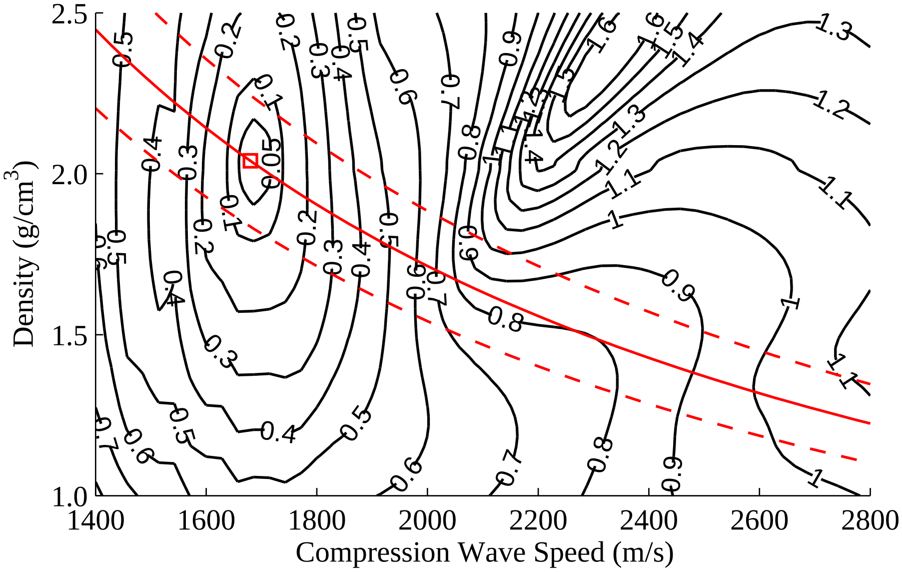

Figure 38. Objective function sensitivity ϕ_H (scalar–vector): layer one

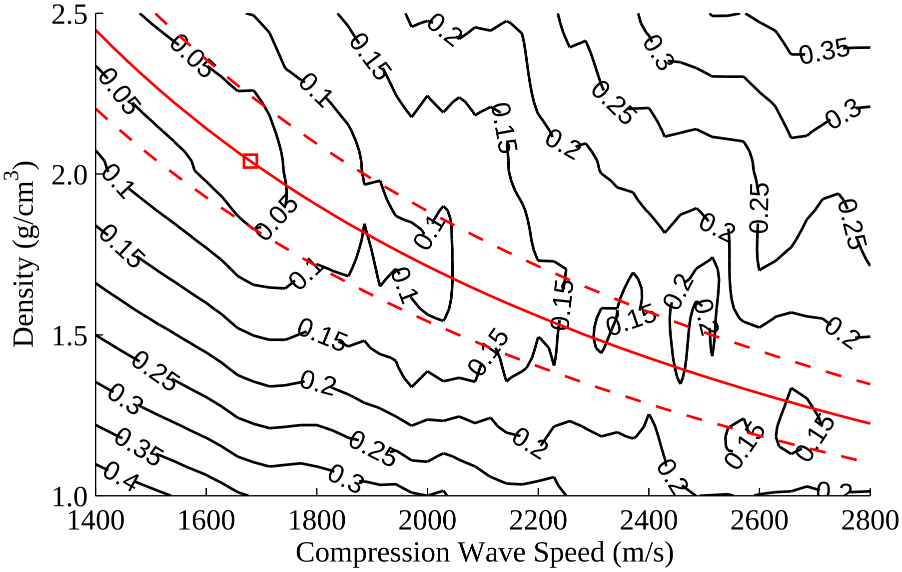

Figure 39. Objective function sensitivity ϕ_H (scalar–vector): half space

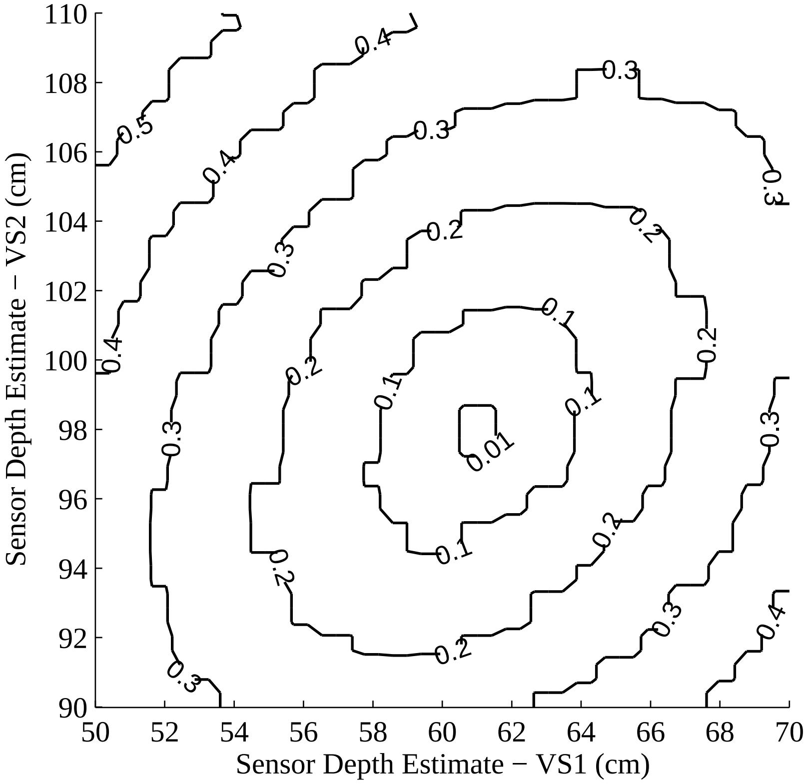

Figure 40. Objective function sensitivity ϕ_H (scalar–vector): sensor depth. The synthetic data set was generated with VS1 and VS2 vector sensors located 61 and 98 cm beneath the sea floor, respectively. Objective function values were computed with various sensor burial depths included in the forward model. The sharp edges and corners of the contours resulted from 1 cm resolution for receiver locations implemented in the forward model.

6.3 Inversion of Synthetic Data

Behavior of the inversion method was validated by inverting the same synthetic data set as was used for the sensitivity study. The primary objective for inversion of a synthetic data set was to verify the performance of the differential evolution algorithm when operating on acoustic data for which the associated geoacoustic parameters were exactly known. Since it was known that a solution existed for which the objective function was exactly zero, failure to converge under these conditions would indicate that the proposed inverse methods were fundamentally flawed. A second objective for the synthetic inversion was to assess the variances of the parameter estimates under ideal conditions. Thus, the synthetic inversions provided insight into the performance of the inversion method when operating under the best case scenario.

A total of six inversions were performed using synthetic acoustic transfer functions. Scalar acoustic, vector acoustic and combined scalar-vector acoustic transfer functions were inverted. In addition, inversions with and without buried sensor depth errors were performed. In all cases, synthetic data were generated using buried sensor depths of 61 and 98 cm. Cases annotated as Inversion 1 were performed using the correct buried sensor depths in the forward model during the inversion. Cases annotated as Inversion 2 were performed using the planned sensor depths of 50 and 100 cm in the forward model during the inversion. Thus, Inversion 2 simulated the case where significant sensor burial depth errors existed.

Figure 41 illustrates the convergence performance for all of the synthetic data inversions. The left panels depict the evolution of the best model realization over the course of the inversions. The right panels show the objective function values for the best 150 model realizations at the conclusion of the inversion. In all cases, a generation was composed of 170 model realizations that were evaluated by the objective function. Note that the convergence rates for all cases were similar, with no obviously significant performance differences.

Inspection of the final distribution of objective function values illustrated in the right panels of Fig. 41 suggests that the best performance was achieved by the inversion of vector acoustic transfer functions, particularly for the case where the buried sensor depths were exactly known. The greatest objective function values were achieved when scalar acoustic transfer functions were inverted.

Note that the simulation of sensor burial depth errors did not result in increased objective function values when inverting combined scalar-vector transfer functions as suggested by the marginal sensitivity analysis. Recall that the analysis of sensitivity to sensor depth errors was performed while holding all other geoacoustic parameters constant at their correct values, a circumstance that was most improbable in the context of the inversion process. Instead, the presence of sensor burial depth errors resulted in convergence on a set of geoacoustic parameters that differed significantly from those used to generate the synthetic data set (see Fig. 44). Therefore, assessment of inversion performance was not as simple as evaluating the distributions of objective function values at the conclusion of the inversion.

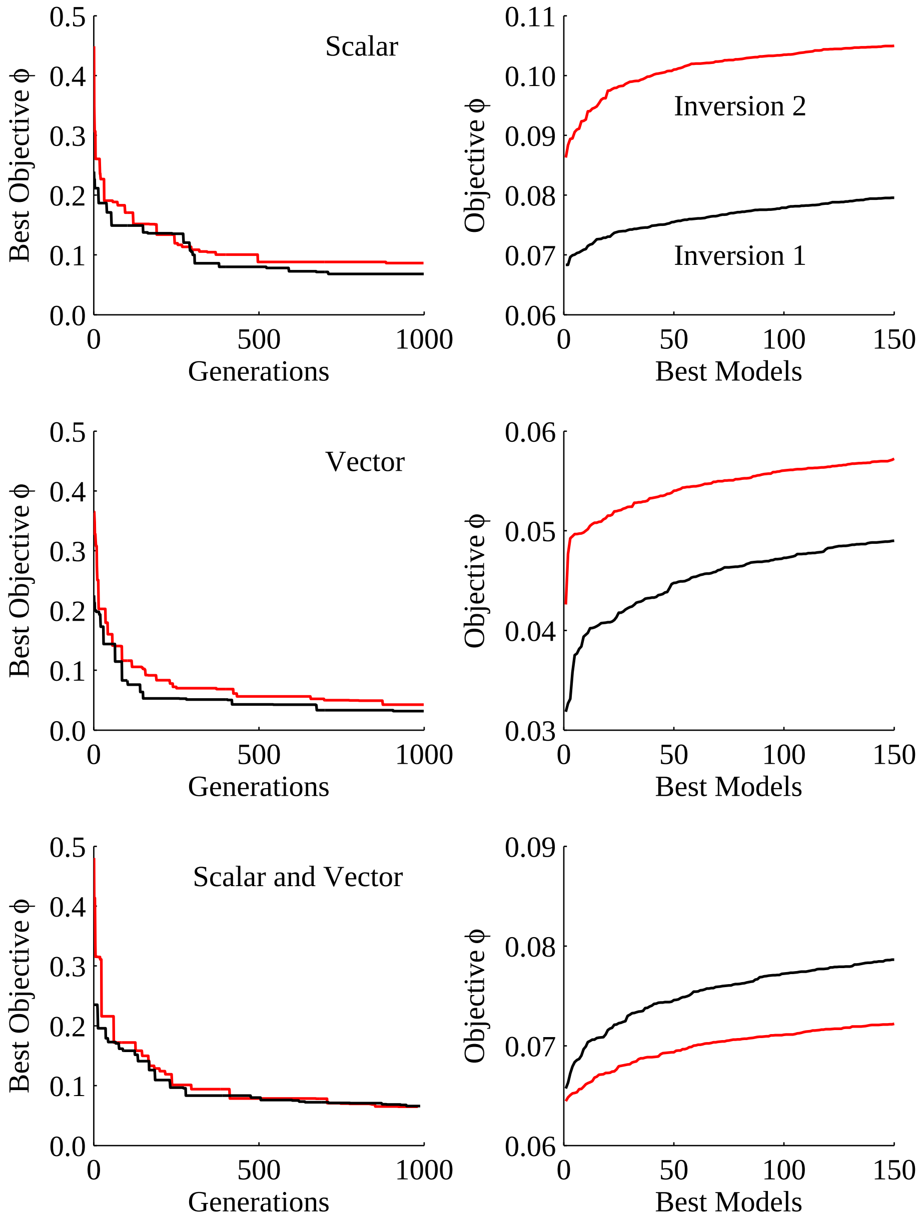

Figure 41. Convergence for inversion of synthetic acoustic transfer functions. The left panels depict the evolution of the best model realization over the course of the inversions. The right panels show values for the best 150 model realizations at the conclusion of each inversion. The simulated environment was parameterized as shown in Table 10. Each generation was populated by 170 models that were evaluated by the objective function.

Results for inversion of scalar acoustic transfer functions are summarized as Fig. 42 and Table 4. Inversion 1 estimates (e.g., no sensor burial depth errors) for the sediment density and compression wave speed in the first layer were both within 2% of their true values. Estimates in the thin, elastic layer were considerably less accurate with errors exceeding 20%. Estimation of the characteristic impedance in this layer was improved where the error was 8%, thus confirming the tendency for improved estimates of the characteristic impedance relative to individual estimates of the density and compression wave speed that was suggested by the sensitivity analysis. Estimates of the thickness of the first and second layers were within 7% and 40% of their true values, respectively. The characteristic impedance in the sediment half space was estimated within 3% of the true value. Independent estimates of density and compression wave speed were not accurate. In no layer did the inversion converge on a value for the shear wave speed.

Inversion 2 estimates (e.g. sensor burial depth errors) were poor. Density and compression wave speed estimates drifted to the limits of the parameter bounds (e.g. 1.0 to 2.5 gm/cm^3 and 1400 to 2800 m/s). While the characteristic impedance estimated for the first layer appears to be quite good, it was the result of the parameter bounds and not due to good inversion performance. Thus, it was important to verify that the density and compression wave speed estimates had not drifted to the parameter bounds when interpreting the characteristic impedance. Sensor burial depth errors also degraded the ability to resolve the second layer and to estimate the characteristic impedance in the half space. In short, the synthetic inversion performed with sensor burial depth errors failed to converge on any of the geoacoustic parameters, thus confirming the expected sensitivity of the acoustic transfer functions to path length errors, and the deleterious effect on the inversion.

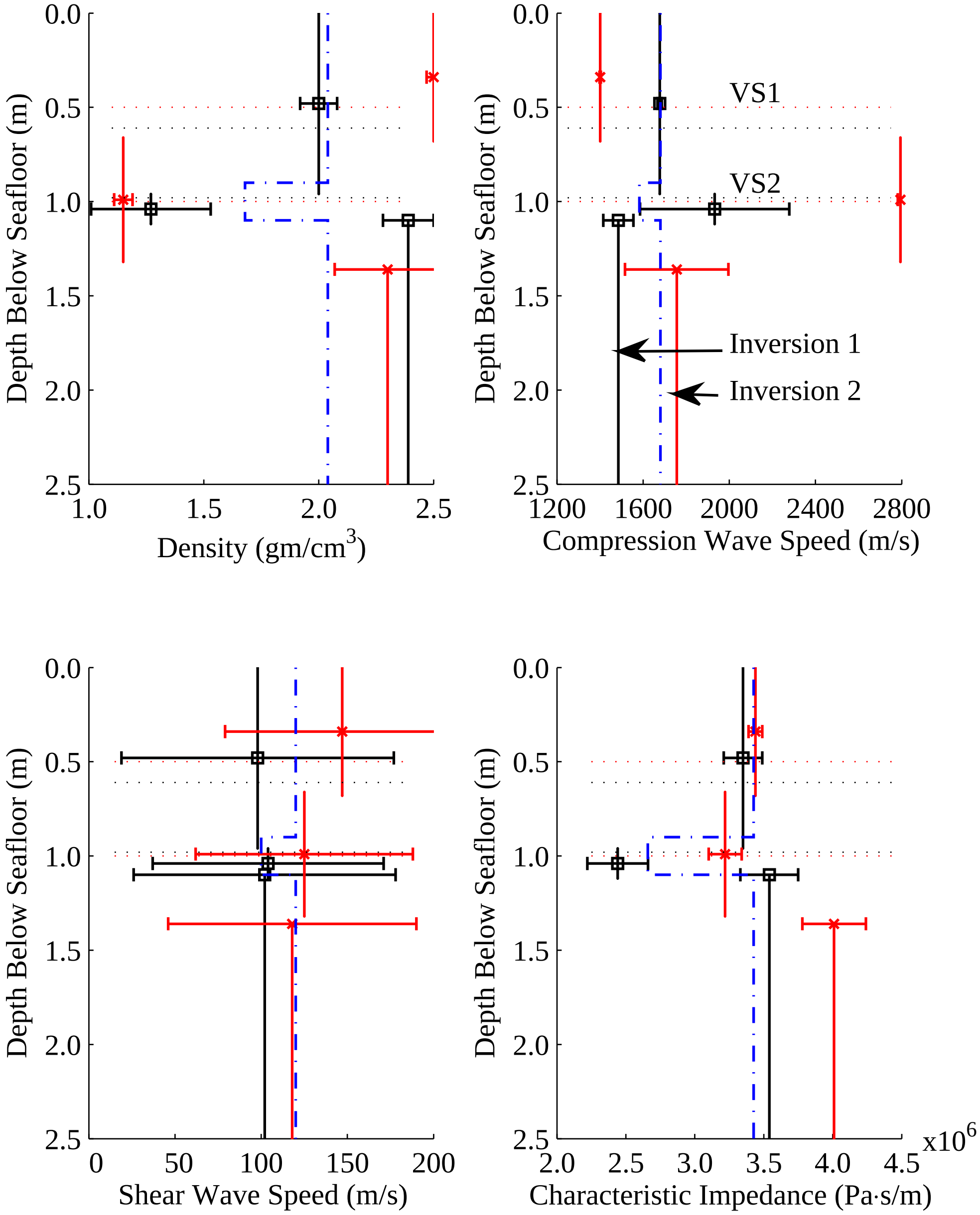

Figure 42. Inversion of synthetic scalar acoustic transfer functions. Parameters of the simulated environment are indicated by the blue dot-dash line. A thin, low impedance elastic layer was located at a nominal depth of one meter.

Table 4. Inversion of synthetic scalar acoustic transfer functions. The synthetic data set was generated using buried sensor depths of 61 and 98 cm for VS1 and VS2, respectively. Inversion 1 addresses the case where the sensor depths were exactly known. Inversion 2 treats the case where the sensor depths were not exactly known. Inversion 2 was run using buried sensor depths of 50 and 100 cm in the forward model.

Layer	**Parameter**	**Units**	**Value**	**Inversion 1**		**Inversion 2**	
				μ	σ	μ	σ
Water Column	Depth	m	16.7	16.1	0.2	17.5	0.0
	Sound Speed	m/s	1531	1543	4	1550	0
Sediment Layer One	Layer Thickness	cm	90	96	3	68	1
	Sediment Density	g/cm^3	2.04	2.00	0.08	2.50	0.03
	Compression Wave Speed	m/s	1680	1677	10	1401	3
	Shear Wave Speed	m/s	120	98	79	147	68
	Characteristic Impedance	MPa·s/m	3.43	3.35	0.14	3.44	0.05
Sediment Layer Two	Layer Thickness	cm	20	12	5	62	3
	Sediment Density	g/cm^3	1.68	1.27	0.26	1.15	0.04
	Compression Wave Speed	m/s	1583	1932	346	2794	12
	Shear Wave Speed	m/s	100	104	67	125	63
	Characteristic Impedance	MPa·s/m	2.66	2.44	0.22	3.22	0.12
Sediment Half Space	Sediment Density	g/cm^3	2.04	2.39	0.11	2.30	0.23
	Compression Wave Speed	m/s	1680	1485	70	1756	240
	Shear Wave Speed	m/s	120	102	76	118	72
	Characteristic Impedance	MPa·s/m	3.43	3.54	0.21	4.01	0.23

Results for inversion of vector acoustic transfer functions are summarized as Fig. 43 and Table 5. Parameter estimates were improved relative to the scalar inversion case. Estimates for density and compression wave speed in the first layer were within 0.5% of their true values. In the second layer, they were within 10% of their true values. Estimates of the characteristic impedance were within 1% and 4% in the first and second layers, respectively. Layer thickness estimates were within 2% and 20%. Shear wave speed estimates were within 20% of the true values in the first two layers. Parameter estimates in the half space were similarly improved with density, compression wave speed and characteristic impedance estimates within 11%, 8% and 1% of their true values, respectively. Shear wave speed was not resolved in the half space.

As before, injection of sensor burial depth errors resulted in significant degradation in the parameter estimates. While the density and compression wave speed estimates drifted off their true values, the estimates were not entirely controlled by the parameter bounds allowed by the inversion. Therefore, estimates of the characteristic impedance were controlled by the inversion process as opposed to the parameter bounds. The characteristic impedance estimated for the first and second layers were both within 5% of the true value for the first layer, suggesting that the ability to resolve the second layer was lost. Inversion results also suggested that the sensor burial depth errors had less of an impact on estimates in the half space where the characteristic impedance was estimated within 2% of the true value. Thus, sensor burial depth errors appear to have eliminated the ability to resolve density and compression wave speed independently. The ability to resolve the thin, low impedance layer was also lost. However, the inversion did provide good estimates for the average characteristic impedance in the sediments.

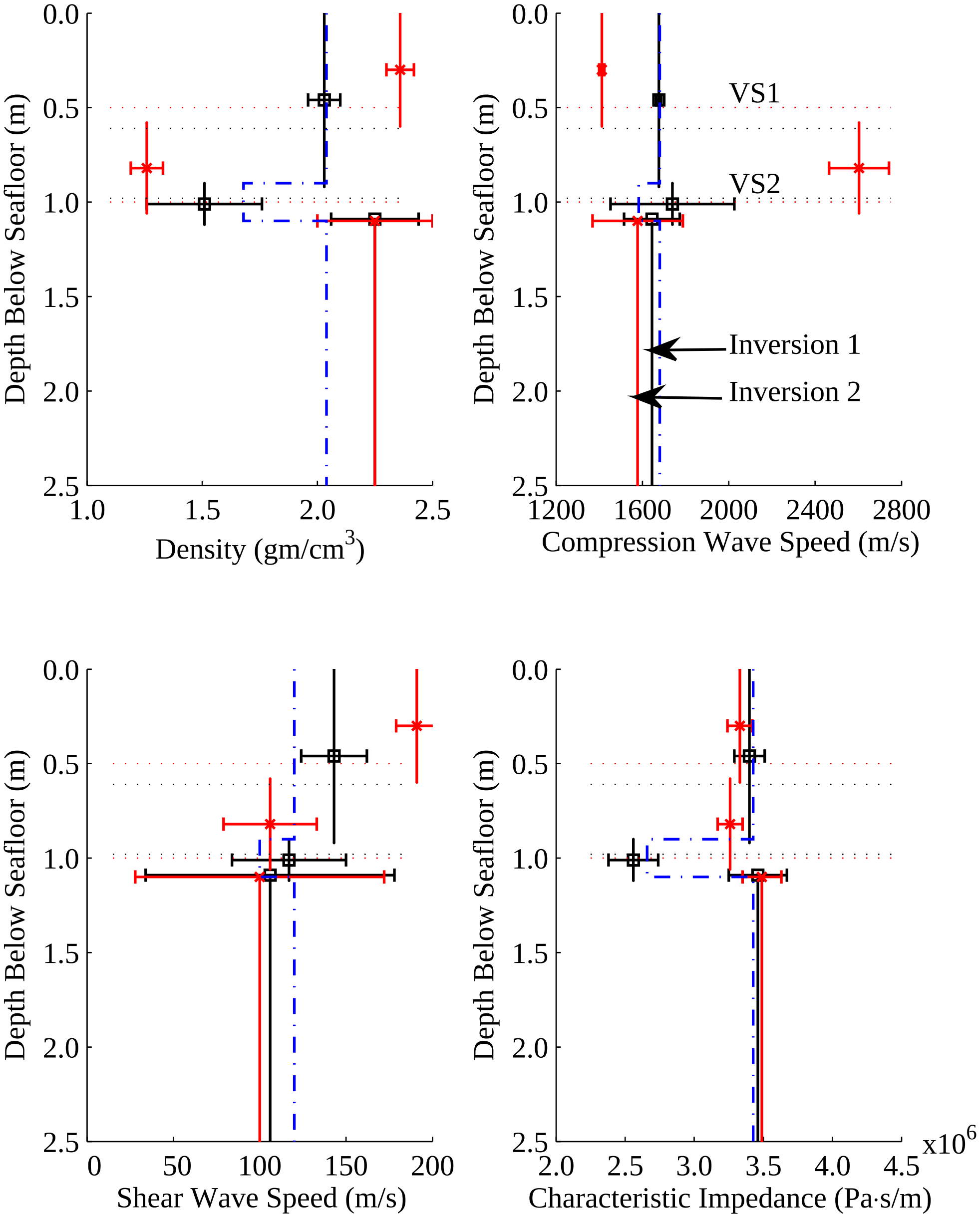

Figure 43. Inversion of synthetic vector acoustic transfer functions. Parameters of the simulated environment are indicated by the blue dot-dash line. A thin, low impedance elastic layer was located at a nominal depth of one meter.

Table 5. Inversion of synthetic vector acoustic transfer functions. The synthetic data set was generated using buried sensor depths of 61 and 98 cm for VS1 and VS2, respectively. Inversion 1 addresses the case where the sensor depths were exactly known. Inversion 2 treats the case where the sensor depths were not exactly known. Inversion 2 was run using buried sensor depths of 50 and 100 cm in the forward model.

Layer	**Parameter**	**Units**	**Value**	**Inversion 1**		**Inversion 2**	
				μ	σ	μ	σ
Water Column	Depth	m	16.7	16.9	0.6	17.1	0.5
	Sound Speed	m/s	1531	1536	19	1511	15
Sediment Layer One	Layer Thickness	cm	90	92	2	60	3
	Sediment Density	g/cm^3	2.04	2.03	0.07	2.36	0.06
	Compression Wave Speed	m/s	1680	1676	12	1412	12
	Shear Wave Speed	m/s	120	143	19	191	12
	Characteristic Impedance	MPa·s/m	3.43	3.40	0.11	3.33	0.09
Sediment Layer Two	Layer Thickness	cm	20	16	5	44	3
	Sediment Density	g/cm^3	1.68	1.51	0.25	1.26	0.07
	Compression Wave Speed	m/s	1583	1739	287	2603	139
	Shear Wave Speed	m/s	100	117	33	106	27
	Characteristic Impedance	MPa·s/m	2.66	2.56	0.18	3.26	0.09
Sediment Half Space	Sediment Density	g/cm^3	2.04	2.26	0.19	2.25	0.25
	Compression Wave Speed	m/s	1680	1544	129	1578	209
	Shear Wave Speed	m/s	120	106	72	100	72
	Characteristic Impedance	MPa·s/m	3.43	3.46	0.21	3.49	0.14

Results for inversion of combined scalar-vector acoustic transfer functions are summarized as Fig. 44 and Table 6. Performance of the inversion was broadly characterized as intermediate between that for the previous two cases (e.g., scalar transfer functions and vector transfer functions). In the absence of sensor burial depth errors, the inversion successfully resolved the density and compression wave speed independently. The thin, low impedance layer was also resolved. Inversion performance in the half space was more consistent with inversion of scalar transfer functions where only the characteristic impedance was resolved. Shear wave speed estimates were degraded relative to those attained with vector transfer functions.

In the presence of sensor burial depth errors, the characteristic impedance was estimated within 5% of the true value for the first layer and half space, the ability to resolve the thin, low impedance layer having been lost.

Results for the inversion of synthetic data indicate that the best and worst performance were obtained by inversion of vector transfer functions and scalar transfer functions respectively. While the differences were not overwhelming, inversion of vector acoustic transfer functions provided improved resolution of the density and compression wave speed in the first two layers. While the ability to resolve the thin, low impedance layer was lost by all inversions performed with sensor burial depth errors, inversion of vector acoustic transfer functions provided the best estimates of the characteristic impedance in an average sense.

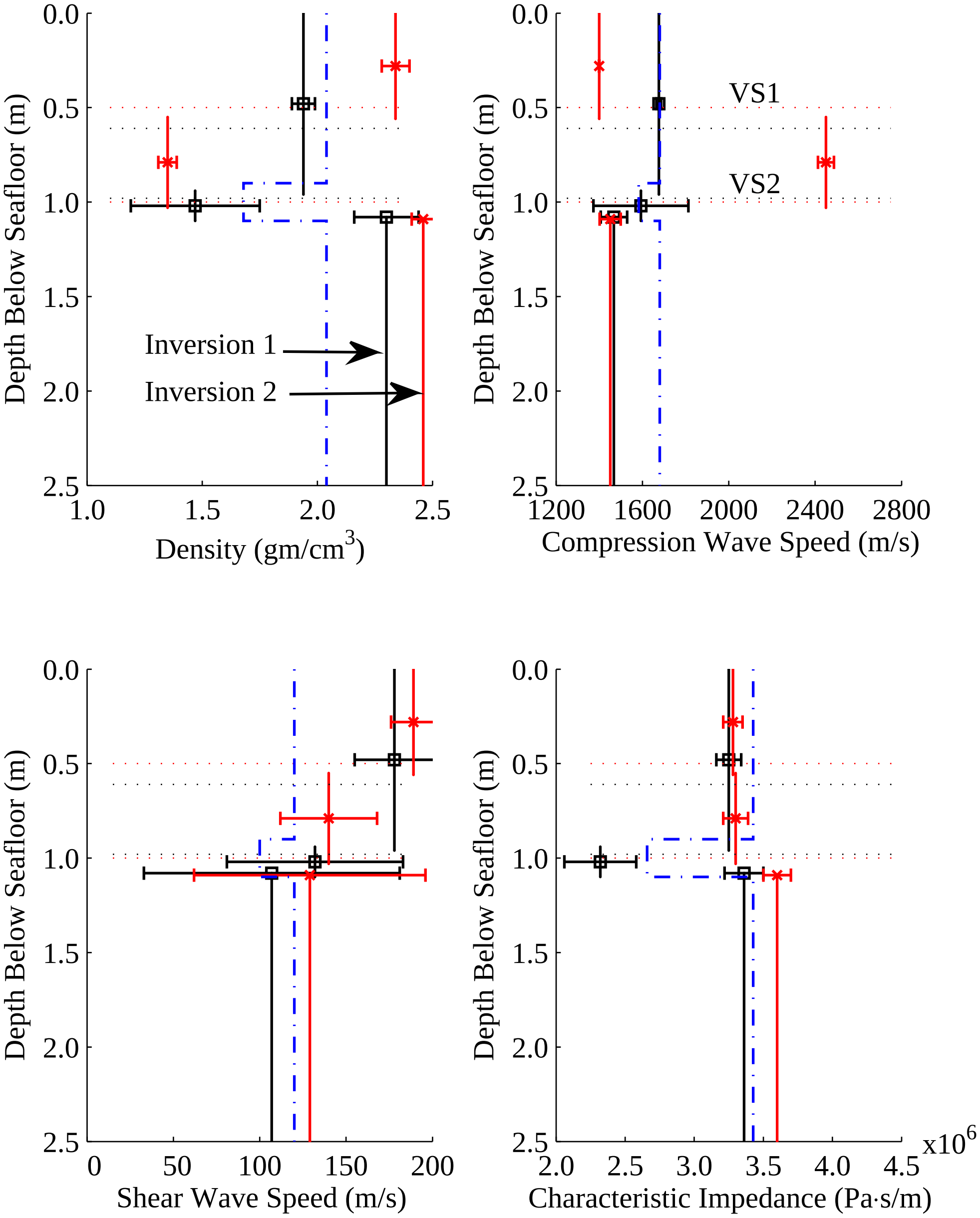

Figure 44. Inversion of synthetic scalar–vector acoustic transfer functions. Parameters of the simulated environment are indicated by the blue dot-dash line. A thin, low impedance elastic layer was located at a nominal depth of one meter.

Table 6. Inversion of synthetic scalar–vector acoustic transfer functions. The synthetic data set was generated using buried sensor depths of 61 and 98 cm for VS1 and VS2, respectively. Inversion 1 addresses the case where the sensor depths were exactly known. Inversion 2 treats the case where the sensor depths were not exactly known. Inversion 2 was run using buried sensor depths of 50 and 100 cm in the forward model.

Layer	**Parameter**	**Units**	**Value**	**Inversion 1**		**Inversion 2**	
				μ	σ	μ	σ
Water Column	Depth	m	16.7	16.7	0.3	16.0	0.0
	Sound Speed	m/s	1531	1549	3	1549	0
Sediment Layer One	Layer Thickness	cm	90	96	3	56	1
	Sediment Density	g/cm^3	2.04	1.94	0.05	2.34	6–
	Compression Wave Speed	m/s	1680	1676	11	1400	1
	Shear Wave Speed	m/s	120	178	23	189	13
	Characteristic Impedance	MPa·s/m	3.43	3.25	0.09	3.28	0.07
Sediment Layer Two	Layer Thickness	cm	20	11	4	46	2
	Sediment Density	g/cm^3	1.68	1.47	0.28	1.35	0.04
	Compression Wave Speed	m/s	1583	1593	220	2450	37
	Shear Wave Speed	m/s	100	132	51	140	28
	Characteristic Impedance	MPa·s/m	2.66	2.32	0.26	3.30	0.09
Sediment Half Space	Sediment Density	g/cm^3	2.04	2.30	0.14	2.46	0.05
	Compression Wave Speed	m/s	1680	1468	61	1451	49
	Shear Wave Speed	m/s	120	107	74	129	67
	Characteristic Impedance	MPa·s/m	3.43	3.36	0.14	3.60	0.10

6.4 Inversion of SAX04 Field Data

Acoustic field data from the SAX04 experiment were inverted for the geoacoustic properties of the bottom. Inversions were performed using scalar field transfer functions, vector field transfer functions and both. Two different experiment configurations were assumed. In the first (e.g., Inversion A), the buried sensor depths were taken to be 61 and 98 cm as was estimated by a regularized inversion of acoustic field data [1]. A second inversion (e.g., Inversion B) was performed for which the buried sensors were assumed to have been at the intended burial depths of 50 and 100 cm.

Among the original goals of this study was an assessment of the value that knowledge of the vector field represented for the quality of the inversion result. However, that question must now be refined in light of results from the sensitivity study and synthetic data inversions. These analyses showed that information about sediment shear wave speed was carried by the suspension response of the buried vector sensor. Thus, it is not sufficient to discuss the value of the acoustic vector field because the information appears to have been associated with the sensor's response to the field, not the field itself. In a perfect world, with undistorted acoustic vector field measurements, sensitivity of the inversion to shear wave speed would have been lost. The case for the other geoacoustic parameters was not so clear.

As illustrated in Fig. 45, Inversion B converged on a solution with lower objective function value relative to Inversion A, where the assumed depths were based on the regularized inversion estimates [1]. Thus, the data would appear to be more consistent with sensor burial depths as originally planned. However, inversions of synthetic data showed that the quality of two inversions performed with distinct data sets (e.g., scalar and/or vector) could not be assessed based solely on the objective function distribution at the conclusion of the inversion.

Figure 45 also shows that the best objective function values achieved when inverting the acoustic field data were considerably greater than those achieved by the inversion of synthetic data. This was not unexpected because the synthetic inversions were performed using a noise free data set and a perfect forward model (e.g., the same code generated the synthetic data set). The addition of experimental noise and the impact of approximations implemented in the forward model functioned to limit the minimum objective function value attainable when inverting real data. Results of the marginal sensitivity analysis suggests that the ability of the inversion to resolve many of the geoacoustic parameters would have been compromised by objective function values on the order of 0.2 as illustrated in Fig. 45. Figures 31 through 40 suggest that objective function values on the order of 0.2 could result in a significant loss of resolution. For example, Fig. 31 shows that sediment density values within ±20% of the true value returned objective function values less than 0.2 (with all other parameters held at their correct values). However, this example is in some sense contrived because the probability of the inversion converging on the correct value for all model parameters except one is highly improbable (unless the objective function was insensitive that one parameter). The extent to which the point of convergence within the m-dimensional parameter space may have been relocated due to noise and modeling approximations is not well understood at present. Therefore, the remaining available option was to compare the inversion estimates to published results for the test site.

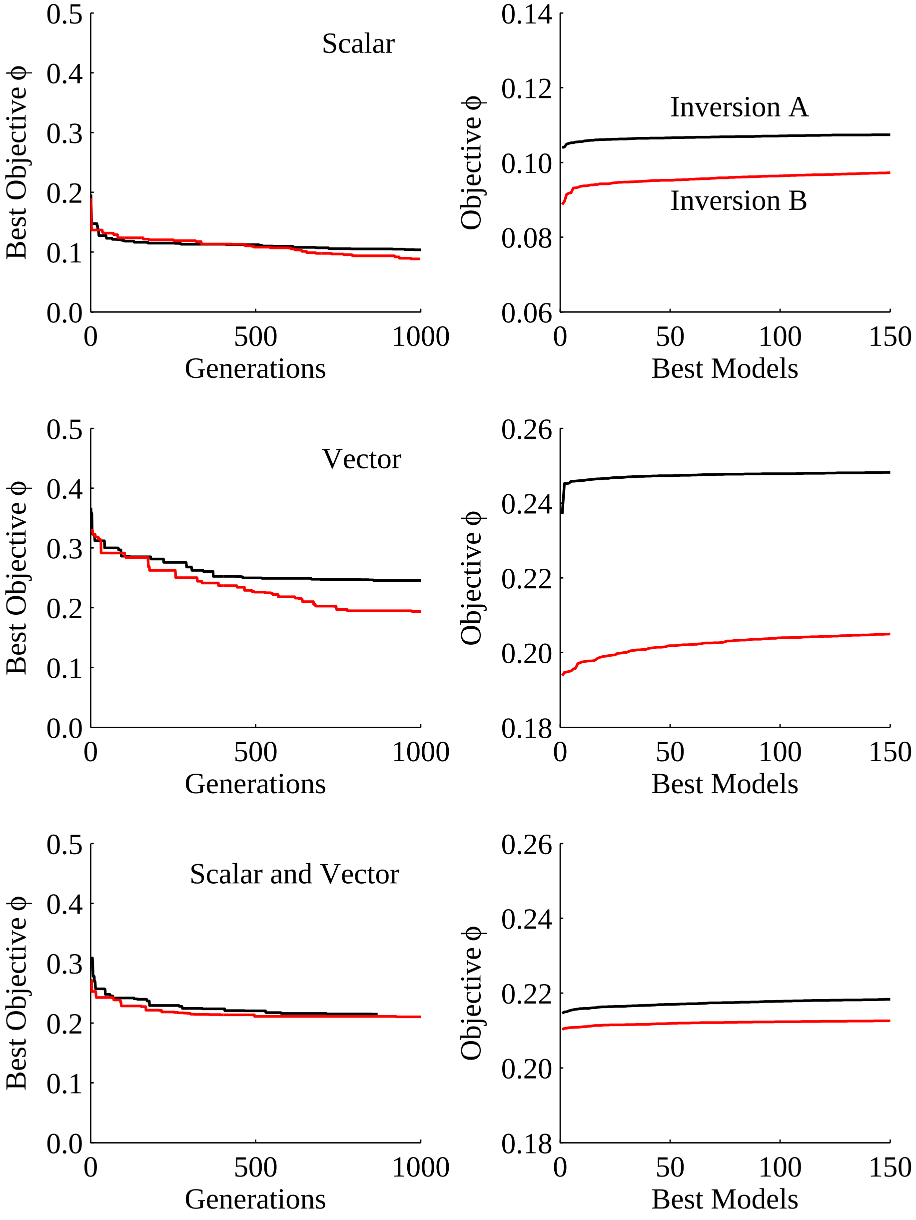

Figure 45. Convergence for inversion of SAX04 acoustic transfer functions. The left panels depict the evolution of the best model realization over the course of the inversions. The right panels show values for the best 150 model realizations at the conclusion of each inversion. Inversion A assumed buried sensor depths of 61 and 98 cm. Inversion B assumed sensors were buried at intended depths of 50 and 100 cm.

The result for inversion of scalar field transfer functions are summarized in Fig. 46 and Table 7. As shown in the figure, Inversion A returned a highly variable and improbable set of parameter estimates. For example, this inversion returned compression wave speed estimates ranging from 1595 to 2669 m/s within the top 23 cm of sediment. Inversion B returned a more simple parameterization, having reduced the environment to a 50 cm layer overlying a sediment half space. However, the density estimate in this first layer drifted to the parameter bound of 2.5 gm/cm^3. The compression wave speed estimate of 1610 m/s in the first layer was within 4% of the reported value. The density (1.99 gm/cm^3) and compression wave speed (1742 m/s) estimates in the half space were both within 4% of nominal values reported for the test site. The inversion did not converge on values for shear wave speed.

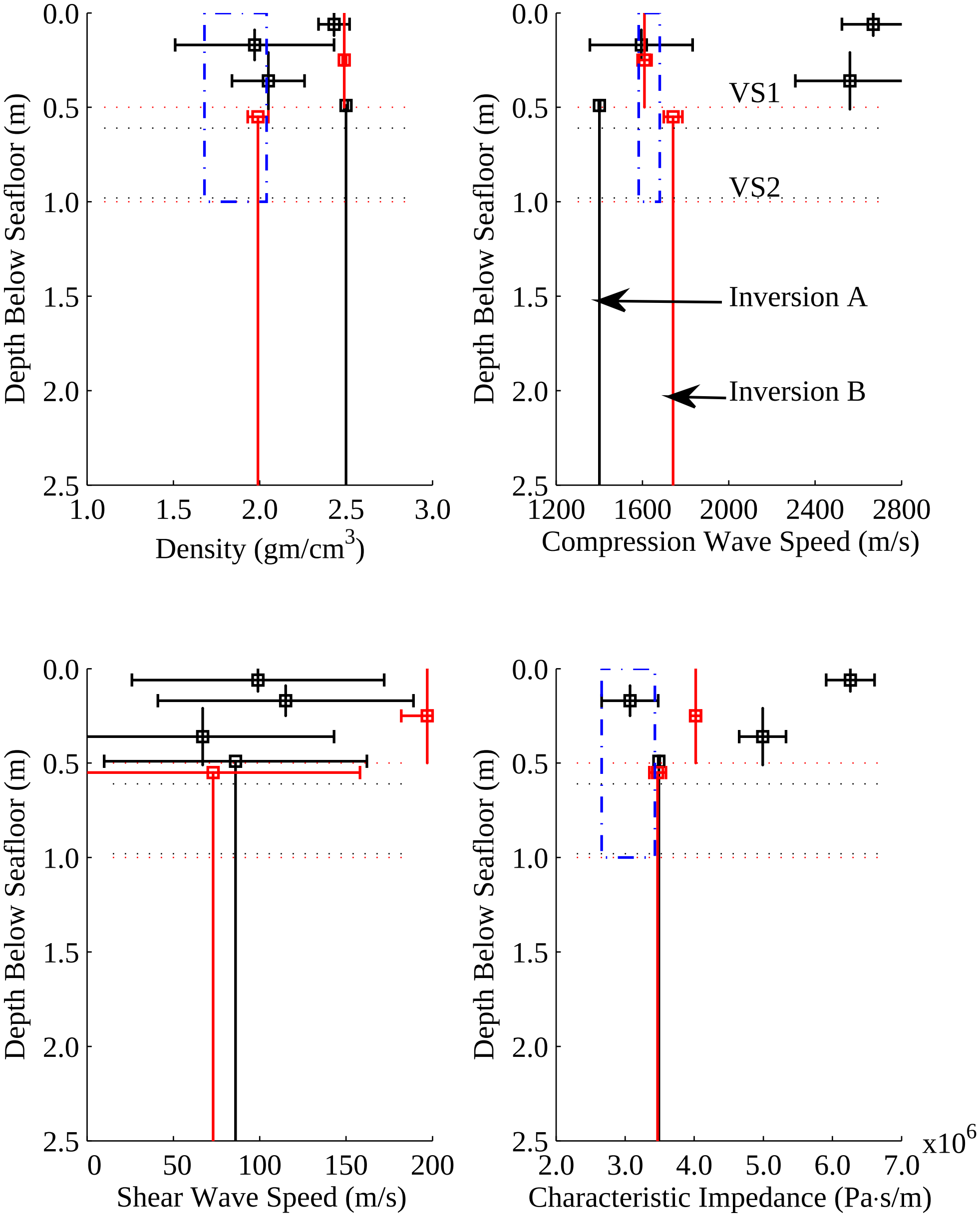

Figure 46. Inversion of SAX04 scalar acoustic transfer functions. Inversion A assumed buried sensor depths of 61 and 98 cm below the seafloor as reported [1]. Inversion B assumed sensors were buried at intended depths of 50 and 100 cm below the seafloor. The blue dot-dash boxes accompanying the density, compression wave speed and characteristic impedance bound the reported values in the top meter of sediment.

Table 7. Inversion of SAX04 scalar acoustic transfer functions. Estimate A assumed buried sensor depths of 61 and 98 cm below the seafloor as reported [1]. Estimate B assumed sensors were buried at intended depths of 50 and 100 cm below the seafloor.

Layer	**Parameter**	**Units**	**Estimate A**		**Estimate B**	
			μ	σ	μ	σ
Water Column	Depth	m	16.7	0.02	16.9	0.0
	Sound Speed	m/s	1541	1	1546	1
Sediment Layer One	Layer Thickness	cm	11	2	50	2
	Sediment Density	g/cm^3	2.43	0.09	2.49	0.01
	Compression Wave Speed	m/s	2669	145	1610	32
	Shear Wave Speed	m/s	99	73	197	15
	Characteristic Impedance	MPa·s/m	6.26	0.35	4.02	0.08
Sediment Layer Two	Layer Thickness	cm	12	4	–	–
	Sediment Density	g/cm^3	1.97	0.46	–	–
	Compression Wave Speed	m/s	1595	238	–	–
	Shear Wave Speed	m/s	115	74	–	–
	Characteristic Impedance	MPa·s/m	3.07	0.41	–	–
Sediment Layer Three	Layer Thickness	cm	26	4	–	–
	Sediment Density	g/cm^3	2.05	0.21	–	–
	Compression Wave Speed	m/s	2461	253	–	–
	Shear Wave Speed	m/s	67	76	–	–
	Characteristic Impedance	MPa·s/m	4.99	0.34	–	–
Sediment Half Space	Sediment Density	g/cm^3	2.50	0.01	1.99	0.06
	Compression Wave Speed	m/s	1401	3	1742	43
	Shear Wave Speed	m/s	86	76	73	85
	Characteristic Impedance	MPa·s/m	3.49	0.01	3.47	0.12

Results for inversion of vector field transfer functions are summarized in Fig. 47 and Table 8. Once again, Inversion A returned highly variable and improbable estimates for the density and compression wave speed in the sediment. While the shear wave speed converged on a value of 21 m/s in the half space, the estimate was assessed as unreliable. Recall that the shear wave speed was used to compute velocity transfer functions that applied only at the depth of each buried vector sensor. The velocity transfer functions computed from the shear wave speeds were used to compensate for corruption of vector field data provided by the buried vector sensors. Since the sediment half space to which this shear wave speed estimate was applied contained both buried vector sensors, it would only be reliable in the case where the shear wave speed was the same at both buried sensor depths.

Inversion B returned an unusual result in that the environmental parameterization was not simplified. Instead, the third layer and half space boundary were located at a depth of more than 2.5 m, thus diminishing their influence over the objective function and inversion outcome. This was the only occasion that the inversion process adopted this method of effectively simplifying the environmental parameterization, as opposed to reducing layer depths to values approaching zero as was intended during development of the software. The parameter estimates returned by this inversion were generally improbable, with the possible exception of the compression wave speed in the top 76 cm of sediment where the estimate of 1583 m/s was within 6% of the nominal value reported for this site (e.g. 1680 m/s).

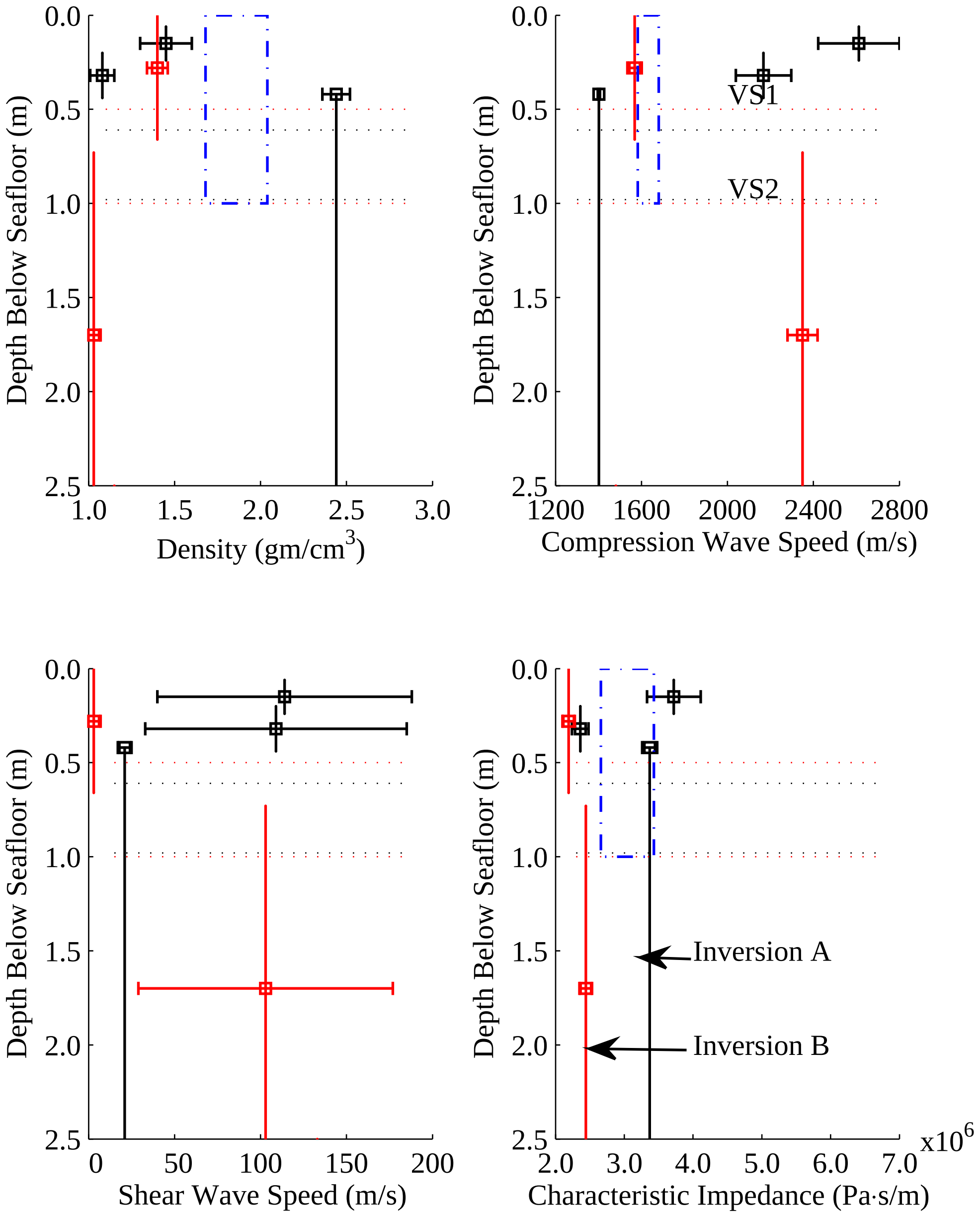

Figure 47. Inversion of SAX04 vector acoustic transfer functions. Inversion A assumed buried sensor depths of 61 and 0.98 cm below the seafloor as reported [1]. Inversion B assumed sensors were buried at intended depths of 50 and 100 cm below the seafloor.

Table 8. Inversion of SAX04 vector acoustic transfer functions. Estimate A assumed buried sensor depths of 61 and 98 cm below the seafloor as reported [1]. Estimate B assumed sensors were buried at intended depths of 50 and 100 cm below the seafloor.

Layer	**Parameter**	**Units**	**Estimate A**		**Estimate B**	
			μ	σ	μ	σ
Water Column	Depth	m	17.3	0.1	16.0	0.0
	Sound Speed	m/s	1547	1	1546	2
Sediment Layer One	Layer Thickness	cm	15	3	76	3
	Sediment Density	g/cm^3	1.45	0.16	1.40	0.06
	Compression Wave Speed	m/s	2611	189	1568	33
	Shear Wave Speed	m/s	114	74	3	4
	Characteristic Impedance	MPa·s/m	3.72	0.39	2.19	0.09
Sediment Layer Two	Layer Thickness	cm	20	4	188	5
	Sediment Density	g/cm^3	1.08	0.07	1.03	0.04
	Compression Wave Speed	m/s	2168	129	2349	70
	Shear Wave Speed	m/s	109	76	103	74
	Characteristic Impedance	MPa·s/m	2.36	0.12	3.17	0.02
Sediment Layer Three	Layer Thickness	cm	–	–	178	14
	Sediment Density	g/cm^3	–	–	1.98	0.21
	Compression Wave Speed	m/s	–	–	1614	134
	Shear Wave Speed	m/s	–	–	99	80
	Characteristic Impedance	MPa·s/m	–	–	3.17	0.02
Sediment Half Space	Sediment Density	g/cm^3	2.44	0.08	1.15	0.13
	Compression Wave Speed	m/s	1402	5	1481	107
	Shear Wave Speed	m/s	21	4	133	63
	Characteristic Impedance	MPa·s/m	3.37	0.11	1.73	0.13

The result for inversion of combined scalar-vector field transfer functions are summarized in Fig. 48 and Table 9. Inversion A returned highly variable and improbable estimates for the density and compression wave speed in the sediments. Estimates for Inversion B were more consistent with expectations, particularly in the half space. The lower panels of Fig. 48 illustrate the most promising results for the inversion of acoustic transfer functions. Both Inversion A and B returned estimates for the characteristic impedance that were consistent with each other and also with expectations for the test site. Perhaps most noteworthy was that both inversion results included a low impedance boundary located at a depth of approximately 60 cm. This is consistent with the hypothesis of a low impedance layer located at a depth of less than one meter that was offered to explain features in the SAX04 data set that were inconsistent with a sandy sediment half space [1].

A noteworthy feature of these inversions was the shear wave speed estimates. Two distinct and consistent sets of estimates were provided, one at each sensor depth. The shear wave speed at the depth of the shallow sensor (e.g., VS1) was estimated by Inversions A and B as 34 and 35 m/s, respectively. Estimates at the deeper sensor (e.g., VS2) were 74 and 69 m/s. The estimated values are generally consistent with regressions reported by Hamilton [2] for compression wave and shear wave speed in sandy sediments. The shear wave speed returned by Hamilton's regression was 52 m/s. These estimates were not however consistent with values based on SAX99 measurements [3], where the shear wave speed was reported as 120 m/s. At least two factors may account for the difference. First, disturbance of the seabed by the passage of Hurricane Ivan shortly before the experiment may have disrupted the bottom such that shear speeds were reduced. Also, the possibility that the act of sensor burial may have influenced the environment local to the sensors cannot be ruled out.

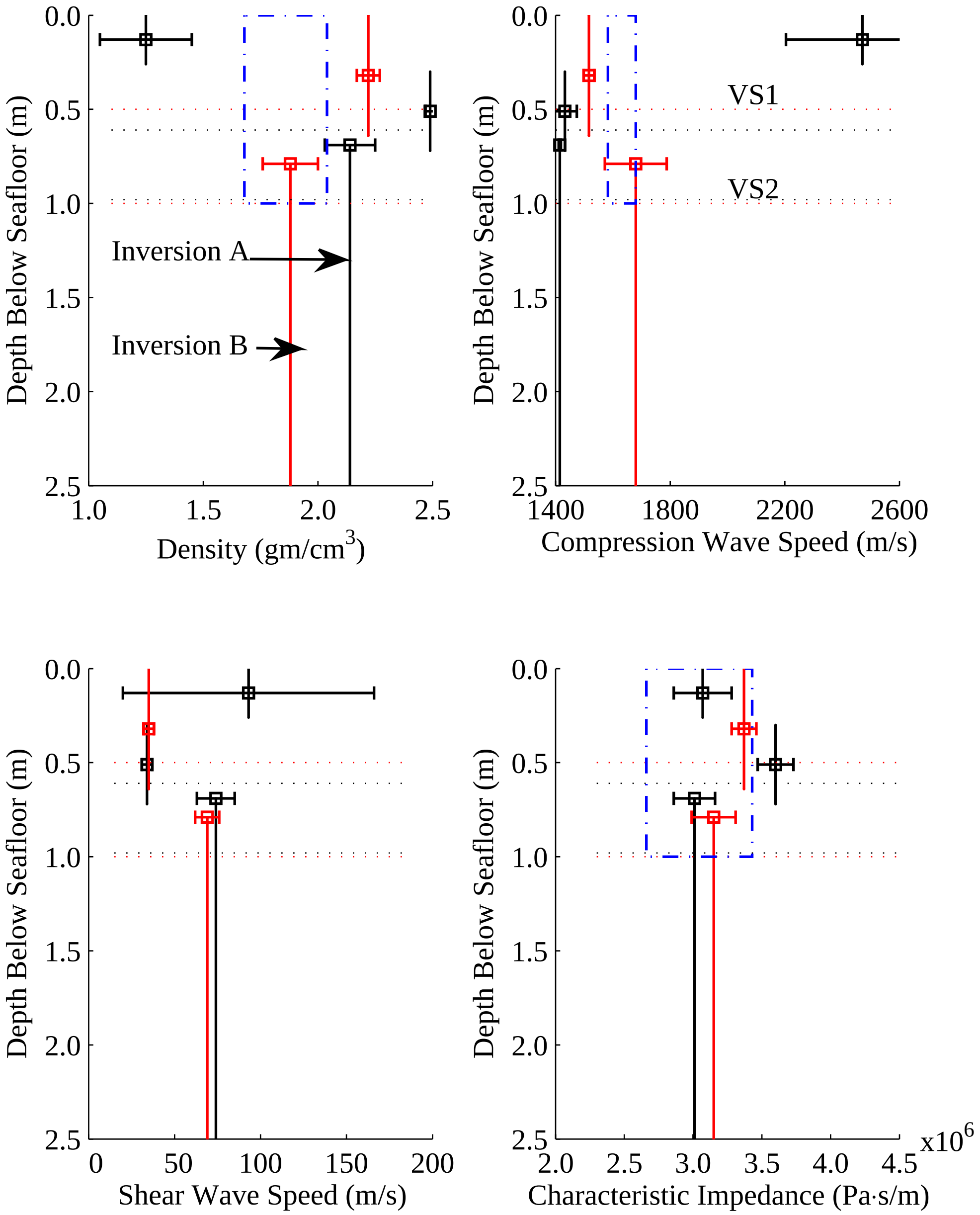

Figure 48. Inversion of SAX04 scalar–vector acoustic transfer functions. Inversion A assumed buried sensor depths of 61 and 98 cm below the seafloor as reported [1]. Inversion B assumed sensors were buried at intended depths of 50 and 100 cm below the seafloor.

Table 9. Inversion of SAX04 scalar–vector acoustic transfer functions. Estimate A assumed buried sensor depths of 61 and 98 cm below the seafloor as reported [1]. Estimate B assumed sensors were buried at intended depths of 50 and 100 cm below the seafloor. Note that summary results for the characteristic impedance of sediments were added for comparison.

Layer	**Parameter**	**Units**	**Estimate A**		**Estimate B**	
			μ	σ	μ	σ
Water Column	Depth	m	16.5	0.3	16.2	0.0
	Sound Speed	m/s	1550	2	1544	1
Sediment Layer One	Layer Thickness	cm	26	7	63	6
	Sediment Density	g/cm^3	1.25	0.20	2.22	0.05
	Compression Wave Speed	m/s	2471	267	1517	19
	Shear Wave Speed	m/s	93	73	35	3
	Characteristic Impedance	MPa·s/m	3.07	0.21	3.37	0.09
Sediment Layer Two	Layer Thickness	cm	37	5	–	–
	Sediment Density	g/cm^3	2.49	0.02	–	–
	Compression Wave Speed	m/s	1433	41	–	–
	Shear Wave Speed	m/s	34	3	–	–
	Characteristic Impedance	MPa·s/m	3.60	0.13	–	–
Sediment Half Space	Sediment Density	g/cm^3	2.14	0.11	1.88	0.12
	Compression Wave Speed	m/s	1415	4	1680	108
	Shear Wave Speed	m/s	74	11	69	7
	Characteristic Impedance	MPa·s/m	3.01	0.15	3.15	0.16

6.5 Discussion and Summary

Analysis results for inversion of complex acoustic transfer functions were presented. The analysis included a study of the objective function sensitivity to the geoacoustic parameters, inversions of a synthetic data set designed to emulate the geoacoustic parameterization reported for the test site, and inversions of acoustic field data collected during the SAX04 experiment.

The purpose of the sensitivity analysis was to numerically verify that the objective function Eq. 69 was responsive to variations in the geoacoustic parameters of interest such that a directed search algorithm could successfully exploit the behavior of the objective function to infer information about the geoacoustic environment. The study also assessed the relative value of information carried by the acoustic scalar and vector fields, to include the suspension response of the buried acoustic vector sensors. The study showed that the objective function was reasonably well balanced in the estimated parameters. The marginal sensitivity of the objective function was of the same order with respect to all of the geoacoustic parameters with one exception. It was shown that the objective function was not sensitive to the shear wave speed unless one of the buried vector sensors was in direct communication with the sediment in question and that a density contrast existed between the sensor and the sediment. The latter requirement was certain to be satisfied for realistic sediments as the TV–001 vector sensors were specifically designed to displace their own mass in seawater.

Inversions of a synthetic data set were performed to verify that the process returned valid parameter estimates when operating under ideal conditions. It was found that all three inversion methods (e.g. scalar, vector and scalar-vector) converged on the correct solution. Inversions that included vector field data performed somewhat better than inversion of scalar field data alone. With the exception of shear wave speed, it was not clear that the improvement was the result of a qualitative difference in information provided by the vector field measurements. When sensor burial depth errors were injected into the inversion, the ability to independently estimate the density and compression wave speed was degraded. However, estimates of the characteristic impedance remained reasonably accurate when the data set included measurements of the vector acoustic field.

Finally, inversions of field data collected during the SAX04 experiment were presented. While estimates of particular parameters were suggestive of the expected results, only the inversion of combined scalar-vector transfer functions returned a coherent and consistent depiction of the depth dependent sediment properties. However, even in this case, independent estimates of the density and compression wave speed were not attainable. Instead, the characteristic impedance of the sediments appear to have been estimated reasonably well. The shear wave speed at the depths of the two buried vector sensors were also estimated.

List of References

[1] J. C. Osler, D. M. F. Chapman, P. C. Hines, G. P. Dooley, and A. P. Lyons, “Measurement and modeling of seabed particle motion using buried vector sensors,” *IEEE Journal of Oceanic Engineering*, vol. 35, no. 3, pp. 516–537, July 2010.

[2] E. L. Hamilton, “V_p / V_s and Poisson’s ratios in marine sediments,” *Journal of the Acoustical Society of America*, vol. 66, no. 4, pp. 1093–1101, Oct. 1979.

[3] M. D. Richardson, K. B. Briggs, L. D. Bibee, P. A. Jumars, W. B. Sawyer, D. B. Albert, R. H. Bennett, T. K. Berger, M. J. Buckingham, N. P. Chotiros, P. H. Dahl, N. T. Dewett, P. Pleischer, R. Flood, C. F. Greenlaw, D. V. Holliday, M. H. Hulbert, M. P. Hutnak, P. D. Jackson, J. S. Jaffee, H. P. Johnson, D. L. Lavoie, A. P. Lyons, C. S. Martens, D. E. McGehee, K. D. Moore, T. H. Orsi, J. N. Piper, R. I. Ray, A. H. Reed, R. F. L. Self, J. L. Schmidt, S. G. Schock, F. Simonet, R. D. Stoll, D. Tang, D. E. Thistle, E. I. Thoros, D. J. Walter, and R. A. Wheatcroft, “Overview of SAX99: Environmental considerations,” *IEEE Journal of Oceanic Engineering*, vol. 26, no. 1, pp. 26–53, Jan. 2001.

CHAPTER 7

Inversion of Specific Acoustic Impedance

7.1 Inversion Data

The specific acoustic impedance provided an alternative approach to inversion of scalar and vector field data. Where use of acoustic transfer functions relied on the ratio of like acoustic quantities measured at two different locations, the inversion of impedance used the ratio of dissimilar quantities measured at a collocated point. Since complex acoustic transfer functions vary strongly with distance, errors in the sensor locations defining the end points for the acoustic path had a deleterious effect on inversion performance. The specific acoustic impedance, computed as the ratio of the acoustic pressure to particle velocity at a point, may reduce the adverse impact of sensor location uncertainties by eliminating errors in the measurement of sensor-to-sensor separations. Despite this relative improvement, sensor position errors may still degrade the performance of impedance based inversions, particularly where reflected acoustic energy is a significant component of the total signal.

Recall that the complex specific acoustic impedance used to support the inversions was provided for the buried sensors as Eq. 85 and restated below as

$$\widehat{Z}_a^{(\varepsilon)}\left(\omega,\vec{r}_n\right)=\frac{P\left(\omega,\vec{r}_n\right)}{U_s\left(\omega,\vec{r}_n,\rho_n,c_{s_n}\right)}=\frac{H_a^{(p)}\left(\omega,\vec{r}_1,\vec{r}_n\right)}{H_a^{(u)}\left(\omega,\vec{r}_1,\vec{r}_n\right)H_s\left(\omega,n\right)}, \tag{94}$$

where $H_s\left(\omega,n\right)=H_s^{(\varepsilon)}\left(\omega,\rho_n,c_{s_n}\right)$ when sensor n was beneath the seafloor and $H_s\left(\omega,n\right)=H_s^{(f)}\equiv 1$ when sensor n was suspended above the seafloor.

Figure 49 illustrates the specific acoustic impedance calculated at each of four acoustic vector sensors. Data used to compute the impedance were identical to that used for transfer function calculations. The real and imaginary parts of the impedance are provided in the upper and lower panels, respectively. Vector sensors 5 and 6 were suspended above the seafloor at 10 and 25 cm, respectively. Vector sensors 1 and 2 were buried beneath the seafloor at nominal depths of 50 and 100 cm, respectively. The sensor that provided data for each impedance measurement is indicated by the legend subscripts.

In considering the information that may be carried by the impedance, it is instructive to recall the trivial case of a plane wave propagating in free space as was discussed in section 1.2 (see page 4). In the case of a plane propagating wave, the specific acoustic impedance observed by an acoustic vector sensor would be equal to the characteristic impedance of the medium. Approximate values for the characteristic impedance of the seawater and sandy sediments during SAX04 were $1.6\text{x}10^6$ and $3.4\text{x}10^6$ Pa·s/m, respectively.

Information about the local environment was reflected as differences between the specific acoustic impedance and the characteristic impedance, including variations with frequency as illustrated in Fig. 49. In particular, any variation of the measured specific acoustic impedance from a constant, purely real quantity (e.g. characteristic impedance) represents either a feature of the environment that has influenced the wave field, or some distortion of the measurement as might occur in the case of a frequency dependent suspension response.

7.2 Objective Function Sensitivity Analysis

Sensitivity of the objective function to the geoacoustic parameters of interest was repeated to permit comparison of inversions based on impedance with those based on acoustic transfer functions. The analysis was based on the same synthetic data sets for both cases, having adopted the geoacoustic parameterization reported for the SAX04 experiment site [1]. The analysis was performed to determine if an objective function based on impedance would be less sensitive to sensor position errors than objective functions based on acoustic transfer functions as

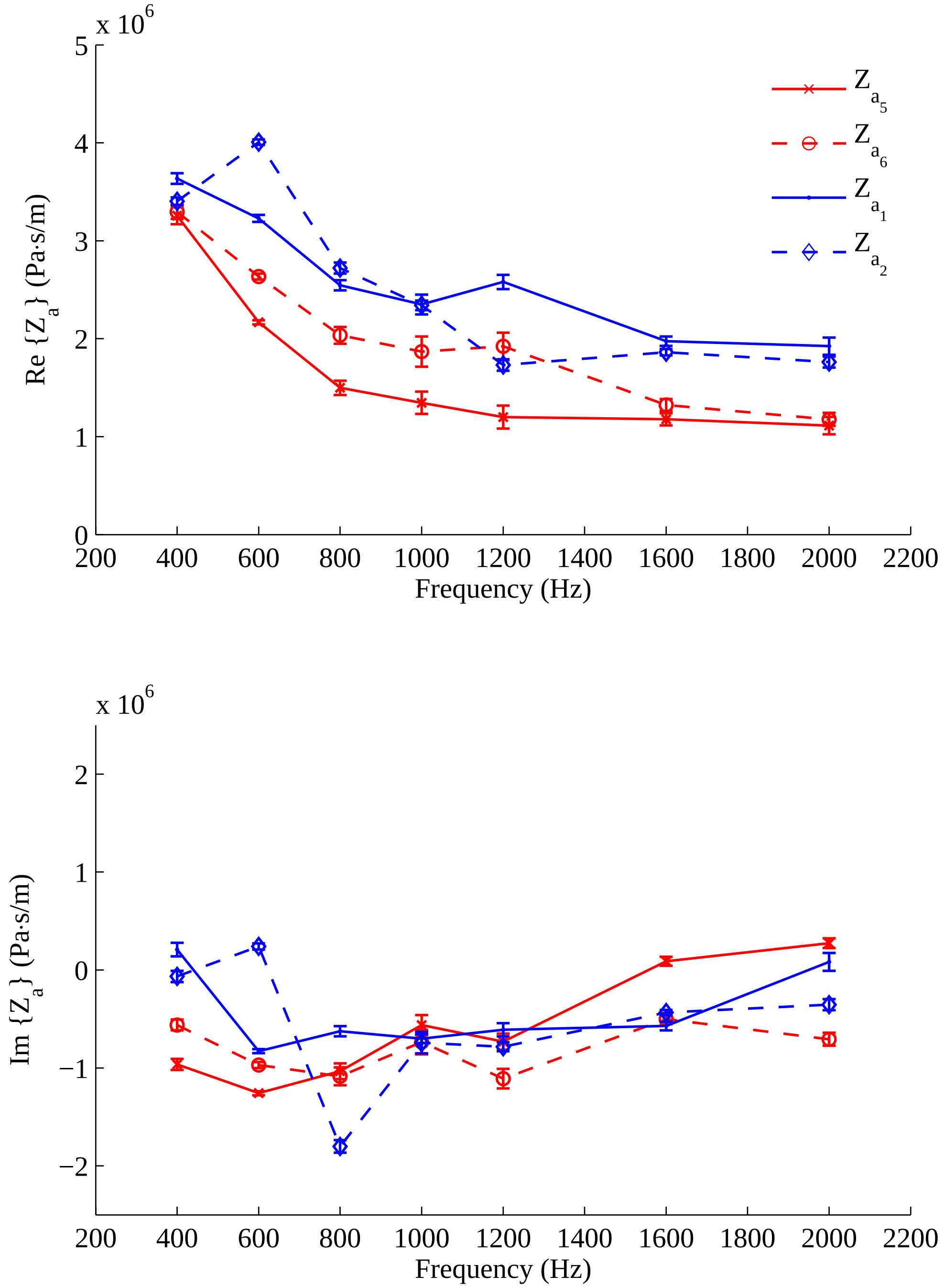

Figure 49. Specific acoustic impedance Z_a. Data measured with acoustic vector sensors VS1, VS2, VS5 and VS6. Error bars indicate one standard deviation.

was postulated. In addition, the analysis enabled a comparison of the sensitivity of these two objective function types to the geoacoustic parameters of interest. In the discussion that follows, sensitivity of the impedance based objective function is compared to sensitivity of the combined scalar-vector acoustic transfer function. Objective functions based on the acoustic transfer functions included both scalar and vector field data. Particulars of the geoacoustic parameterization adopted for this sensitivity study were as reported for the test site and were provided as Table 3 (see page 86).

Figure 50 illustrates the sensitivity of both the impedance and transfer function based objective functions to the depth and sound speed in the water column. Recall that estimation of the water column properties was not among the parameters of interest. Thus, objective functions were sought to minimize the influence of the water column properties. As shown in the figure, sensitivity of the impedance based objective function to the water column properties was reduced relative to that based on acoustic transfer functions. In addition, objective function values were virtually unchanged whether the acoustic vector field measurements in the sediment were modeled as having been exact or distorted by a frequency dependent suspension response of the buried sensors.

Figure 51 illustrates sensitivity of the objective function to the geoacoustic parameters of the first sandy layer. As shown in the figure, sensitivity of the objective function to the thickness of the layer and to the sediment density were increased relative to that realized with acoustic transfer functions. On the contrary, the sensitivity of the impedance based objective function to the compression wave speed was decreased relative to the transfer function based objective function. Finally, sensitivity of the objective function to estimation errors in the sediment shear wave speed was slightly increased. Only in the case of sediment shear wave speed did the suspension response of the positively buoyant vector sensor result in a significant change in sensitivity relative to the undistorted measurement of a neutrally buoyant sensor.

Figure 52 illustrates behavior of the impedance based objective function for variations in the geoacoustic properties of a thin muddy layer located at a nominal depth of one meter. As shown in the figure, the sensitivity of the objective function was generally increased, with the exception of the shear wave speed where the sensitivity was essentially unchanged.

Behavior of the objective function for variations in the geoacoustic properties of the sediment at a depth of 2.1 m is illustrated as Fig. 53. As was the case for the thin muddy layer, the sensitivity of the impedance based objective function to the sediment properties was generally increased relative to those based on acoustic transfer functions. However, the small increase in the shear wave speed sensitivity was inconsequential as has been shown for all cases in which the sensor is not embedded in the material in question.

A two dimensional sensitivity analysis was repeated to test the impedance based objective function for correlation between the sediment density and compression wave speed. Figure 54 illustrates the sensitivity of the objective function to variations in the geoacoustic properties of the first sandy layer. Values assumed for the compression wave speed and density are indicated by the square marker, with the solid red line representing the constant characteristic impedance. The red dashed lines indicate ±10% variation in the characteristic impedance of the medium. As shown in the figure, the correlation between these two parameters was modest as evidenced by elongation of the contours in the direction of constant characteristic impedance. However, there remained a single minimum within the inversion bounds that should facilitate the resolution of these two parameters.

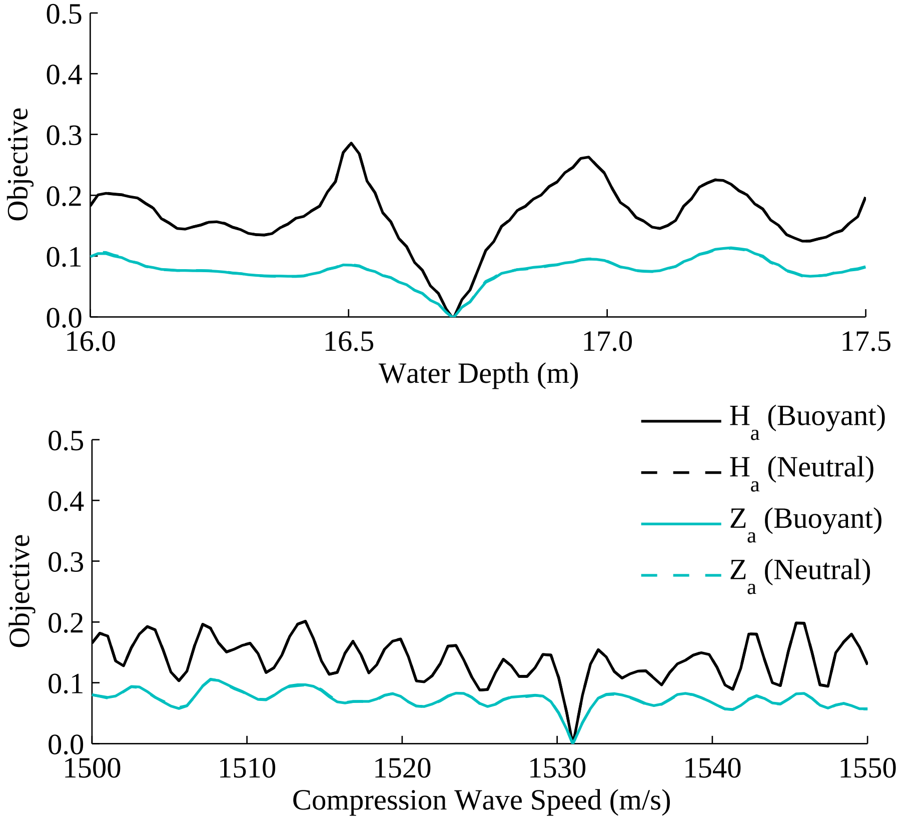

Figure 50. Objective function sensitivity ϕ_Z: water column

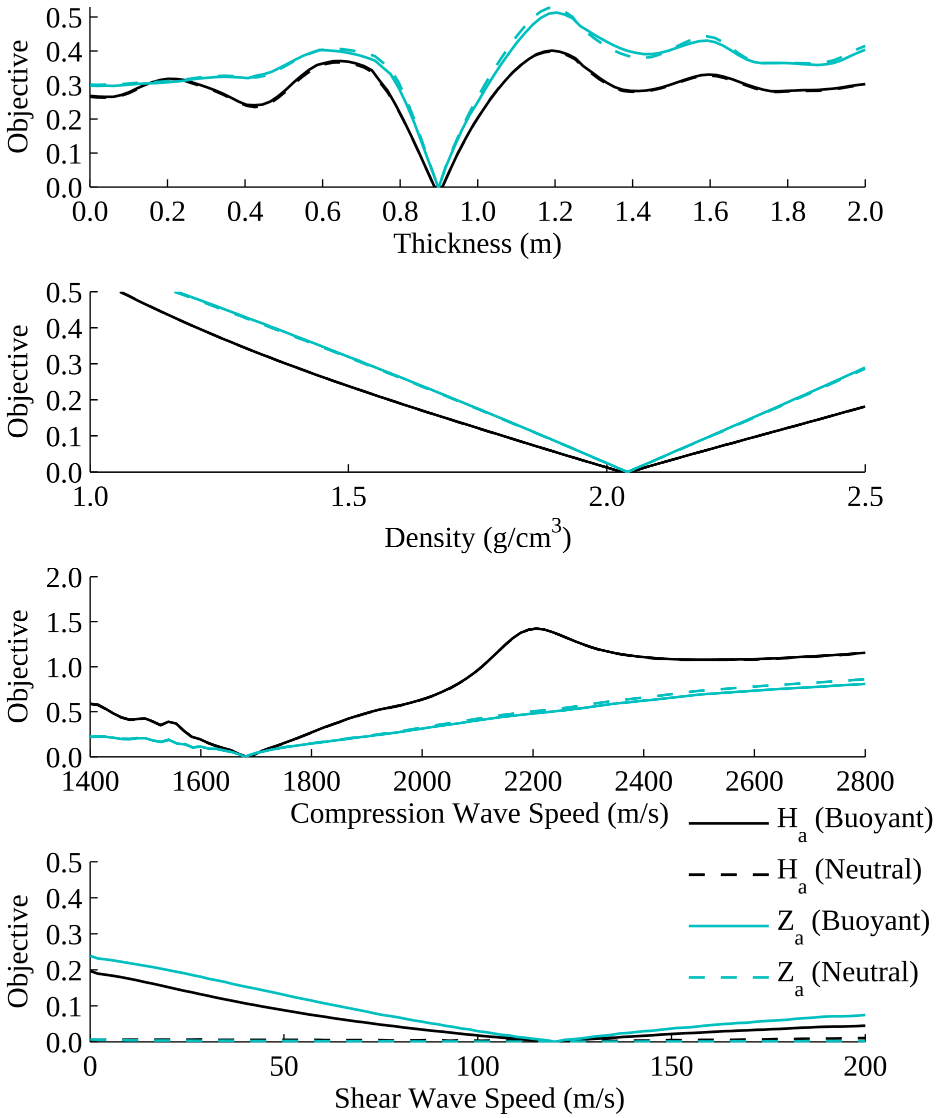

Figure 51. Objective function sensitivity ϕ_Z: layer one

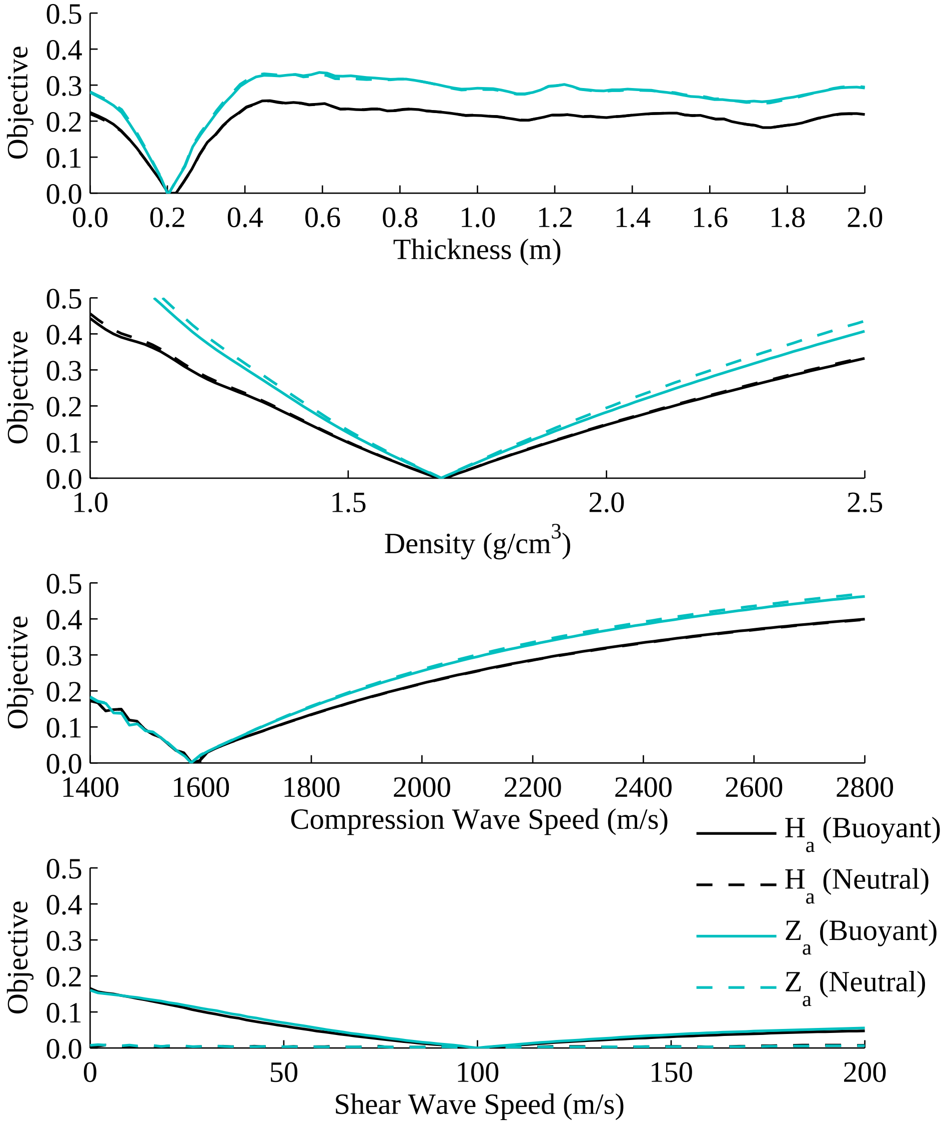

Figure 52. Objective function sensitivity ϕ_Z: layer two. Sensitivity of impedance based objective function to geoacoustic properties of a thin elastic layer located at a nominal depth of one meter.

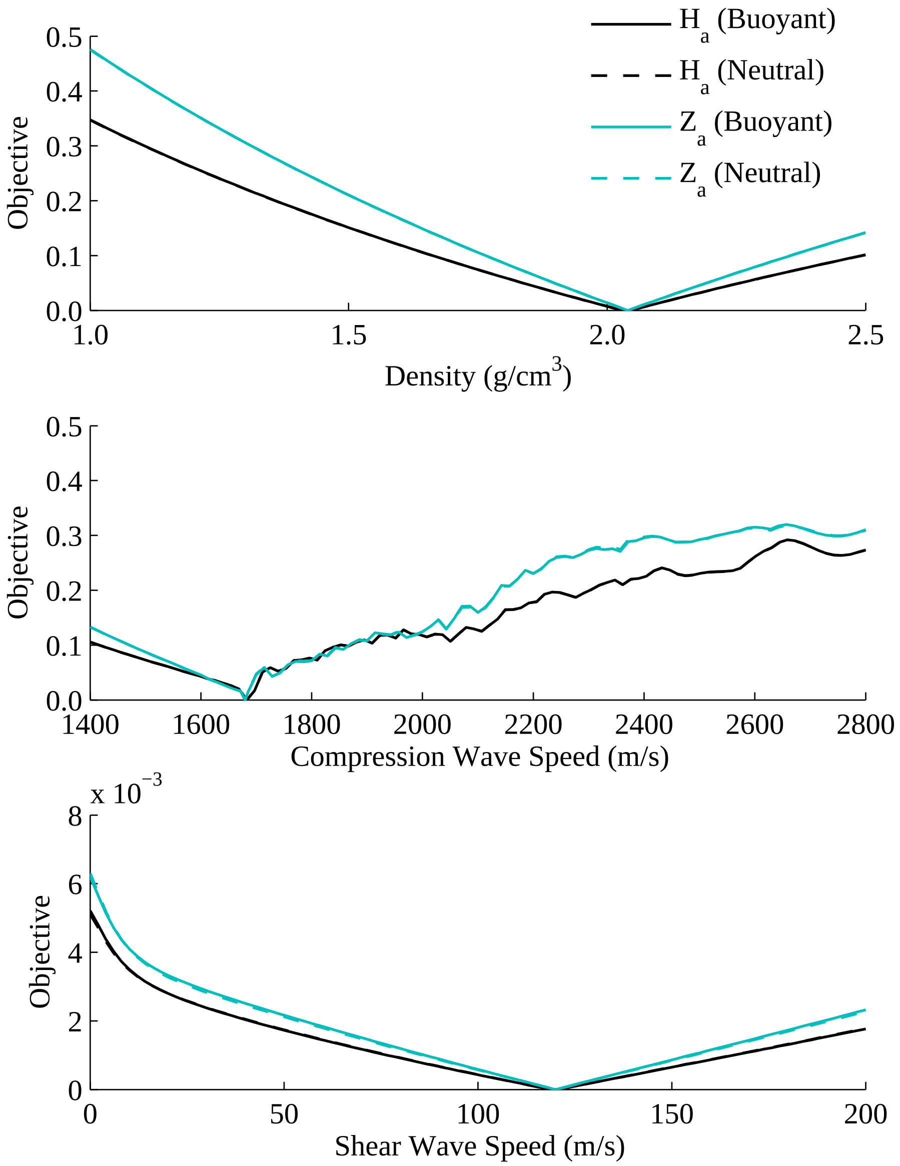

Figure 53. Objective function sensitivity ϕ_Z: half space. Sensitivity of impedance based objective function to geoacoustic properties of the sediment half space.

Figure 55 illustrates a similar result when analyzing the sensitivity of the objective function to changes in these parameters at a depth of 2.1 m. In this case, the objective function was much less sensitive and was least sensitive in the direction of constant characteristic impedance for this remote layer. Since this layer would only influence the objective function through reflection, it was not unexpected that the sensitivity varied most strongly with the characteristic impedance mismatch at this interface.

7.2.1 Sensor Location Errors

Figure 56 illustrates the sensitivity of the impedance based objective function to errors in the sensor positions. As shown in the figure, the impedance based objective function was less sensitive to errors in the sensor locations than objective functions based on the complex acoustic transfer functions (see Fig. 40).

The general reduction in sensitivity to uncertainty in the sensor positions resulted from the difference in the acoustic quantity used. Since the acoustic transfer functions vary strongly with distance, errors in the sensor locations equate to uncertainty in the path length over which the transfer function was computed. While less important for the magnitude of the transfer function, the phase error can be significant, particularly at higher frequencies. Since the specific acoustic impedance was computed at a point (as opposed to across a finite distance), it tended to be less affected by sensor location errors. Also note that Fig. 56 shows that the objective function was more sensitive to depth estimation errors for VS1 than to the deeper of the two buried sensors, VS2. Recall that the environmental parameterization for the synthetic data set included a low impedance reflector with a mid-plane depth of one meter. Thus, the greater sensitivity shown by the shallow sensor was due to changes in the specific acoustic impedance as the distance from this reflector was varied.

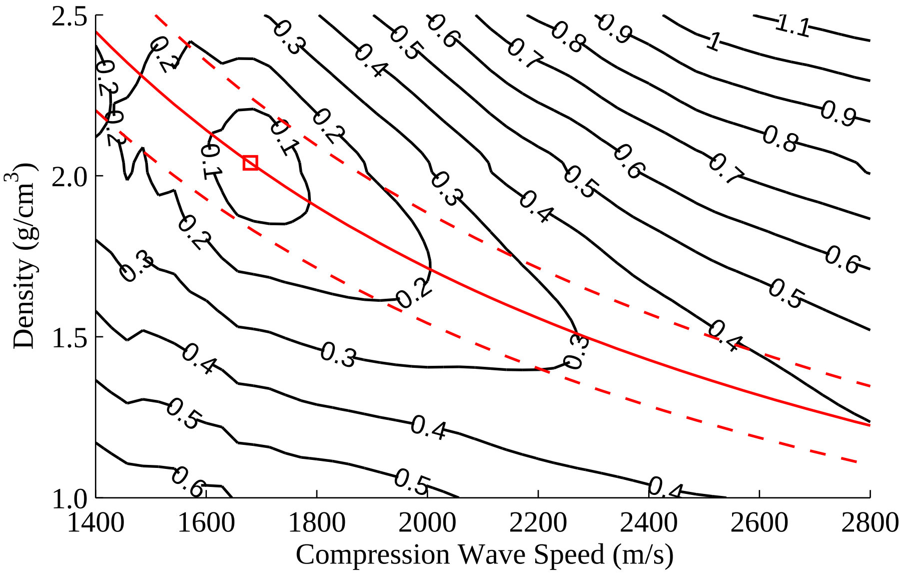

Figure 54. Objective function sensitivity ϕ_Z (2D): layer one. Objective function surface for variations in compression wave speed and density for the first sediment layer. Values providing a constant characteristic impedance equal to the assigned value are indicated by the red solid line. The dashed lines represent ±10%.

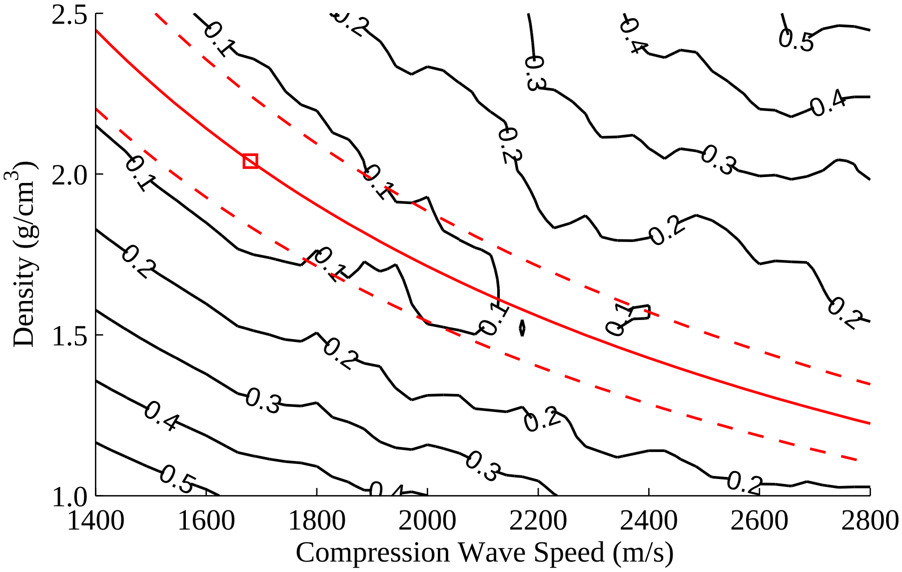

Figure 55. Objective function sensitivity ϕ_Z (2D): half space. Objective function surface for variations in compression wave speed and density in the sediment half space. Values providing a constant characteristic impedance equal to the assigned value are indicated by the red solid line. The dashed lines represent ±10%.

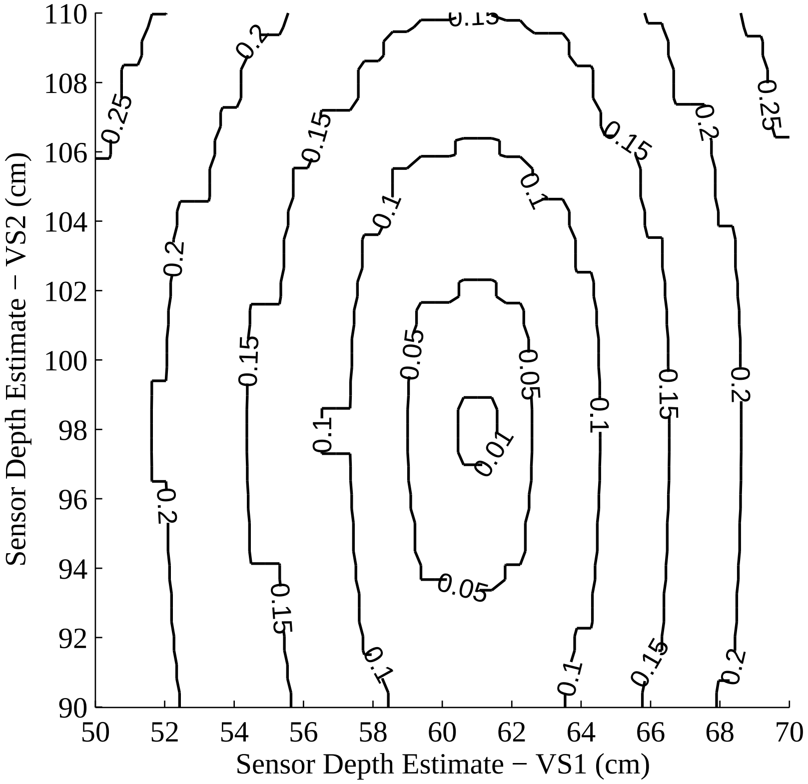

Figure 56. Objective function sensitivity ϕ_Z: sensor depth. Sensitivity of impedance based objective function to sensor burial depth errors. The synthetic data set was generated with VS1 and VS2 vector sensors located 61 and 98 cm beneath the sea floor, respectively. Objective function values were computed with various sensor burial depths included in the forward model. The sharp edges and corners of the contours resulted from 1 cm resolution for receiver locations implemented in the forward model.

7.3 Inversion of Synthetic Data

Inversion of a synthetic data set was conducted to verify performance of the method under ideal conditions. The environment used to generate the synthetic data set was characterized by a thin elastic layer as was used for the sensitivity study. Inversions with and without buried sensor depth errors were performed. In both cases, synthetic data were generated using buried sensor depths of 61 and 98 cm. Inversion 1 was performed using the correct buried sensor depths in the forward model during the inversion. Inversion 2 was performed using the planned sensor depths of 50 and 100 cm in the forward model during the inversion. Thus, Inversion 2 simulated the case where significant sensor burial depth errors existed.

Figure 57 illustrates the convergence behavior for inversion of the synthetic data set. The right panel shows the objective function values for the best 150 realizations tested by the inversion. It was this subset of the population that was used to estimate the probability distributions for the parameter estimates. The left panel provides the evolution of the best objective function value over the course of the inversion. As shown in the figure, the value of the best objective function decreased most quickly in the first 150 generations, after which convergence proceeded more slowly. Results for the inversion of synthetic acoustic impedance are summarized as Fig. 58 and Table 10.

Recall that the parameterization of the environment embedded in the inversion included a maximum of three finite sediment layers overlying a sediment half space. The method was designed to permit the elimination of unnecessary layers by omitting them from the forward model at run time. Inversion of synthetic data confirmed that the method reduced the complexity of the environmental parameterization to the minimum required by converging on a solution with only two finite sediment layers overlying a sediment half space as illustrated in Fig. 58.

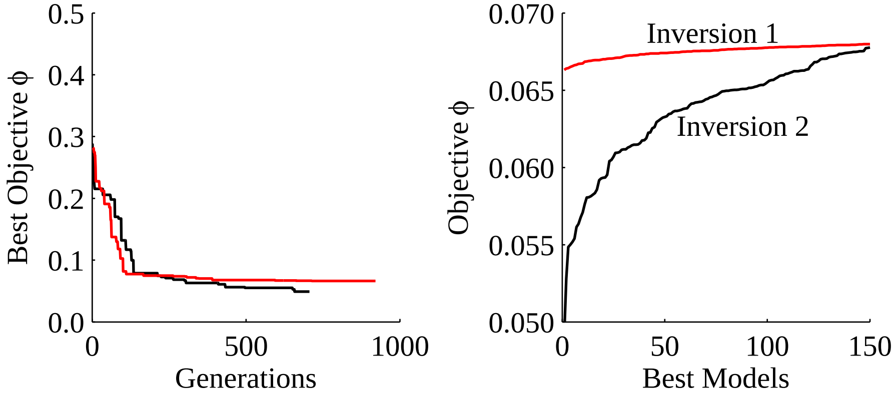

Figure 57. Convergence for inversion of synthetic acoustic impedance. The left panel depicts the evolution of the best model realization over the course of the inversions. The right panel shows values for the best 150 model realizations at the conclusion of each inversion. Each generation was populated by 170 models that were evaluated by the objective function.

In the absence of sensor burial depth errors, estimates of density and compression wave speed in the first layer were within 1% of the true values. The estimated thickness of the layer was within 3% and the shear wave speed was within 16%. Estimation errors in the thin, second layer ranged from less than 1% for the compression wave speed to 20% for the layer thickness. As was the case for inversion of acoustic transfer functions, only the characteristic impedance was resolved in the half space where the estimation error was 1%.

When sensor burial depth errors were injected into the analysis, the inversion did not independently resolve density and compression wave speed. However, not only was the characteristic impedance resolved with good precision, but the thin elastic layer was detected and resolved where the error in the estimated thickness was 1%. This was the only case in which the ability to resolve the thin elastic layer was not lost with the injection of sensor burial depth errors.

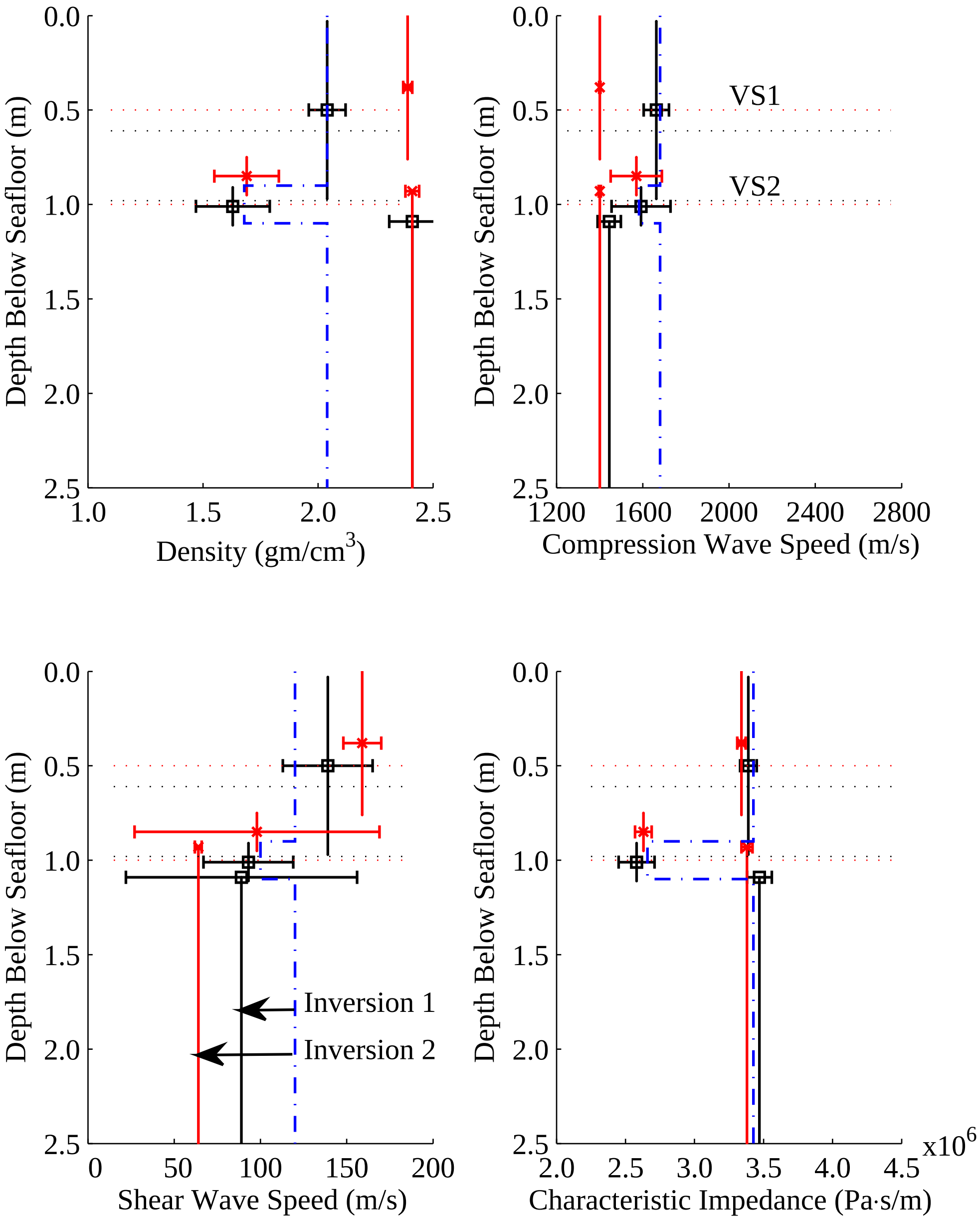

Figure 58. Inversion of synthetic specific acoustic impedance. Parameters of the simulated environment are indicated by the magenta dot-dash line. A thin, low impedance elastic layer was located at a nominal depth of one meter.

Table 10. Inversion of synthetic specific acoustic impedance. The synthetic data set was generated using buried sensor depths of 61 and 98 cm for VS1 and VS2, respectively. Estimate 1 addresses the case where the sensor depths were exactly known. Estimate 2 treats the case where the sensor depths were not exactly known. This inversion was run using buried sensor depths of 50 and 100 cm in the forward model.

Layer	**Parameter**	**Units**	**Value**	**Estimate 1**		**Estimate 2**	
				μ	σ	μ	σ
Water Column	Depth	m	16.7	16.6	0.5	16.6	0.2
	Sound Speed	m/s	1531	1531	19	1547	8
Sediment Layer One	Layer Thickness	cm	90	87	6	76	1
	Sediment Density	g/cm^3	2.04	2.04	0.08	2.39	0.02
	Compression Wave Speed	m/s	1680	1663	59	1401	3
	Shear Wave Speed	m/s	120	139	26	159	11
	Characteristic Impedance	MPa·s/m	3.43	3.39	0.06	3.34	0.03
Sediment Layer Two	Layer Thickness	cm	20	16	4	17	3
	Sediment Density	g/cm^3	1.68	1.63	0.16	1.69	0.14
	Compression Wave Speed	m/s	1583	1592	137	1570	119
	Shear Wave Speed	m/s	100	93	26	98	17
	Characteristic Impedance	MPa·s/m	2.66	2.58	0.13	2.63	0.06
Sediment Half Space	Sediment Density	g/cm^3	2.04	2.41	0.10	2.41	0.03
	Compression Wave Speed	m/s	1680	1445	54	1401	5
	Shear Wave Speed	m/s	120	89	67	64	2
	Characteristic Impedance	MPa·s/m	3.43	3.47	0.09	3.38	0.04

7.4 Inversion of SAX04 Field Data

Acoustic field data from the SAX04 experiment were inverted for the geoacoustic properties of the bottom. Two different experiment configurations were assumed. In the first (e.g., Inversion A), the buried sensor depths were taken to be 61 and 98 cm. A second inversion (e.g., Inversion B) was performed for which the buried sensors were assumed to have been at the intended depths of 50 and 100 cm.

Convergence behavior and objective function values for the inversions are provided as Fig. 59. Both inversions (e.g., A and B) produced similar convergence behavior, although inversion B ultimately converged on a solution set with slightly lower objective function values. Comparison of the objective function values obtained using real and synthetic (see Fig. 57) data reveals that the real data inversion did not achieve as low an objective function value as the synthetic case. As was discussed for the inversion of acoustic transfer functions, it was not unexpected that inversion of synthetic data would yield a better result as measured by the objective function values. Synthetic data inversions benefited from what in effect was perfect physics, an idealized environment and noise free data. It was unavoidable that results for inversion of real data would be impacted by the assumptions and approximations of the models used and the presence of noise in the data set.

Inversion results are summarized in Fig. 60 and Table 11. In both cases the environmental parameterization was simplified to a single layer approximately two meters thick overlying a sediment half space. Both inversions returned parameter estimates that were consistent with one another, despite the different sensor positions that were assumed by each. This tends to confirm results of the sensitivity study and synthetic data inversions where it was concluded that inversion of the specific acoustic impedance should be less affected by uncertainty in the buried

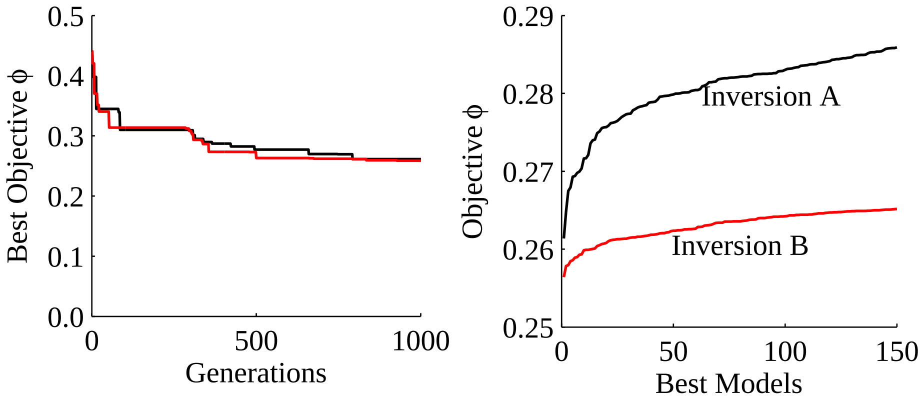

Figure 59. Convergence for inversion of SAX04 acoustic impedance. The left panel depicts the evolution of the best model realization over the course of the inversion. The right panel shows the objective function values for the best 150 model realizations. Inversion A assumed buried sensor depths of 61 and 98 cm below the seafloor. Inversion B assumed sensors were buried at intended depths of 50 and 100 cm below the seafloor.

sensor depths. In neither case were the estimates for density and compression wave speed reliable, as was also the case when inverting acoustic transfer functions. However, estimates of the characteristic impedance were consistent with expectations for this test site.

The shear wave speed estimate may not have been reliable because the layer to which this parameter was assigned contained both buried vector sensors. As discussed previously, the shear wave speed estimates were integrated into calculations of the velocity transfer functions for each of the buried vector sensors. The velocity transfer functions compensated for corruption in the vector field data that resulted from the frequency dependent sensor suspension response for the buried sensors. Therefore, unless the shear wave speed at both sensor depths were the same, the estimate is not necessarily valid physically.

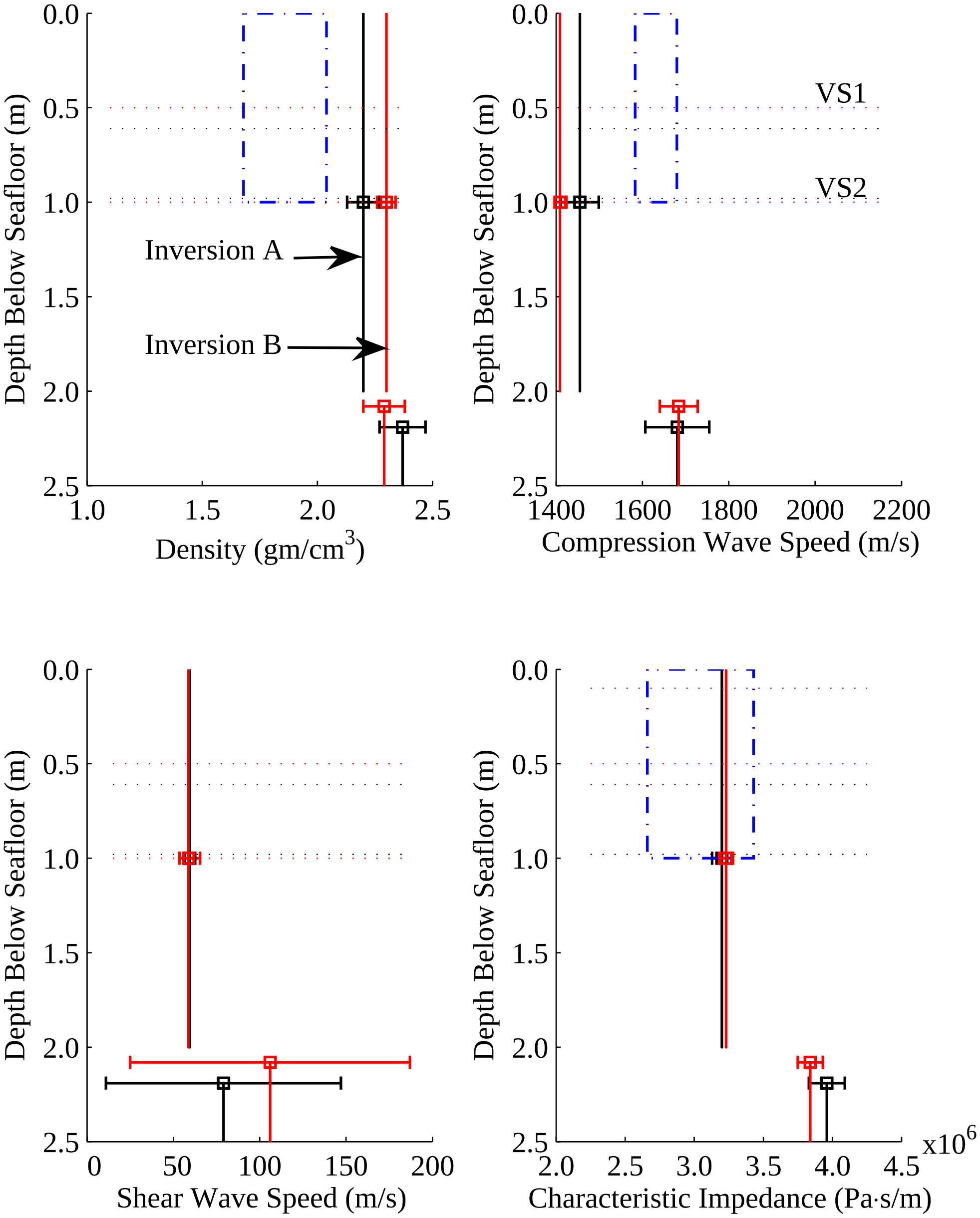

Figure 60. Inversion of SAX04 specific acoustic impedance. Inversion A assumed buried sensor depths of 61 and 98 cm. Inversion B assumed sensors were buried at the intended depths of 50 and 100 cm. Parameter bounds for density, compression wave speed and characteristic impedance shown as the blue dash-dot line were based on reports from the test site [1].

Table 11. Inversion of SAX04 specific acoustic impedance. Inversion A assumed buried sensor depths of 61 and 98 cm. Inversion B assumed sensors were buried at intended depths of 50 and 100 cm as intended.

Layer	**Parameter**	**Units**	**Inversion A**		**Inversion B**	
			μ	σ	μ	σ
Water Column	Depth	m	16.3	0.1	16.2	0.2
	Sound Speed	m/s	1530	21	1501	6
Sediment Layer One	Layer Thickness	cm	199	1	199	1
	Sediment Density	g/cm^3	2.20	0.07	2.30	0.04
	Compression Wave Speed	m/s	1455	44	1409	15
	Shear Wave Speed	m/s	59	6	59	3
	Characteristic Impedance	MPa·s/m	3.20	0.07	3.23	0.05
Sediment Half Space	Sediment Density	g/cm^3	2.41	0.10	2.29	0.09
	Compression Wave Speed	m/s	1681	54	1684	44
	Shear Wave Speed	m/s	89	67	106	81
	Characteristic Impedance	MPa·s/m	3.96	0.13	3.84	0.09

7.5 Discussion and Summary

A method for the inversion of acoustic scalar and vector field data was introduced in which the inversion operated on the derivative acoustic quantity of specific acoustic impedance. It was shown that the sensitivity of this method to uncertainties in the depths of the buried sensors was relatively less than that predicted for inversion of complex acoustic transfer functions discussed in the previous chapter.

A synthetic data set was generated to support both the sensitivity study and synthetic data inversions. The environmental parameterization used to generate the synthetic data was designed to emulate the conditions reported for this test site, including the thin elastic layer located at a nominal depth of one meter. Both the sensitivity study and inversion of the synthetic data suggested that the method would provide good performance, including greater tolerance of sensor burial depth errors relative to inversion of acoustic transfer functions.

Data collected during the SAX04 experiment was inverted for the depth dependent properties of the seafloor at the test site. The inversion was performed with two distinct parameterizations for the buried sensor depths. In the first inversion, the sensor depths were taken to be as estimated by a regularized inversion of acoustic data (e.g., 61 and 98 cm). In the second inversion, the sensor depths were taken to be as specified by the experiment plan (e.g. 50 and 100 cm). Results returned by both inversions were consistent in that each converged on a simplified environment characterized by a single sediment layer overlying a sediment half space. While neither inversion converged on plausible values for the density and compression wave speed for the surficial sediments, both converged on consistent, plausible values for the characteristic impedance of the sediment.

List of References

[1] J. C. Osler, D. M. F. Chapman, P. C. Hines, G. P. Dooley, and A. P. Lyons, "Measurement and modeling of seabed particle motion using buried vector sensors," *IEEE Journal of Oceanic Engineering*, vol. 35, no. 3, pp. 516–537, July 2010.

CHAPTER 8

Summary and Conclusions

8.1 Summary

The primary objective of this work was to test the postulate that the acoustic vector field contains information that could be used to improve estimates of the geoacoustic properties of the sea floor. This question was not addressed in the context of a traditional geoacoustic inverse problem where acoustic data are typically collected over paths lengths on the order of kilometers. Instead, data collected for this experiment sampled less than one wavelength of the seismo-acoustic field using sensors deployed in close proximity to the seafloor, on both sides of the interface. Thus, new inverse problem approaches were required to test the postulate that information in the acoustic vector field could measurably improve a given parameter estimate.

Inverse methods developed for this work operated on complex representations of the acoustic field. In the first instance, complex acoustic transfer functions between various pairs of acoustic vector sensors were inverted for the local geoacoustic properties. Inversion of acoustic transfer functions was selected to facilitate comparison of inversion results using only scalar field data, only vector field data and when both were included. An objective function was derived to guide a directed search for the set of parameter estimates that resulted in the lowest mismatch between the observed data and the prediction of a forward model, in this case a seismo-acoustic code based on wavenumber integration. An evolutionary algorithm was used to perform the directed search.

In the second instance, the complex specific acoustic impedance was inverted. Where the transfer functions were based on the ratio of like acoustic quantities observed at distinct locations, the specific acoustic impedance was based on the ratio of distinct quantities computed at a point. The performance of the impedance based inversions were compared to the inversion of combined scalar and vector transfer functions, there being no good analogue to impedance that does not include the vector field. Among the more favorable characteristics of the impedance based inversion was greater tolerance for uncertainties in the depths of the buried sensors, relative to inversion of acoustic transfer functions.

The central question addressed by this research was answered in the affirmative, albeit with a significant qualification. Data collected with the vector channels of a small number of acoustic vector sensors were used to improve estimates of the geoacoustic properties of the seafloor, most significantly the shear wave speed. However, information about the shear wave speed was shown to reside in the frequency dependent suspension responses of the buried sensors, not within the vector field itself. As shown by the sensitivity study, estimates of shear wave speed would not have been successful were the vector channel data not corrupted by the suspension response.

8.2 Conclusions

Particular questions posed at the beginning of this research sought to examine the utility of acoustic vector sensors for use in geoacoustic inversion experiments. In addition to addressing the central question of utility, these questions also sought to identify the limitations applicable to vector field inversion.

> *Did the vector acoustic field carry exploitable information about the environment that was not available in the scalar field?*

In the context of the SAX04 experiment, clear evidence for the presence of uniquely exploitable vector field information was not compelling. While there were certain improvements observed when vector field data was added to the inversion, it cannot be stated with great confidence that the improvements were due to the unique attributes of information carried by the vector field as opposed to improvement due simply to the availability of more information in a general sense. Specifically, it is not known whether equivalent performance gains could have been realized through the use of additional scalar field data, or if the gains were exclusive to information carried by the vector acoustic field. As a special case, scalar field sampling could be designed to yield estimates of the scalar field gradient, thus providing information equivalent to that provided by an inertial vector sensor through momentum considerations alone (Eq. 1). Given that the scalar and vector fields are coupled, questions of the relative merit of information provided by each are incomplete when separated from the context of the experiment.

> *Was information carried by the vector acoustic field useful only at the point of measurement, or was it also used to formulate parameter estimates at locations removed from the point of measurement?*

This research did not produce evidence that information carried by the vector field was qualitatively different from that in the scalar field. As a result, we might expect the estimates resulting from use of vector field data to have similar attributes to those gained with scalar field data. Taking the inversion of acoustic transfer functions as an example, parameters estimated based on observations at two distinct points represent the average properties over the path between those points. Among the parameters estimated by these inversion approaches was the layer thickness. The geophysical properties associated with each layer represent averages within the layer. This applies to estimates deriving their information from the acoustic vector field itself, exclusive of any information that may have been added by the suspension response of the buried sensors.

Interpretation of shear wave speed estimates demanded more care. In the inversions performed for this study, the shear wave speeds were point estimates local to each buried vector sensor. The best shear wave estimates resulting from this study were 35 m/s ($\sigma = 3$) and 69 m/s ($\sigma = 7$) at 50 cm and 100 cm depth, respectively. However, the shear wave speed estimate returned by the impedance based inversion was 59 m/s ($\sigma = 3$) for a layer that contained both of the buried vector sensors. This result does not necessarily represent the average shear wave speed for sediments located between the buried vector sensors in a physical sense. Instead, it represents the shear wave speed that best accounted for the data corruption due to the suspension responses of both sensors in a least squares sense.

> *Was the suspension response of an acoustic vector sensor used to improve geoacoustic parameter estimates? Did the improvement apply to only certain parameters and not others?*

Estimates for all geoacoustic parameters were improved by knowledge of the suspension response. In the case of shear wave speed estimates, it was the frequency dependent suspension response directly, that carried the relevant information. Estimation of all other parameters benefited by accounting for the transfer function between the acoustic vector field and vector data provided by the buried sensors. Systematic errors in the vector channel data were reduced by incorporation of the suspension dynamics in the inverse method.

Figure 61 presents an estimate for geoacoustic properties of the SAX04 test site that includes contributions from the inversion of both acoustic transfer functions and specific acoustic impedance. Only the characteristic impedance of the sediments is shown, neither inverse method having successfully resolved the density and compression wave speed independently. Also shown is the shear wave speed estimated at the depth of each buried sensor, and the objective function values for the best model realizations. Note that the depth dependent estimate for the characteristic impedance is consistent with the nominal value of 3.43x10^6 Pa·s/m and in the depth of the low impedance interface (< 1 m) reported by Osler [1].

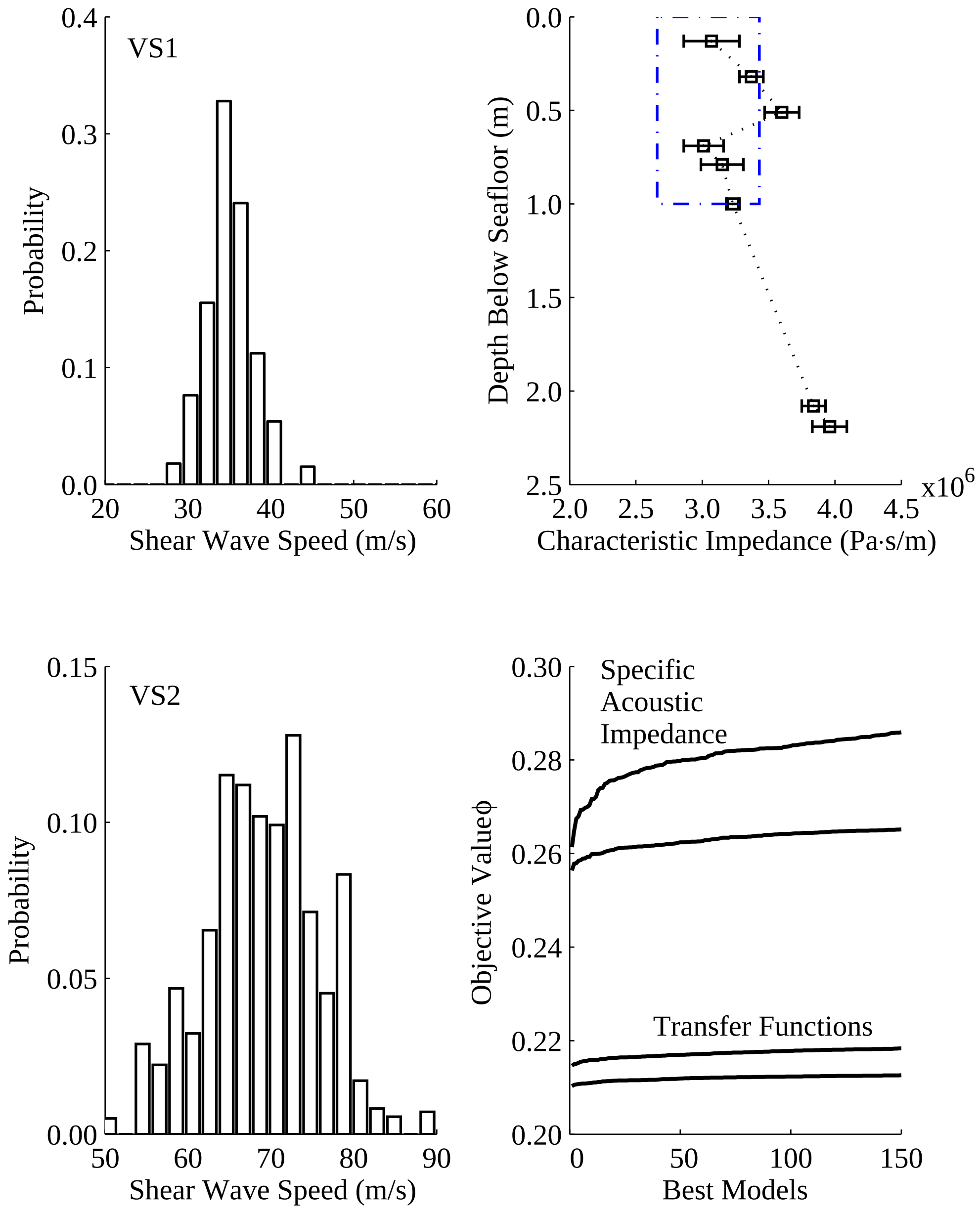

Figure 61. Summary results for inversion of SAX04 data

8.3 A Final Thought

Acoustic vector sensors have significant potential to advance the art of geoacoustic inversion. However, the complications introduced by the difficulty of making an accurate measurement of the seismo-acoustic vector field cannot be overstated. The tacit assumption often made by those newly acquainted with acoustic vector sensors is that data provided by the vector channels represent the vector field with adequate fidelity. The fact that real vector sensors invariably involve a mount, or other constraint on the motion of the sensor case, may be under appreciated. In the case of the inertial class of vector sensors used for this study, the result was the placement of a frequency dependent transfer function between the acoustic field variable and data representing that field variable. Analysis of the transfer function for probable values of sediment density and shear wave speed indicated the presence of a sensor suspension resonance within the analysis band. This frequency response function undoubtedly corrupted the vector channel data. However, the nature of that data corruption carried useful information about the environment in which the sensors were embedded, a truly fortuitous outcome.

List of References

[1] J. C. Osler, D. M. F. Chapman, P. C. Hines, G. P. Dooley, and A. P. Lyons, "Measurement and modeling of seabed particle motion using buried vector sensors," *IEEE Journal of Oceanic Engineering*, vol. 35, no. 3, pp. 516–537, July 2010.

BIBLIOGRAPHY

Bendat, J. S. and Piersol, A. G., *Random Data Analysis and Measurement Procedures*, 3rd ed. New York: John Wiley and Sons, 2000.

Boyles, C. A., *Acoustic Waveguides: Applications to Oceanic Science.* New York: John Wiley and Sons, 1984.

Briggs, K. B., Reed, A. H., Jackson, D. R., and Tang, D., "Fine-scale volume heterogeneity in a mixed sand/mud sediment off Fort Walton Beach, FL," *IEEE Journal of Oceanic Engineering*, vol. 35, no. 3, pp. 471–487, July 2010.

Buckingham, M. J., "Compressional and shear wave properties of marine sediments: Comparisons between theory and data," *Journal of the Acoustical Society of America*, vol. 117, no. 1, pp. 137–152, Jan. 2004.

Chapman, D. M. F., "What are we inverting for?" in *Inverse Problems in Underwater Acoustics*, Taroudakis, M. I. and Makrakis, G. N., Eds. New York, NY: Springer-Verlag, 2001.

Cray, B. A. and Nuttall, A. H., "Directivity factors for linear arrays of velocity sensors," *Journal of the Acoustical Society of America*, vol. 110, no. 1, pp. 324–331, July 2001.

Deng, K. K., "Underwater acoustic vector sensor using transverse-response free, shear mode, PMN-PT crystal," U.S. Patent 7 066 026, 2006.

DiNapoli, F. R. and Davenport, R. L., "Theoretical and numerical Green's function field solution in a plane multilayered medium," *Journal of the Acoustical Society of America*, vol. 67, no. 1, pp. 92–105, Jan. 1980.

Doyle, L. J. and Sparks, T. M., "Sediments of the Mississippi, Alabama, and Florida (MLFA) continental shelf," *Journal of Sedimentary Research*, vol. 50, no. 3, pp. 905–915, Sept. 1980.

Duval, C. Florida Division of Library and Information Services. "Storm surge during Hurricane Ivans's landfall: Fort Walton Beach, Florida." Aug. 2011. [Online]. Available: http://fpc.dos.state.fl.us/prints/pr75883.jpg

Evans, R. B., "A coupled mode solution for acoustic propagation in a waveguide with stepwise depth variations of a penetrable bottom," *Journal of the Acoustical Society of America*, vol. 74, no. 1, pp. 188–195, July 1983.

Fallat, M. R. and Dosso, S. E., "Geoacoustic inversion via local, global, and hybrid algorithms," *Journal of the Acoustical Society of America*, vol. 105, no. 6, pp. 3219–3230, June 1999.

Gerstoft, P., "Inversion of seismoacoustic data using genetic algorithms and *a posteriori* probability distributions," *Journal of the Acoustical Society of America*, vol. 95, no. 2, pp. 770–782, Feb. 1994.

Gerstoft, P. and Mecklenbräuker, C. F., "Ocean acoustic inversion with estimation of *a posteriori* probability distributions," *Journal of the Acoustical Society of America*, vol. 104, no. 2, pp. 808–819, Aug. 1998.

Guza, R. T. and O'Reilly, W., "Attenuation of ocean waves by ripples on the seafloor," Scripps Institution of Oceanography, La Jolla, CA, Tech. Rep., Mar. 2007.

Hamilton, E. L., "V_p / V_s and Poisson's ratios in marine sediments," *Journal of the Acoustical Society of America*, vol. 66, no. 4, pp. 1093–1101, Oct. 1979.

Han-Shu, P. and Feng-Hua, L., "Geoacoustic inversion based on a vector hydrophone array," *Chinese Physics Letters*, vol. 24, no. 7, pp. 1977–1980, July 2007.

Heard, G. J., Hannay, D., and Carr, S., "Genetic algorithm inversion of the 1997 geoacoustic inversion workshop test case data," *Journal of Computational Acoustics*, vol. 6, no. 1, pp. 61–71, Mar. 1998.

Hines, P. C., Osler, J. C., Scrutton, J. G. E., Chapman, D. M. F., and Lyons, A., "Using buried vector sensors to examine seabed layering in sandy sediment," *Journal of the Acoustical Society of America*, vol. 120, no. 5, p. 3181, Nov. 2006.

Hines, P. C., Osler, J. C., Scrutton, J. G. E., and Halloran, L. J. S., "Time-of-flight measurements of acoustic wave speed in sandy sediment at 0.6–20 kHz," *IEEE Journal of Oceanic Engineering*, vol. 35, no. 3, pp. 502–515, July 2010.

Jensen, F. B., Kuperman, W. A., Porter, M. B., and Schmidt, H., *Computational Ocean Acoustics*, ser. Modern Acoustics and Signal Processing. New York: Springer-Verlag, 1993.

Jeyakumar, G. and Velayuthan, C. S., "A comparative performance analysis of differential evolution and dynamic differential evolution variants," in *World Congress on Nature and Biologically Inspired Computing*, 2008, pp. 463–468.

Jeyakumar, G. and Velayuthan, C. S., "An empirical comparison of differential evolution variants on different classes of unconstrainted global optimization problems," in *World Congress on Nature and Biologically Inspired Computing*, 2009, pp. 866–871.

Kester, W., *ADC Input Noise: The Good, The Bad, and The Ugly. Is No Noise Good Noise?*, Analog Devices, Norwood, MA, 2006.

Koch, R. A., “Proof of principle for inversion of vector sensor array data,” *Journal of the Acoustical Society of America*, vol. 128, no. 2, pp. 590–599, Aug. 2010.

Kolsky, H., *Stress Waves in Solids.* New York: Dover Publications, 1963.

McConnell, J. A., “Analysis of a compliantly suspended acoustic velocity sensor,” *Journal of the Acoustical Society of America*, vol. 113, no. 3, pp. 1395–1405, Mar. 2003.

Mecklenbräuker, C. F. and Gerstoft, P., “Objective functions for ocean acoustic inversion derived by likelihood methods,” *Journal of Computational Acoustics*, vol. 8, no. 2, pp. 259–270, June 2000.

Menke, W., *Geophysical Data Analysis: Discrete Inverse Theory*, ser. International Geophysics Series, Dmowska, R. and Holton, J. R., Eds. San Diego: Academic Press, 1989, vol. 45.

Mezura-Montes, E., Velázquez-Reyes, J., and Coello, C. A., “A comparative study of differential evolution variants for global optimization,” in *Proceedings of the 8th Annual Conference of Genetic and Evolutionary Computation*, 2006, pp. 485–492.

National Geophysical Data Center. “A global self-consistent, hierarchical, high-resolution shoreline database.” Feb. 2010. [Online]. Available: http://www.ngdc.noaa.gov/mgg/shorelines/gshhs.html

Nehorai, A. and Paldi, E., “Acoustic vector-sensor array processing,” *IEEE Transactions on Signal Processing*, vol. 42, no. 9, pp. 2481–2491, Sept. 1994.

Oestreicher, H. L., “Field and impedance of an oscillating sphere in a viscoelastic medium with an application to biophysics,” *Journal of the Acoustical Society of America*, vol. 23, no. 6, pp. 707–714, Nov. 1951.

Osler, J. C., “Cruise report SAX04,” Nov. 2004, unpublished.

Osler, J. C. and Chapman, D. M. F., “Quantifying the interaction of an ocean bottom seisometer with the seabed,” *Journal of the Geophysical Research*, vol. 103, no. B5, pp. 9879–9894, May 1998.

Osler, J. C., Chapman, D. M. F., Hines, P. C., Dooley, G. P., and Lyons, A. P., “Measurement and modeling of seabed particle motion using buried vector sensors,” *IEEE Journal of Oceanic Engineering*, vol. 35, no. 3, pp. 516–537, July 2010.

Pekeris, C. L., “Theory of propagation of explosive sound in shallow water,” in *Memiors*, vol. 27. Geological Society of America, 1948.

Potty, G. R. and Miller, J. H., “Nonlinear optimization techniques for geoacoustic tomography,” in *Inverse Problems in Underwater Acoustics*, Taroudakis, M. I. and Makrakis, G. N., Eds. New York, NY: Springer-Verlag, 2001.

Potty, G. R., Miller, J. H., Dahl, P. H., and Lazauski, C. J., “Geoacoustic inversion results from the ASIAEX East China Sea experiment,” *IEEE Journal of Oceanic Engineeering*, vol. 29, no. 4, pp. 1000–1010, Jan. 2005.

Potty, G. R., Miller, J. H., Lynch, J. F., and Smith, K. B., “Tomographic inversion for sediment parameters in shallow water,” *Journal of the Acoustical Society of America*, vol. 108, no. 3, pp. 973–986, Sept. 2000.

Price, K. V., , Storn, R. M., and Lampinen, J. A., *Differential Evolution A Practical Approach to Global Optimization*, ser. Natural Computing Series. Heidelberg Germany: Springer-Verlag, 2005.

Richardson, M. D., Briggs, K. B., Bibee, L. D., Jumars, P. A., Sawyer, W. B., Albert, D. B., Bennett, R. H., Berger, T. K., Buckingham, M. J., Chotiros, N. P., Dahl, P. H., Dewett, N. T., Pleischer, P., Flood, R., Greenlaw, C. F., Holliday, D. V., Hulbert, M. H., Hutnak, M. P., Jackson, P. D., Jaffee, J. S., Johnson, H. P., Lavoie, D. L., Lyons, A. P., Martens, C. S., McGehee, D. E., Moore, K. D., Orsi, T. H., Piper, J. N., Ray, R. I., Reed, A. H., Self, R. F. L., Schmidt, J. L., Schock, S. G., Simonet, F., Stoll, R. D., Tang, D., Thistle, D. E., Thoros, E. I., Walter, D. J., and Wheatcroft, R. A., “Overview of SAX99: Environmental considerations,” *IEEE Journal of Oceanic Engineering*, vol. 26, no. 1, pp. 26–53, Jan. 2001.

Santos, P., Rodriguez, O., Felisberto, P., and Jesus, S., “Geoacoustic matched-field inversion using a vertical vector sensor array,” in *Proceedings of the Third International Conference and Exhibition on Underwater Acoustic Measurements: Technologies & Results*, June 2009.

Schmidt, H., *SAFARI Seismo-Acoustic Fast Field Algorithm for Range Independent Environments*, Supreme Allied Command Anti-Submarine Warfare Research Center, La Spezia, Italy, Sept. 1988.

Schmidt, H., *OASES Version 3.1 User Guide and Reference Manual*, Massachuesetts Institute of Technology, July 2006. [Online]. Available: http://acoustics.mit.edu/faculty/henrik/oases.html

Schmidt, H. and Jensen, F. B., “A full wave solution for propagation in multilayered viscoelastic media with application to Gaussian beam reflection at fluid-solid interfaces,” *Journal of the Acoustical Society of America*, vol. 77, no. 3, pp. 813–825, Mar. 1985.

Sherman, C. H. and Bulter, J. L., *Transducers and Arrays for Underwater Sound.* New York: Springer, 2007.

Shipps, J. C. and Deng, K., “A minature vector sensor for line array applications,” in *Proceedings OCEANS 2003*, 2003, pp. 2367–2370.

Simons, D. G., Moll, C. V., and Harrison, C. H., “Inversion of shallow water ambient noise data by means of differential evolution as a global search method,” in *Acoustic Sensing Techniques for the Shallow Water Environment*, Caiti, A., Chapman, N. R., Hermand, J.-P., and Jesus, S. M., Eds. Dordrecht, The Netherlands: Springer-Verlag, 2006.

Skudrzyk, E., *The Foundations of Acoustics.* New York: Springer-Verlag, 1971.

Smith, K. B. and van Leijen, A. V., “Steering vector sensor array elements with linear cardiods and nonlinear hippioids,” *Journal of the Acoustical Society of America*, vol. 122, no. 1, pp. 370–377, July 2007.

Stephen, R. A., “A review of finite difference methods for seismo-acoustics problems at the seafloor,” *Reviews of Geophysics*, vol. 26, no. 3, pp. 445–458, 1988.

Stewart, S. R. National Hurricane Center. “Tropical cyclone report, Hurricane Ivan, 2–24 September 2004.” May 2005. [Online]. Available: http://www.nhc.noaa.gov/2004ivan.shtml

Storn, R. M. and Price, K. V., “Differential evolution – a simple and efficient heuristic for global optimization over continuous spaces,” *Journal of Global Optimization*, vol. 11, no. 4, pp. 341–359, Dec. 1997.

Tappert, F. D., *The Parabolic Approximation Method*, ser. Lecture Notes in Physics. New York: Springer-Verlag, 1977, vol. 70.

Temkin, S., *Elements of Acoustics.* New York: John Wiley and Sons, 1981.

Thoros, E. I., Richardson, M. D., and Lynch, J. F., “Guest editorial special issue on sediment acoustic processes,” *IEEE Journal of Oceanic Engineering*, vol. 33, no. 4, pp. 357–358, Oct. 2008.

Thoros, E. I., Williams, K. L., Chotiors, N. P., Christoff, J. T., Commander, K. W., Greenlaw, C. F., Holliday, D. V., Jackson, D. R., Lopes, J. L., McGehee, D. E., Piper, J. E., Richardson, M. D., and Tang, D., “An overview of SAX99: Acoustic measurements,” *IEEE Journal of Oceanic Engineering*, vol. 26, no. 1, pp. 4–25, Jan. 2001.

University of Washington, Applied Physics Laboratory. “SAX04 deployment plan revision 1.2.” Feb. 2007. [Online]. Available: http://www.apl.washington.edu/projects/SAX04/sax04_layout.pdf

Vaughan, W. C., Briggs, K. B., Kim, J.-W., Bianchi, T. S., and Smith, R. W., “Storm-generated sediment distribution along the northwest Florida inner continental shelf,” *IEEE Journal of Oceanic Engineering*, vol. 34, no. 4, pp. 495–515, Oct. 2009.

Vendhan, C. P., Diwan, G. C., and Bhattacharyya, S. K., "Finite-element modeling of depth and range dependent acoustic propagation in oceanic waveguides," *Journal of the Acoustical Society of America*, vol. 127, no. 6, pp. 3319–3326, June 2010.

The TV-001 Miniature Vector Sensor, Wilcoxon Research, Inc., Gaithersburg, MD, 2003.

Zaharie, D., "A comparative analysis of crossover variants in differential evolution," in *Proceedings of the International Multiconference on Computer Science and Information Technology*, 2007, pp. 171–181.

Zaharie, D., "Adaptive differential evolution and exponential crossover," in *Proceedings of the International Multiconference on Computer Science and Information Technology*, 2008, pp. 927–931.

Zielinski, K., Wang, X., and Laur, R., "Comparison of adaptive approaches for differential evolution," in *Parallel Problem Solving from Nature*, ser. Lecture Notes in Computer Science, Rudolph, G., Jansen, T., Lucas, S., Poloni, C., and Beume, N., Eds., vol. 5199. Heidelberg Germany: Springer-Verlag, 2008, pp. 641–650.